

Abstract

Quantum adiabatic computing is a promising framework for tackling combinatorial optimization problems by exploiting quantum mechanical principles such as superposition and the adiabatic theorem. In this context, [1] proposed a method of quantum computation based on bifurcations in quantum non linear oscillators, enabling the generation of cat states. This approach demonstrated that can be used to solve combinatorial problems such as the Ising model.

This master's thesis provides a concise review of the bifurcation-based quantum computation proposed in [1] and, as one of the thesis' objectives, extends this approach by implementing the method in a novel model of quantum oscillators defined within a dissipative environment [2]. The mean-field equations of these dissipative oscillators are analysed for both single and coupled cases, to study the dynamic of the system and how it changes with the couplings. Moreover, numerical simulations are conducted to examine the Ising model with random couplings and the Hopfield network, with emphasis on memory storage and the resulting ground-state degeneracy. Finally, the method, using both types of oscillators, is applied to the determination of eigenvectors of a matrix \mathbf{M} .

Contents

Abstract	i
1 Introduction	2
1.1 Theoretical Context	2
1.2 Objectives	2
2 Theoretical Framework	4
2.1 Quantum mechanics	4
2.1.1 Density matrix	4
2.1.2 Liouville space	4
2.1.3 Wigner function	5
2.1.4 Master equation	5
2.1.5 Symmetries and conserved quantities	7
2.1.5.1 Conserved quantities	8
2.1.5.2 Symmetries	8
2.1.5.3 \mathbb{Z}_p symmetry	8
2.1.6 Adiabatic theorem of quantum mechanics	9
2.1.7 Quantum Optics	10
2.1.7.1 Coherent states and displacement operator	10
2.1.7.2 Squeezed states and squeezing operator	11
2.2 Kerr Parametric Oscillators	13
2.2.1 KPO model	13
2.2.2 Quantum computation with a KPO network	14
2.2.3 Ising model with an external field	15
2.3 Dissipative oscillator	16
2.3.1 Generation of the cat states	17
3 Methodology	21
3.1 Success probability of a configuration \vec{S}	21
3.2 Simulations	22
3.2.1 KPO	22
3.2.2 Dissipative oscillators	22
4 Results and discussion	23
4.1 Result with the KPO oscillators	23
4.1.1 Overlap with the theoretical result	23
4.1.2 Success probability of the Ising model with and without an external field	24
4.2 Dissipative oscillators	26
4.2.1 Validity of the mean field approximation of the dissipative oscillators	26
4.2.2 Coupled dissipative oscillators	28
4.2.3 Results of the Ising model	31
4.3 Applications	33
4.3.1 Hopfield model	33
4.3.2 Eigenvector problem	35
5 Conclusions	43
6 Future work	44
A Hopfield model	45
B Limit of the amplification of the non-lineal Hamiltonian for the KPO	45
C Energy of the ground state of the H_{NL}	47
D Mean-field approximation for one oscillator	51
E Mean-field approximation of the Ising model for two oscillators with $\vec{h} = 0$	56
F Parity symmetry for coupled dissipative oscillators	62

G QUBO	63
H Quantum annealing	64
I Eigenvector determination	65
J Computational resources	71
K Wigner Picture	73
K.1 Weyl transform	73
L Rotation Frame	74
References	75

1 Introduction

1.1 Theoretical Context

Combinatorial optimization is a subfield of mathematical optimization concerned with finding configurations that minimize a given objective function [3, 4]. These problems involve discrete decision variables and finite search spaces, which are typically too large for exhaustive search methods [4, 5]. Many of these problems belong to the class of NP-hard optimization problems, meaning that they cannot be solved efficiently [5, 6].

The NP-hard class of problems is highly important, since real-world problems belong to this family. Some examples include the Multiprocessor Scheduling in computer science [7], the Travelling Salesman Problem in logistic [8], the Protein Folding in biology [9], the Airline Scheduling problem in aviation [10], Genotype Imputation in genetics [11] and other formulations such as Quadratic Unconstrained Binary Optimization (QUBO) [12, 13] and G. Furthermore, NP-hard problems also arise in machine learning and deep learning too, for example in K-Means Clustering [14] and Support Vector Machines [15]. Solving them accurately and efficiently can have a significant impact on industry, improving logistic, advancing the understanding of crucial biochemical processes, enabling rapid training of deep neural networks [6]... Developing effective methods to address NP-hard problems is essential for scientific and technological progress.

The main challenge with NP-hard problems is that there is no efficient method to solve them. Conventional techniques tend to rely on heuristic algorithms that provide approximate solutions like [8, 16]. However, such methods do not guarantee exact solutions, and no efficient algorithm has yet been discovered that can solve the NP-hard problems exactly. If such algorithm were found, the field of mathematical optimization would be revolutionized, since NP-hard problems do possess a key feature: any NP-hard problem can be reduced efficiently to another NP-hard problem [6, 17, 18]. Thus, an efficient algorithm for one NP-hard problem would provide efficient solutions for all problems of this class. For instance, an efficient algorithm for Travelling Salesman Problem also enable efficient solutions to the Protein Folding problem.

In this context, quantum computers have attracted significant attention in recent years. They provide new computational paradigms that may address NP-hard problems more efficiently, particularly through quantum annealing [19, 20, 21, 22], which promises to outperform classical approaches. Quantum computers have been particularly specialised in the class of Quadratic Unconstrained Binary Optimization (QUBO) problems, where decision variables take binary values $\{0, 1\}$. As is discussed in [12], any QUBO instance can be transformed into an Ising formulation, where decision variables are $\{-1, 1\}$. Consequently, a quantum algorithm capable of solving the Ising model can, in principle, solve any QUBO instance and thus, any NP-hard problem.

In this context, [1] proposed the use of a Kerr parametric oscillator [23] to perform quantum adiabatic computation. Their model relies on amplifying the non linear component of the Hamiltonian to deterministically generate odd or even cat states by crossing a bifurcation. Using this approach, they demonstrated that, using appropriate coupling between the oscillators, the model can solve the Ising problem both with and without external field [24]. Their work introduce the novel concept of exploiting bifurcations for quantum adiabatic computing. Although no physical implementation has yet been realized, potential platforms have been suggested in [1], which include Josephson Junctions [25, 26, 27, 28, 29, 30], nanoelectromechanical systems [31, 32] and carbon nanotubes [33]. However, the physical implementation of these methods lies beyond the scope of the present study.

Additionally, [34] introduced an oscillator defined in a dissipative environment in the context of associative memory, exploiting its metastability to retrieve stored states. Subsequently, [2] demonstrated that, under appropriate parameters, this system supports cat states as steady states, enabling its use in bifurcation-based quantum computing as is proposed in [1]. Unlike the model in [1], which deteriorates under dissipation [24], this mechanism intrinsically relies on dissipation, suggesting enhanced robustness in open-system settings and motivating further study of coupled dissipative oscillators, for which the effect of interaction terms has not yet been studied.

1.2 Objectives

There are three main objectives in this study. First, it provides a critical review of the bifurcation-based quantum computer model proposed in [1, 24], focusing on its application to the Ising model with and without an external field, and assesses the validity of the assumptions made to derive their results. Second, subsequent to this analysis,

the study seeks to extend the approach by applying the same quantum computation methodology to the oscillator examined in [2, 34], which is defined within a dissipative environment. Finally, both oscillators will be employed to solve the Hopfield network and to compute the eigenvectors associated with a given eigenvalue.

2 Theoretical Framework

2.1 Quantum mechanics

Throughout this work, all parameters are expressed in units of \hbar , and therefore we set $\hbar = 1$.

2.1.1 Density matrix

In a quantum system, we may have an ensemble of quantum states $\{|\psi_i\rangle\} \in \mathcal{H}$, where each state is given with probability $p_i \geq 0$. Therefore, the concept of matrix density is introduced to characterize the ensemble:

$$\rho = \sum_i p_i |\psi_i\rangle \langle \psi_i| \quad (1)$$

$$\langle A \rangle = \text{Tr}(A\rho) = \sum_i p_i \langle \psi_i | A | \psi_i \rangle$$

Any quantum state that can be written as in equation 1 is a density matrix. This kind of matrix spans a convex set; thus, any linear combination of density matrices is also a density matrix:

$$\rho = p\rho_A + (1-p)\rho_B \quad p \in [0, 1] \quad \rho, \rho_A, \rho_B \in \mathcal{B}(\mathcal{H}) \quad (2)$$

The properties that characterize this operator are [35]:

- Unit trace:

$$\text{Tr}(\rho) = 1 \quad (3)$$

Since the eigenvalues of ρ are interpreted as probabilities, their sum must be normalized to one.

- Self-adjoint: $\rho^\dagger = \rho$
- Semi-definite positive: $\rho \geq 0 \rightarrow \langle \psi | A | \psi \rangle \geq 0, \forall |\psi\rangle \in \mathcal{H}$ This means that ρ does not have any negative eigenvalue.

Finally, the time evolution of a density matrix in a close quantum system is given by the Von Neumann or Liouville—Von Neumann equation [35]:

$$\dot{\rho}(t) = -i[H, \rho(t)] \quad (4)$$

2.1.2 Liouville space

Since the set of density matrices is convex, it can be defined a Hilbert space whose elements corresponds with these operators treated as vectors. This space is known as Liouville space, L . It can be understood as the resulting Hilbert space obtained from the tensor product between the original space and its dual [36, 37]. Therefore, each density matrix in $\mathcal{B}(\mathcal{H})$ is mapped to a vector in L :

$$\begin{pmatrix} \rho_{11} & & & \rho_{1n} \\ \cdot & \cdot & \cdot & \cdot \\ \rho_{n1} & \cdot & \cdot & \rho_{nn} \end{pmatrix} \longrightarrow \begin{pmatrix} \rho_{11} \\ \cdot \\ \cdot \\ \rho_{1n} \\ \cdot \\ \cdot \\ \rho_{nn} \end{pmatrix} = |\rho\rangle \in L \quad (5)$$

And the inner product in this space:

$$\langle \langle \rho | \sigma \rangle \rangle = \text{Tr}(\rho^\dagger \sigma) \quad (6)$$

The action of operators on the density matrix can also be expressed in L using the Kronecker product [36]:

$$A \otimes B = \begin{pmatrix} A_{11}B & \cdot & \cdot & A_{1N}B \\ \cdot & \cdot & \cdot & \cdot \\ \cdot & \cdot & \cdot & \cdot \\ A_{N1}B & \cdot & \cdot & A_{NN}B \end{pmatrix} \quad (7)$$

The action of the operators in Liouville space can be expressed as:

Original space	\mathcal{H}_F
$A\rho$	$A^\dagger \otimes I \rho\rangle\rangle$
ρB	$I \otimes B^\dagger \rho\rangle\rangle$
$A\rho B$	$A \otimes B^\dagger \rho\rangle\rangle$

Table 1: Rules for rewriting operators in L

2.1.3 Wigner function

The Wigner function is the quantum generalization of the classical probability distribution and serve as the phase space counterpart of the density matrix. Its definition is straightforward using the Weyl transform \mathbf{K} , given the density operator ρ :

$$W(x, p) = \frac{1}{2\pi} \int dy e^{-ipy} \langle x + y/2 | \rho | x - y/2 \rangle = \mathcal{W}\left[\frac{1}{2\pi}\rho\right] \quad (8)$$

The Wigner function is a real-valued function and is considered a quasi-probability distribution rather than a true joint probability density. As a result, there can be regions of the phase space where its value is negative (this is a consequence of the quantum correlations). Furthermore, it may take non-zero values in regions where the standard probability distribution $|\psi(x)|^2 = 0$. The physical interpretation of the Wigner function becomes meaningful after integration. Moreover, the Wigner function can be directly connected to the wave function description:

$$|\psi(x)|^2 = \rho(x) = \int dp W(x, p) \quad |\psi(p)|^2 = \int dx W(x, p) \quad (9)$$

Since it is a quasi-probability distribution, the Wigner function is normalized over the position-momentum phase space:

$$1 = \int dx dp W(x, p) \quad (10)$$

This description also enables the computation of the expected values of operators A :

$$\langle A \rangle = \int dx \int dp W(x, p) A(x, p) \quad (11)$$

Finally, Wigner function has an upper bound $|W(x, p)| \leq 4\pi$.

2.1.4 Master equation

If a closed system is considered, its full evolution is determined by the Von Neumann equation 4 for the density matrix. The solutions to this equation do not converge to a stationary state for long times, unless the initial state was a pure state corresponding to an eigenstate of the Hamiltonian.

However, if a dissipative term is added, the system will converge to a steady state at long times. This occurs for systems being in contact with an external environment (\mathcal{H}_E):

$$\mathcal{H} = \mathcal{H}_A \otimes \mathcal{H}_E \quad (12)$$

The system of interest is \mathcal{H}_A , which interacts with a thermal bath \mathcal{H}_E . This setup is known as open quantum system. For Markovian processes in \mathcal{H}_A , the evolution of the density matrix is determined by the Lindblad master equation [35]:

$$\dot{\rho}(t) = -i[H(t), \rho(t)] + \sum_i L_i \rho(t) L_i^\dagger - \frac{1}{2} \left\{ L_i^\dagger L_i, \rho(t) \right\} = \mathcal{L}\rho(t) \quad (13)$$

This master equation describes the non-unitary evolution of an open quantum system in contact with a thermal bath. This evolution allows the system to thermalize and reach an steady state. Furthermore, the jump operators L_i are defined such that their action on the quantum state represent spontaneous jumps between quantum states.

Moreover, the Lindblad (or Lindbladian) superoperator can be defined as follows:

$$\mathcal{L}(\cdot) = -i[H(t), (\cdot)] + \sum_i L_i(\cdot) L_i^\dagger - \frac{1}{2} \left\{ L_i^\dagger L_i, (\cdot) \right\} \quad (14)$$

A superoperator is defined as an operator that acts on the space $\mathcal{B}(\mathcal{H}_A)$, which consists of all linear operators on the Hilbert space \mathcal{H}_A .

The Lindblad equation satisfies the following properties:

- Trace preservation: $\text{Tr}(\dot{\rho}(t)) = 0$. This ensure that the total probability remains normalized over time.
- Positivity preservation: $\rho(t) \geq 0$. Since \mathcal{L} is a CPTP map, the positivity of the density matrix $\rho(t)$ is guaranteed for $t > 0$.
- Hermiticity preservation: $\rho(t) = \rho^\dagger(t)$.

The solution to the equation:

$$\dot{\rho}(t) = \mathcal{L}\rho(t) \longrightarrow \rho(t) = T \left[e^{\int_{t_0}^t ds \mathcal{L}(s)} \right] \rho(0) \quad (15)$$

Here, $T[\cdot]$ denotes the time ordered operator. Since the system must converge to a steady state at long times, the spectrum of the superoperator must lie in the complex plane with $\Re[\lambda] \leq 0$. Otherwise, the solution will diverge, and ρ would no longer represent a valid density matrix.

The Lindbladian can be expressed in its eigenbasis as follows:

$$|\rho(t)\rangle\rangle = T \left[e^{\int_{t_0}^t ds \mathcal{L}(s)} \right] |\rho(0)\rangle\rangle = \sum_i e^{\lambda_i(t)} \langle\langle \Lambda_i^L(t) | \rho(0) \rangle\rangle |\Lambda_i^R(t)\rangle\rangle \quad (16)$$

The Lindbladian \mathcal{L} is decomposed in terms of its left eigenvectors ($\langle\langle \Lambda_i^L |$) and right eigenvectors ($|\Lambda_i^R \rangle\rangle$), since \mathcal{L} is generally non-hermitian:

$$\begin{aligned}
 \mathcal{L}(t) &= \sum_i \lambda_i(t) |\Lambda_i^R(t)\rangle\langle\Lambda_i^R(t)| \\
 \mathcal{L}(t) |\Lambda_i^R(t)\rangle\langle\Lambda_i^R(t)| &= \lambda_i(t) |\Lambda_i^R(t)\rangle\langle\Lambda_i^R(t)| \\
 \langle\langle\Lambda_i^L(t)|\mathcal{L}(t) &= \lambda_i(t) \langle\langle\Lambda_i^L(t)| \\
 \langle\langle\Lambda_i^L(t)|\Lambda_j^R(t)\rangle\langle\Lambda_j^R(t)| &= \delta_{ij}
 \end{aligned} \tag{17}$$

Thanks to the Evan's theorem [38], we know that in finite-dimensional spaces, there is always at least one eigenvalue $\lambda_i = 0$, which corresponds to the steady state of the system:

$$\rho_{ss} = \lim_{t \rightarrow \infty} T \left[e^{\int_{t_0}^t ds \mathcal{L}(s)} \right] \rho(0) \tag{18}$$

2.1.5 Symmetries and conserved quantities

As discussed in [39, 40], there are several differences between unitary and dissipative system, when dealing with symmetries and conserved quantities. To introduce the behaviour of each system under symmetries, the states will be represented by density matrices, which belongs to the Liouville space L of dimension N^2 , being N the dimension of the Hilbert space of the system \mathcal{H} . Although the states are matrices, they will be treated as a vectors in L , $|\rho\rangle \in L$. Furthermore, the steady state of the system will correspond with the eigenstates of the subspace $L_{ss} \subset L$.

In unitary systems, there are at least N steady states; conversely, in dissipative system, there can be fewer than N steady states. Furthermore, the dimension of the steady states subspace L_{ss} is not determined solely by the Hamiltonian structure, but is also influenced by the jumps operators of the system. The subspace L_{ss} corresponds to the subspace generated by the right eigenoperators $\{|\Lambda_i^R\rangle\}_{i=1}^d$ of \mathcal{L} with zero eigenvalue. In these systems, states can also exhibit steady-states coherences and oscillating coherences. However, the appearance of the latter coherences depends exclusively on the unitary part of \mathcal{L} .

Systems undergoing unitary evolution exhibits a direct relationship between conserved quantities J and continuous symmetries $U = e^{i\phi J}$, as stated in the Noether's theorem:

$$[H, J] = 0 \iff J = 0 \iff U^\dagger H U = H \tag{19}$$

In contrast, for dissipative systems, the adjoint of a superoperator $\mathcal{U} = U(\cdot) U^\dagger$ ($U = e^{i\phi J}$) is defined as:

$$\mathcal{U} = e^{i\phi \mathcal{J}} \quad \mathcal{U}^\dagger = U^\dagger(\cdot) U \tag{20}$$

A conserved quantity J in a dissipative system can then be defined by $\mathcal{L}^\dagger J = 0$. Therefore, the following statements regarding symmetries and conserved quantities can be established:

- I. $[J, H] = [J, L_k] = 0$
- II. $\dot{J} = 0$
- III. $\mathcal{U}^\dagger \mathcal{L} \mathcal{U} = \mathcal{L}$

The peculiarity with respect the unitary evolution is that I \implies II, I \implies III but II $\not\implies$ I, III $\not\implies$ I, and III $\not\iff$ II. This allows the following situations:

- There can be conserved quantities that do not commutes with all of \mathcal{L} but are still conserved as a whole.
- The symmetry U generated by such a quantity does not have to be a symmetry of the system.
- The symmetry generator does not have to commute with every element of \mathcal{L} .

- A symmetry generator does not correspond to a conserved quantity.

Thus, in dissipative systems, symmetries and conserved quantities need not be directly related. This arise because a symmetry at the superoperator level does not always imply a symmetry at the operator level [39]. Nevertheless, they provide important information about the steady states and the block diagonalization of \mathcal{L} . Finally, when condition I is satisfied, the symmetry is called a strong symmetry, as it is associated with a conserved quantity; otherwise, it is referred to as a weak symmetry [41].

2.1.5.1 Conserved quantities

A conserved quantity in a dissipative system can be defined as a left eigenoperator J that belong to the zero-eigenvalue subspace of \mathcal{L}^\dagger . Therefore, the operator J satisfies the eigenvalue equation $\mathcal{L}^\dagger J = \dot{J} = 0$, and the number of conserved quantities is given by $\dim(L_{ss}) = D$ [42]. Since the conserved quantities corresponds with left eigenoperators of \mathcal{L} , there exists a direct relationship between the basis elements of L and conserved quantities.

If \mathcal{L} has no purely imaginary eigenvalues and $\{M_\mu\}_{\mu=0}^D$ be an orthonormal basis for the D -dimensional space L_{ss} , the steady state of the system can be expanded in this basis:

$$\rho_{ss} = \lim_{t \rightarrow \infty} T \left[e^{\int_{t_0}^t \mathcal{L}(s)} \right] \rho(0) = \sum_{\mu=0}^D \rho_\mu M_\mu \quad (21)$$

It is important to note that M_μ does not need to satisfy any of the conditions of a density matrix; they simply form a basis of L_{ss} . This expansion shows that the expectation value of a conserved quantity J_μ correspond to the contribution of M_μ to the steady state:

$$\langle\langle J_\mu | \rho(0) \rangle\rangle = \langle\langle J_\mu | \rho_{ss} \rangle\rangle = \rho_\mu \quad (22)$$

2.1.5.2 Symmetries

In a unitary system, an operator $U = e^{i\phi J}$ can be considered a symmetry, if it commutes with the Hamiltonian of the system $[H, U]$. In a dissipative system, the operator U will constitute a continuous symmetry if the superoperator $\mathcal{U} = e^{i\phi \mathcal{J}}$ commutes with the Lindbladian $[\mathcal{L}, \mathcal{U}] = [\mathcal{L}, \mathcal{J}] = 0$. Therefore, since U is a symmetry:

$$T \left[e^{\int_{t_0}^t \mathcal{L}(s)} \right] (U^\dagger \rho(0) U) = U^\dagger T \left[e^{\int_{t_0}^t \mathcal{L}(s)} \right] (\rho(0)) U \quad (23)$$

In particular, any symmetry that commutes with the Hamiltonian, $U^\dagger H U = H$, and with the jump operators $U L_k U^\dagger = L_k e^{i\phi}$ [43], or any permutation among the jump operators, $\{L_k\}$, leaves \mathcal{L} invariant [44]. Consequently, \mathcal{L} can be block-diagonalized according to U , with each block corresponding to an eigenvalue of U . Moreover, if the steady state is unique, it will also exhibit this symmetry.

2.1.5.3 \mathbb{Z}_p symmetry

The simplest symmetry a system can possess is \mathbb{Z}_p , which the special case of $p = 2$ corresponding to parity symmetry. The associated operator to the symmetry is $Z_p = e^{i\frac{2\pi}{p} a^\dagger a}$, which corresponds to the situation where the Lindbladian is invariant under the transformation $a \rightarrow ae^{-i\frac{2\pi}{p}}$. This symmetry is characterized by:

$$[Z_p, \mathcal{L}] = 0 \iff [Z_p, H] = [Z_p, L_k] = 0 \iff \mathcal{L}^\dagger Z_p = \dot{Z}_p = 0 \implies [Z_p, \mathcal{L}] = 0 \quad (24)$$

Assuming that the symmetry is conserved in time, it is possible to construct p conserved quantities, each corresponding to the projectors onto the p different symmetry sectors ($\{\Pi_n\}_{n=1}^p$) [39, 40, 45]. Consequently, the set of projectors onto the subspaces of Z_p allows \mathcal{L}_{ss} to be block-diagonalized into p^2 subspaces [45], which evolve independently under \mathcal{L} [45]. Moreover, there will be at least p subspaces containing with one steady state each.

On the other hand, if the operator Z_p commutes with \mathcal{L} , then the parity of the initial state will be conserved in time:

$$Z_p |\rho(t)\rangle\rangle = Z_p T \left[e^{\int_{t_0}^t \mathcal{L}(s)} \right] |\rho(0)\rangle\rangle = T \left[e^{\int_{t_0}^t \mathcal{L}(s)} \right] Z_p |\rho(0)\rangle\rangle = T \left[e^{\int_{t_0}^t \mathcal{L}(s)} \right] z_{p,n} |\rho(0)\rangle\rangle = z_{p,n} |\rho(t)\rangle\rangle \quad (25)$$

2.1.6 Adiabatic theorem of quantum mechanics

In an adiabatic process, there are two characteristic time scales:

- **Internal time**(T_i): The timescale over which the system undergoes internal changes.
- **External time**(T_e): The timescale over which external parameters are varied.

A process is considered adiabatic if $T_e \ll T_i$, meaning that external changes occur more slowly than internal changes.

Theorem: Suppose a Hamiltonian H_i with a discrete spectrum. If the Hamiltonian changes gradually from H_i to H_f , the adiabatic theorem states that the n -th energy level of H_i will correspond with the n -th energy level of H_f [46].

The proof of this theorem can be found in [46].

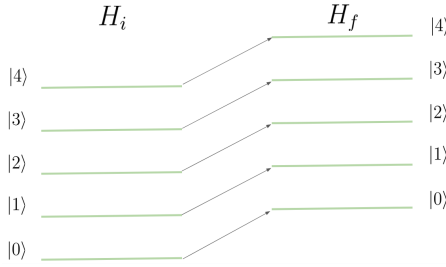


Figure 1: Adiabatic theorem of quantum mechanics

This theorem underlies quantum quantum adiabatic computation, which addresses problems by preparing and evolving the system within the ground state of the Hamiltonian. In this work, we briefly outline the framework, while a more comprehensive study is provided in [47]. The evolution of a quantum system is governed by the Schrödinger equation:

$$i\partial_t |\psi(t)\rangle = H(t)\psi(t) \quad (26)$$

Here, $H(t)$ denotes a time-dependent Hamiltonian that evolves over the interval $t \in [0, T]$. The time can be rescaled using the change of variables $s = \frac{t}{T}$:

$$\frac{i}{T} \partial_s |\psi(s)\rangle = H(s)\psi(s) \quad (27)$$

The dependence of H on s can take various forms; one of the most commonly encountered in the literature is:

$$H(s) = A(s)H_i(s) + B(s)H_f(s) \quad (28)$$

With $A(s=0) = B(s=1) = 1$ and $A(s=1) = B(s=0) = 0$, this defines the form of the Hamiltonians commonly used in quantum annealing applications [19, 20, 21, 22].

Equation 27 shows that the parameter T determines the rate at which the system evolves. Solving the Schrödinger equation for a given time yields a set of N instantaneous eigenstates and eigenvalues of $H(s)$:

$$H(s) |\varepsilon_l(s)\rangle = \varepsilon_l(s) |\varepsilon_l(s)\rangle \quad (29)$$

Here, N denotes the dimension of the Hilbert space. If the energy levels throughout the evolution satisfy [48]:

$$\varepsilon_0(s) \leq \varepsilon_1(s) \quad (30)$$

And the initial state is the ground state of $H(s = 0)$, the system will remain in the instantaneous ground state $|\psi(s)\rangle = |\varepsilon_0(s)\rangle$ [48, 47] throughout the evolution. The adiabatic theorem states that this is guaranteed if the minimum energy gap between the ground state and the first excited state does not close [48]. The adiabatic theorem states:

$$\lim_{T \rightarrow \infty} |\langle \varepsilon_0(1) | \psi(1) \rangle| = 1 \quad (31)$$

The combination of slow evolution and a nonzero energy gap ensures that the system remains close to the instantaneous ground state of $H(s)$ [48].

To verify that the system evolves sufficiently slow, a widely used approximation for the total time evolution is given by [48, 47, 49]:

$$\frac{1}{T} \max_{s \in [0,1]} \frac{|\langle \varepsilon_i(s) | \partial_s H(s) | \varepsilon_j(s) \rangle|}{\Delta^2} \ll 1 \quad \forall j \neq i \quad (32)$$

It is evident that the energy gap Δ strongly influences the total time required for adiabatic computation [20, 21].

2.1.7 Quantum Optics

2.1.7.1 Coherent states and displacement operator

A coherent state is an eigenstate of the annihilation operator:

$$a |n\rangle = \sqrt{n} |n-1\rangle$$

$$a^\dagger |n\rangle = \sqrt{n+1} |n+1\rangle \quad (33)$$

$$a |\alpha\rangle = \alpha |\alpha\rangle$$

They are also called Glauber states [50]. As discussed in [50], the name refers to the fact that light fields are perfectly coherent in these states. Furthermore, they can be generated using high quality lasers [51].

Since the annihilation operator is a non-hermitian operator, its eigenvalues are complex. As discussed in [50], coherent states provide the closest quantum description to the wavelike states of an electromagnetic oscillator. Because the wave behavior of light is typically treated as classically, the coherent states are often considered as classical states in quantum optics. The amplitude of the wave represented by the coherent state corresponds directly to its eigenvalue.

Coherent states are closely related to the Fock states of the harmonic oscillator:

$$H = a^\dagger a + \frac{1}{2} = N + \frac{1}{2} \quad (34)$$

The eigenstate of the harmonic oscillator, $|n\rangle$, represent the occupation number of each energy state. Additionally, the quantum state $|n\rangle$ can be interpreted as the system having n excitations. In this context, the vacuum state corresponds to $|0\rangle$, which is also coherent state with 0 amplitude.

The expected value of the harmonic oscillator Hamiltonian is:

$$\langle H \rangle_\alpha = |\alpha|^2 + \frac{1}{2} \quad (35)$$

There are two contributions to the energy; the first, $|\alpha|^2$ corresponds to the classical wave intensity, while the second $\frac{1}{2}$, represents the vacuum energy.

Furthermore, a relevant property of the coherent states is that they are states of balanced minimal uncertainty:

$$\Delta q = \Delta p = \frac{1}{\sqrt{2}} \quad (36)$$

Moreover, a phase shift by an angle θ changes only the argument of the amplitude α :

$$U(\theta) |\alpha\rangle = ||\alpha|e^{-i\theta}\rangle \quad (37)$$

This reflects the characteristic wavelike behavior. Furthermore, the displacement operator is introduced as:

$$D(\alpha) = e^{\alpha a^\dagger - \alpha^* a} \quad (38)$$

It is a unitary operator that produces a displacement α in the amplitude of a :

$$D^\dagger(\alpha) a D(\alpha) = a + \alpha \quad (39)$$

This property is demonstrated in [50]. An interesting and very useful feature of coherent states is that they can be expressed in terms of the vacuum state as:

$$|\alpha\rangle = D(\alpha) |0\rangle \quad (40)$$

Therefore, any coherent state can be interpreted as a displacement of the vacuum state. Moreover, the wave amplitude can be decomposed into its real and imaginary parts:

$$\alpha = \frac{1}{\sqrt{2}} (q_0 + ip_0) \quad (41)$$

Coherent states are not orthogonal states. Therefore, their scalar product is given by:

$$\langle \alpha' | \alpha \rangle = e^{-\frac{1}{2}(|\alpha|^2 + |\alpha'|^2) + \alpha'^* \alpha} \quad (42)$$

Therefore, the completeness relation is given by:

$$I = \frac{1}{2\pi} \int dq_0 dp_0 |\alpha\rangle \langle \alpha| \quad (43)$$

This means that the basis is over-complete, as a consequence of the states not being orthogonal.

2.1.7.2 Squeezed states and squeezing operator

As discussed previously, coherent states are physical states that have minimal uncertainty:

$$\Delta q = \Delta p = \frac{1}{\sqrt{2}} \quad \Delta q \Delta p = \frac{1}{2} \quad (44)$$

However, coherent states are not the only ones that saturate the Heisenberg uncertainty principle, since the variances of quantum states do not necessarily have to be equal to $\frac{1}{2}$. The uncertainty of one quadrature can be squeezed below the vacuum level ($\frac{1}{2}$) at the expense of an increases uncertainty in the canonically conjugate quadrature [50]. Therefore, the uncertainty of a squeezed state can be expressed as:

$$\Delta q = \frac{1}{2}e^{-2\xi} \quad \Delta p = \frac{1}{2}e^{2\xi} \quad (45)$$

Here, the parameter ξ represents the strength of the squeezing. Furthermore, it is straightforward to verify that the product of uncertainties saturates the Heisenberg inequality, and that a decrease in the uncertainty of one quadrature produces an increase in the other.

Moreover, these relations show that the actual effect of squeezing is a rescaling of the quadratures. As is discussed in [50], this effect is manifested in the wave function as:

$$\varphi(q) = e^{\xi/2}\psi_0(e^\xi q) \quad \tilde{\varphi}(q) = e^{-\xi/2}\tilde{\psi}_0(e^{-\xi}p) \quad (46)$$

As is shown in [50], the operator that produces this transformation is:

$$S(\xi) = e^{\frac{\xi}{2}(a^2 - (a^\dagger)^2)} \quad (47)$$

This operator is known as the squeezing operator. Therefore, the squeezed-vacuum states can be defined as:

$$|\xi\rangle = S(\xi)|0\rangle \quad (48)$$

Furthermore, all minimum-uncertainty states are displaced squeezed-vacuums states:

$$|\alpha, \xi\rangle = D(\alpha)S(\xi)|0\rangle \quad (49)$$

On the other hand, the parameter ξ can be interpreted as the product of time and a coupling constant, which allows the squeezing operator to be regarded as an evolution operator. This makes it possible to identify:

$$H \propto a^2 - (a^\dagger)^2 \quad (50)$$

As the Hamiltonian that produces the squeezing of a quantum state.

The squeezing operator satisfies the following relations:

$$\begin{aligned} S^\dagger(\xi)qS(\xi) &= qe^{-\xi} \\ S^\dagger(\xi)pS(\xi) &= pe^{+\xi} \end{aligned} \quad (51)$$

$$S^\dagger(\xi)aS(\xi) = a \cosh \xi - a^\dagger \sinh \xi$$

The energy of a state of the form $|\psi\rangle = D(\alpha)S(\xi)|0\rangle$ is:

$$\langle H \rangle_\psi = |\alpha|^2 + \frac{1}{2} + \sinh^2 \xi \quad (52)$$

The first term corresponds to the energy contribution of the coherent part due to the amplitude of the state. The second term represents the contribution of the vacuum. Finally, the third term accounts for the fluctuation energy of the squeezed states.

2.2 Kerr Parametric Oscillators

2.2.1 KPO model

In the rotating frame L, the Kerr parametric oscillators (KPO) has the following Hamiltonian:

$$H = \Delta a^\dagger a + \frac{K}{2} (a^\dagger)^2 a^2 - \frac{p}{2} [a^2 + (a^\dagger)^2] \quad (53)$$

Here, Δ is the detuning of the oscillator's eigenfrequency, K is the Kerr coefficient representing the strength of the Kerr nonlinearity, and p is the pump amplitude for the parametric drive [1].

As is described in [1], this oscillator can be used for the deterministic generation of cat states via quantum adiabatic evolution. To achieve this task, the parametric drive is made time-dependent, $p = p(t)$, so that the Hamiltonian becomes $H = H(t)$. The system starts at $p = 0$, where the ground state of the Hamiltonian is the vacuum state $|0\rangle$. Then, the parametric drive $p(t)$ is increased slowly according to an adiabatic schedule. This slow evolution ensures that the system remains in the instantaneous ground state of $H(t)$. The increase of the parametric drive enhances the nonlinear terms in the Hamiltonian, causing the system to undergo a bifurcation. As a result, the instantaneous ground state deviates from the vacuum state. When the parametric drive is increased such that $p \gg \Delta$, the detuning term becomes negligible, and the effective Hamiltonian reduces to:

$$H \approx \frac{K}{2} (a^\dagger)^2 a^2 - \frac{p}{2} [a^2 + (a^\dagger)^2] \quad (54)$$

For this Hamiltonian, the ground state is degenerate and consist on a linear combination of coherent states ($a|\alpha\rangle = \alpha|a\rangle$):

$$|\text{Ground}\rangle \sim |\sqrt{p/K}\rangle \pm |-\sqrt{p/K}\rangle \quad (55)$$

Since the initial state prior to the adiabatic evolution is the vacuum state $|0\rangle$, which is symmetric under parity inversion ($a \rightarrow -a$), the final state after the evolution, for p large enough, will be the symmetric cat state [1]:

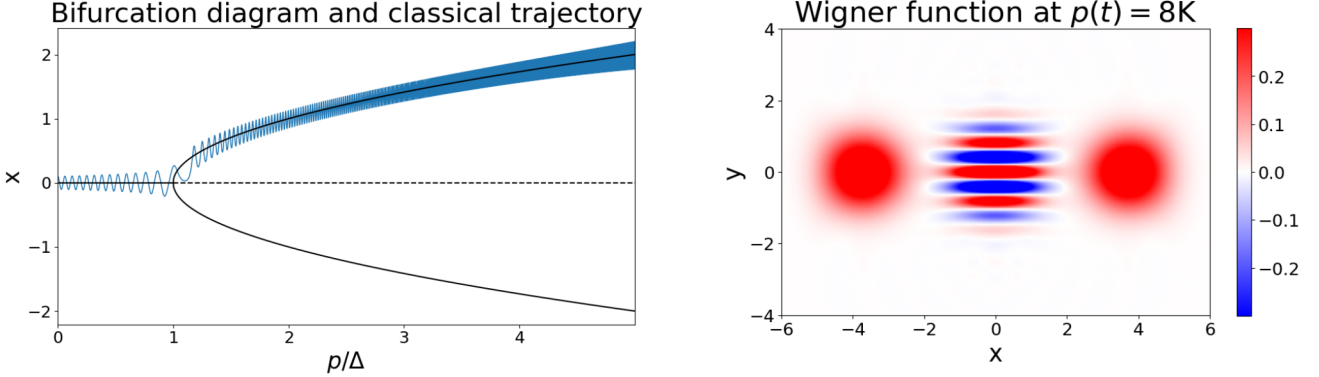
$$|\text{Ground}\rangle \sim |\sqrt{p/K}\rangle + |-\sqrt{p/K}\rangle \quad (56)$$

The generation of these cat states has been discussed in [1] through an analysis of the mean-field equations:

$$\begin{aligned} \dot{x} &= y [\Delta + p + K(x^2 + y^2)] \\ \dot{y} &= x [-\Delta + p - K(x^2 + y^2)] \end{aligned} \quad (57)$$

Here, x denotes the position and y the momentum. These equations has been obtained in the Heisenberg picture using the mean-field approximation. The mean-field analysis shows that the system undergoes Pitchfork bifurcation at $p = \Delta$. Beyond this point, two stable branches appears at $x = \pm\sqrt{(p - \Delta)/K}$. Therefore, before the phase transition, the ground state of the system remain the vacuum state. After the phase transition, cat states are generated.

Classically, after the bifurcation, the system must settle into one of the two stables branches. However, in the quantum regime, the state of the system can exists as a linear superposition of both branches, which corresponds to the generation of a cat state:



Phase transition of the mean-field analysis of the KPO oscillator. The system undergoes a Pitchfork bifurcation at $p = \Delta$, where two stable branches emerge. In the classical regime, the system selects one of these branches for its evolution.

Wigner function of the final quantum state after adiabatic evolution. This quasi-probability distribution exhibits two distinct lobes and a correlation region between them, indicating that the final state is a quantum superposition of the two classical branches. Each of these lobes corresponds to one of the branches emerging after the bifurcation.

Table 2: Left: Bifurcation diagram of the mean-field approximation. Right: Wigner function of the final quantum state after adiabatic evolution.

2.2.2 Quantum computation with a KPO network

This non-linear oscillator can be used to perform quantum adiabatic computation [1]. If N_o KPO oscillators are coupled, after the bifurcation they will generate cat states, that produces a superposition of 2^{N_o} states. By defining a suitable coupling between the oscillators, these states can be used to solve combinatorial optimization problems. Building on this idea, [1] proposes a network of these non-linear oscillators to solve the Ising problem. To achieve this task, the following Hamiltonian is proposed:

$$H = \sum_{i=1}^{N_o} \Delta_i a_i^\dagger a_i + \frac{K}{2} \left(a_i^\dagger \right)^2 a_i^2 - \frac{p}{2} \left[a_i^2 + \left(a_i^\dagger \right)^2 \right] - \frac{\xi_0}{2} \sum_{i=1}^{N_o} \sum_{j=1}^{N_o} J_{ij} \left(a_i^\dagger a_j + a_j^\dagger a_i \right) \quad (58)$$

Here, $J_{ij} = J_{ji}$ are the coupling weights of the Ising model, ξ_0 is a coupling constant with dimensions of energy, and Δ_i is the detuning of each KPO. Just as the Ising model, the coupling has a symmetry by the exchange of all the spins, $E_{\text{ISING}}(\vec{s}) = E_{\text{ISING}}(-\vec{s})$, this Hamiltonian exhibits a symmetry by the exchange of all the annihilation operators, $a_i \rightarrow -a_i$.

As discussed in [1], this network can be used to solve the Ising model if the detuning frequencies are set to:

$$\Delta_i = \xi_0 \sum_{i=1}^{N_o} |J_{ij}| \quad (59)$$

These detuning frequencies ensure that the Hamiltonian is positive semidefinite. This condition is required to ensure that the ground state of the Hamiltonian is still the vacuum state $|0\rangle$ when $p = 0$, which is the required starting point for the generation of the cat states.

The system is initialized in the ground state $|0\rangle$ with $p = 0$. For $t > 0$, the photon pump is increased linearly and very slowly over time, until the non-linear term becomes of order K . At this point, if p is large enough, the detuning Δ_i and coupling $\xi_0|J_{ij}|$ become a perturbation of the non-linear Hamiltonian:

$$H = \sum_{i=1}^{N_o} \frac{K}{2} \left(a_i^\dagger \right)^2 a_i^2 - \frac{p}{2} \left[a_i^2 + \left(a_i^\dagger \right)^2 \right] \quad (60)$$

Under these conditions, if the couplings between the oscillators were set to zero, then the generated state after the bifurcation would correspond to a superposition of all the tensor product combinations of the coherent states $|\pm\sqrt{p/K}\rangle$. However, $\xi_0 J_{ij}$ is small but not zero, so it can be treated as a perturbation of the non-linear Hamiltonian. Therefore, the correction to the energy for the tensor product $\otimes_{i=1}^{N_o} |s_i \sqrt{p/K}\rangle$ is given by [1]:

$$E_{\text{corr}}(s) = \frac{p}{K} \sum_{i=1}^{N_o} \Delta_i - \xi_0 \frac{p}{K} \sum_{i=1}^{N_o} \sum_{j=1}^{N_o} J_{ij} s_i s_j \quad (61)$$

Here, the first term depends on the detuning of the system, while the second is proportional to the Ising energy. Therefore, the new ground state of the system is the one that minimizes the Ising energy.

Therefore, since the system has a symmetry $a_i \rightarrow -a_i$, the new ground state of the system is:

$$|\psi_f\rangle = \frac{1}{\sqrt{2(1 + e^{-2N_o p/K})}} \left(\otimes_{i=1}^{N_o} |s_i \sqrt{p/K}\rangle + \otimes_{i=1}^{N_o} |-s_i \sqrt{p/K}\rangle \right) \quad (62)$$

The relative phase between the states is positive due to the fact that the initial state is $|0\rangle$, which has an even parity.

Therefore, by measuring the signs of the KPO amplitudes ($s_i \sqrt{p/K}$) using the PVM defined in 3.1 on the final quantum state after the evolution, the solution to the Ising model is obtained from the sign $s_i \in \{-1, 1\}$ of each amplitude.

2.2.3 Ising model with an external field

As discussed in [24], this model can be generalized to include the situation in which the Ising model is subject to an external field \vec{h} . In that situation, the proposed Hamiltonian is:

$$H = \sum_{i=1}^{N_o} \Delta_i a_i^\dagger a_i + \frac{K}{2} \left(a_i^\dagger \right)^2 a_i^2 - \frac{p}{2} \left[a_i^2 + \left(a_i^\dagger \right)^2 \right] - \frac{\xi_0}{2} \sum_{i=1}^{N_o} \sum_{j=1}^{N_o} J_{ij} \left(a_i^\dagger a_j + a_j^\dagger a_i \right) + \sigma(t) \xi_0 \sum_{i=1}^{N_o} h_i \left(a_i + a_i^\dagger \right) \quad (63)$$

Here, a new term has been added to the Hamiltonian, accounting for the external drive. This new term is proportional to the function:

$$\sigma(t) = \sqrt{\frac{p(t) - \Delta \tanh(p(t)/\Delta)}{K}} \quad (64)$$

The time-dependent amplitude of the external field has been selected to be $\sigma \approx 0$ when $t = 0$. This property ensure that the Hamiltonian is still positive semidefinite when $p = 0$. For long times, $\sigma \approx \sqrt{(p - \Delta)/K}$, which corresponds to the amplitude of the states. This is done to ensure that both terms of the Ising energy are at the same order at the end of the adiabatic evolution.

The addition of this new term breaks the symmetry $a_i \rightarrow -a_i$. Therefore, the new ground state of the system after the bifurcation is:

$$|\psi_f\rangle = \otimes_{i=1}^{N_o} |s_i \sqrt{p/K}\rangle \quad (65)$$

Therefore, the correction to the total energy, when $p \gg \Delta$, is:

$$E_{\text{corr}}(s) = \frac{p}{K} \sum_{i=1}^{N_o} \Delta_i - \xi_0 \frac{p}{K} \sum_{i=1}^{N_o} \sum_{j=1}^{N_o} J_{ij} s_i s_j + 2\xi_0 \frac{p}{K} \sum_{i=1}^{N_o} h_i s_i \quad (66)$$

2.3 Dissipative oscillator

A model of a driven-dissipative oscillator with both linear and non-linear dissipation is presented in [2, 34]:

$$\dot{\rho}(t) = -i[H_n, \rho] + \gamma_1 \mathcal{D}[a]\rho + \gamma_m \mathcal{D}[a^m]\rho \quad (67)$$

Where the Hamiltonian on the rotation frame, after the parametric approximation, is given by:

$$H_n = \Delta a^\dagger a + i\eta \left[a^n e^{in\theta} - (a^\dagger)^n e^{-in\theta} \right] \quad (68)$$

This Hamiltonian describes the dynamics of an oscillator undergoing an $n > 0$ photon-exchange process at frequency ω_s . The first term represents the harmonic oscillator dynamic, with $\Delta = \omega_0 - \omega_s$ being the detuning between the natural frequency ω_0 of the system and the driving frequency ω_s . The second term accounts for the n -photon exchange induced by a photon pump acting on the system. The driving strength is controlled by the parameter η , and θ denotes its phase. The presence of this term introduces a squeezing effect on the states, [2].

The system is coupled to two environments through two Lindblad dissipators. The first, associates with the operator a , corresponds to single-photon loss with rate γ_1 . The second describes the loss of m photons at rate γ_m with $m > 1$.

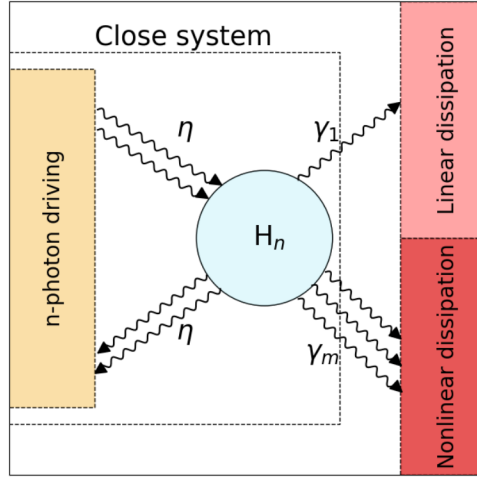


Figure 2: Sketch of the dissipative oscillator described by 67. The oscillator undergoes an n -photon exchange process driven with strength η . It is coupled to a linear environment with coupling constant γ_1 , representing single-photon losses, and to a non linear environment leading to m -photons losses at rate γ_m with $m > 1$.

This oscillator exhibit a \mathbb{Z}_n symmetry ($a \rightarrow ae^{i\frac{2\pi}{n}}$) which leaves \mathcal{L} invariant when $n = m$, [41]. As is discussed in [41], the system may present either a weak or a strong symmetry depending on the commutation relations with the operator $Z_n = e^{i\frac{2\pi}{n}a^\dagger a}$. The symmetry is strong when the operator Z_n commutes with both the Hamiltonian and the jump operators:

$$[Z_n, H_n] = [Z_n, a] = [Z_n, a^m] = 0 \quad (69)$$

This is achieved in the case of $\gamma_1 = 0$, which implies the existence of a conserved quantities corresponding to the projectors onto the different symmetry sectors of Z_n .

On the other hand, if $\gamma_1 > 0$, the symmetry will becomes a weak symmetry, since the conditions of 69 are no longer satisfied. In this case, the superoperator $\mathcal{Z}_n = Z_n(\cdot)Z_n$ will commute with the Lindbladian:

$$[\mathcal{L}, \mathcal{Z}_n] = 0 \quad (70)$$

This oscillator has been extensively studied in the literature, and it has been shown that at least one steady state exists in the case of $n = m$ for infinite dimension [52]. However, the situation becomes more involved when $n \neq m$.

These results can be generalized to the case $n \neq m$, as discussed in [2]. In this scenario, the condition of $\gamma_1 = 0$ does not guarantee the presence of a strong symmetry. It is also required that the operator $Z_p = e^{i\frac{2\pi}{p}a^\dagger a}$ commutes with the jump operators [39, 40]:

$$[Z_p, a^n] = [Z_p, a^m] = 0 \longrightarrow \gcd(n, m) = p > 1 \quad (71)$$

As is discussed in [2], a strong symmetry arises when m is not coprime with n , whereas if $\gcd(n, m) = 1$, the system exhibits only a weak symmetry, with $[\mathcal{L}, Z_n] = 0$. Furthermore, p determines both the number of steady states and the block structure of \mathcal{L} . In the following, we assume the system operates in the strong-symmetry regime, since this is the case of interest in the present work. Due to the symmetry, the Liouvillian can be diagonalized into p^2 sectors [40, 45]:

$$\mathcal{L} = \bigoplus_{\mu, \nu=1}^p B_{\mu, \nu} \quad (72)$$

Among these p^2 independent sectors, at least p subspaces will have their own steady state [40]. These subspaces correspond to $\{B_{\mu, \mu}\}_{\mu=1}^p$. The remaining sectors contain coherences that decay in the long-time limit [2, 40].

The steady state of the oscillator, for both weak and strong symmetry, can be expressed in terms of squeezed coherent states as:

$$|\alpha, \xi\rangle = D(\alpha)S(\xi)|0\rangle \quad (73)$$

Furthermore, the squeezing parameter ξ_j for lobe j can be approximated as [2]:

$$\xi_j = se^{2i\theta_j + iH(n-m)\frac{\pi}{2}} \text{ for } j = 1, \dots, n \quad (74)$$

Here, $H(x)$ is the Heaviside function, and s represents the squeezing strength.

The mean-field results in [2] provide the phase of the coherent lobes of the steady state $\alpha_j = re^{i\theta_j}$ with $\theta_j = \theta_0 + (2j+1)/n$ for $j = 1, \dots, n$. Due to the rotational symmetry, it can be assumed that the amplitude r and the squeezing strength s are the same for each lobe.

Finally, there are p steady states, which are coherent superpositions of the lobes. For instance, the steady state belonging to the symmetry sector $\mu = 1$ is [2]:

$$\rho = |\psi_{ss}\rangle \langle \psi_{ss}| \text{ with } |\psi_{ss}\rangle = \frac{1}{\sqrt{p}} \sum_{j=1}^p |\alpha_j, \xi_j\rangle \quad (75)$$

2.3.1 Generation of the cat states

The oscillator has, as a particular case, $(n, m) = (2, 4)$, for which the steady states are cat states [2]. Particularizing the mean-field approximation derived in [2] for the special case of strong symmetry ($\gamma_1 = 0$), $(n, m) = (2, 4)$, and $\theta = \frac{\pi}{2}$ to generate cat states along the position quadrature, yields:

$$\dot{\alpha} = -i\Delta\alpha + 2\eta\alpha^* - 2\gamma_m |\alpha|^6 \alpha \quad (76)$$

Using this approximation, the conditions for the appearance and the coherence phase of the cat states in the steady state are computed in D:

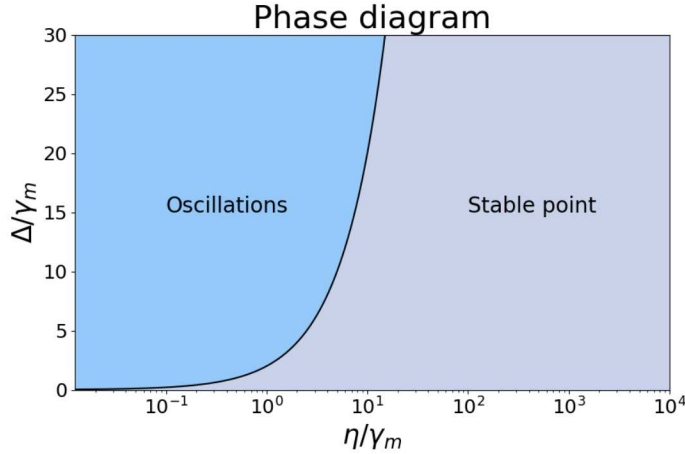


Figure 3: Phase diagram of the dissipative oscillator introduced in [2] for the special case $\gamma_1 = 0$ and $(n, m) = (2, 4)$ (strong symmetry). The diagram was obtained by solving the mean-field equations derived in [2] for the parameters of interest. The system initially exhibits a phase where the linear stability analysis reveals purely imaginary eigenvalues. In this regime, the oscillator undergoes oscillations in both position and momentum. Conversely, when the pump falls below the threshold $\frac{\Delta}{\eta} = 2$, two new stable fixed points emerge, corresponding to the coherence phases of the cat state.

It is important to recall that the mean-field approximation provide information only about the coherence phase of the state and does not determine the squeezing. Therefore, the results obtained for the states remain undetermined with respect to the squeezing parameter ξ . The mean-field analysis shows that for $\frac{\Delta}{\eta} > 2$, there exists a single steady state corresponding to a vacuum squeezed state $|0, \xi\rangle \langle 0, \xi|$, which is associated with the trivial solution $\alpha = 0$. In this regime, the linear stability analysis identifies this point as a center, so oscillations in position and momentum are expected. However, when the driving strength increases such that $\frac{\Delta}{\eta} \leq 2$, the system undergoes a phase transition: the squeezed vacuum becomes an unstable, and two new stable points emerge. These points correspond to the coherence phases of the squeezed coherent states that form the cat states:

$$\alpha = \left(\frac{\eta}{2\gamma_m} \right)^{1/6} \left(4 - \left(\frac{\Delta}{\eta} \right)^2 \right)^{1/12} \left\{ \pm \cos \left[\frac{1}{2} \arctan \left(\frac{\Delta}{\eta \sqrt{4 - \left(\frac{\Delta}{\eta} \right)^2}} \right) \right] \right. \\ \left. \mp i \sin \left[\frac{1}{2} \arctan \left(\frac{\Delta}{\eta \sqrt{4 - \left(\frac{\Delta}{\eta} \right)^2}} \right) \right] \right\} \quad (77)$$

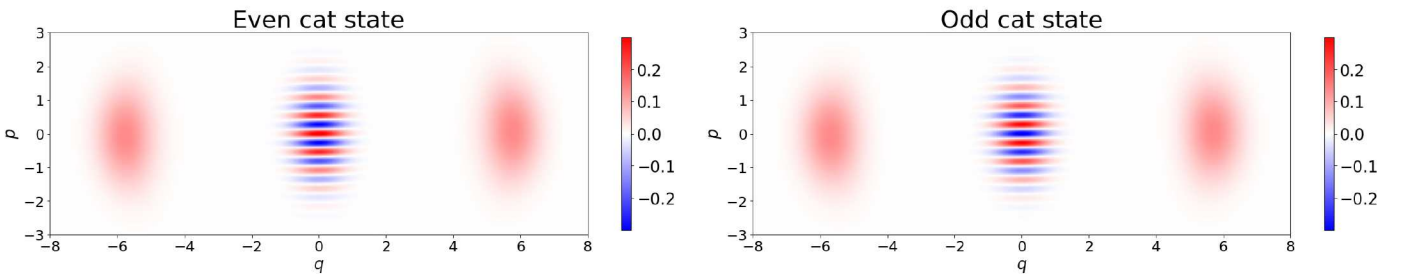


Figure 4: Even and odd cat states generated with $\Delta = 200\gamma_m$ and $\eta = 2000\gamma_m$ in a Hilbert space of dimension $\dim \mathcal{H} = 50$.

In this special case, the oscillator exhibits a \mathbb{Z}_2 symmetry, which allows the Lindbladian \mathcal{L} to be block-diagonalized into 4 sectors according to the eigenvalues of \mathcal{Z}_2 . Among these 4 blocks, two of them ($B_{1,1}, B_{2,2}$) contain steady states, corresponding to states with positive or negative parity. Therefore, after the bifurcation, the system exhibits two steady states, each associated with a defined parity:

$$|\text{CAT}^\pm\rangle = C(|\alpha, \xi\rangle \pm |-\alpha, \xi\rangle) \quad (78)$$

Here, C corresponds to a normalization factor, while the phase α is determined from the mean-field approximation. If the squeezing effect is neglected and the coherence amplitude is large enough, both states can be considered almost orthogonal, which set the normalization factor to $C = \frac{1}{\sqrt{2}}$. Therefore, after the bifurcation, the oscillator can simultaneously follow both branches of the bifurcation behaviour that contrast with the classical case, where the system must select only one branch.

Furthermore, an analysis of the Lindbladian spectrum through simulations shows that before the bifurcation, there are two eigenvalues equals to zero. However, examining the corresponding right eigenoperators of the superoperator reveals that only one of them is a density matrix, while the other is an hermitian non-positive operator. This valid density matrix has positive parity, so it is restricted to the Lindbladian sector corresponding to Z_2 and will evolve into even cat state after the bifurcation. The other operator, which is not a density matrix below $\frac{\Delta}{2}$, will rise to the odd cat state.

Therefore, using approach proposed in [1], this oscillator can be employed for the deterministic generation of cat states with either odd or even parity. To achieve this, the driving strength is taken as a time-dependent parameter $\eta(t)$. For this study, the chosen time dependence will be:

$$\eta(t) = \eta_f \tanh\left(\frac{t}{\tau}\right) \quad (79)$$

Here, η_f represents the final driving strength reached at long times, while the parameter τ controls the rate at which $\eta(t)$ approaches η_f . The specific time dependence has been chosen to be the hyperbolic tangent because it is upper bounded for times larger than τ , allowing the system to reach a steady state. Moreover, τ provides a way to regulate the speed of changes in the system. Finally, since Z_2 commutes with the Hamiltonian for any η , the symmetry \mathbb{Z}_2 remain preserved throughout the evolution.

To deterministically generate a cat state, the system is initialized with $\eta = 0$ and a final driving strength η_f above the bifurcation threshold $\eta_f > \frac{\Delta}{2}$. The oscillator should start in an initial state with the parity corresponding to the cat state that is intended to be generated. Since the parity is a conserved symmetry of the system, the projectors onto the two parity sectors remain conserved quantities throughout the evolution [40, 45]:

$$\Pi_\pm = \frac{1}{2}(I \pm Z) \quad (80)$$

Therefore, the parity of the initial state uniquely determines which cat state will be generated after the bifurcation. Moreover, the expectation values of the conserved parity projectors can be used as indicators to verify whether the cat states are being properly produced. Once the initial state is prepared, the system will evolve while the driving strength increases according to 79. When the driving strength exceeds the threshold $\frac{\Delta}{2}$, the desired cat state emerges.

These features makes this oscillator a promising candidate for implementing quantum adiabatic computation, in close analogy with the Kerr parametric oscillators of [1]. To verify the feasibility of such approach, an analysis of the spectrum of H_2 is done:

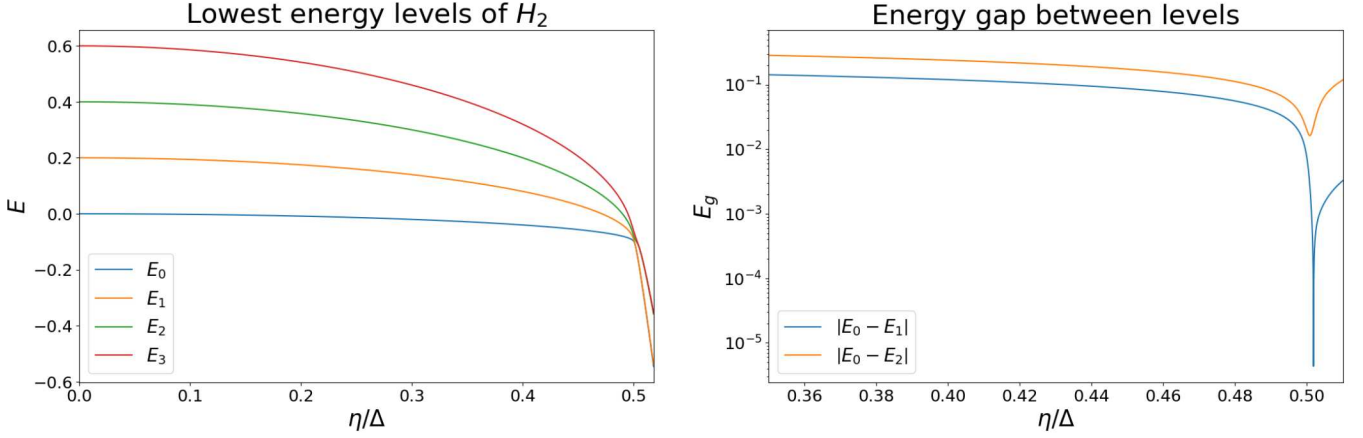


Figure 5: Lowest energy levels of H_2 as a function of the parameter η for $\frac{\Delta}{\eta_f} = 1.904761$.

The increase in the driving strength produces a decrease in the energy levels, which at second-order perturbation theory is given by $E^{(2)} = -\frac{n}{\Delta}\eta^2$. This implies that the driving reduces the energies of all the levels differently, proportional to their quantum number. However, numerical observation show that at the bifurcation all the levels approach the ground state, and then separates again after the bifurcation. In particular, the energy gap between the ground state and the first state becomes very close near the bifurcation, which is undesirable for quantum adiabatic computing. However, it is not a problem since these two states have different parities. Consequently, if the initial state is prepared with a well-defined parity, transitions between the ground state and the first excited state are forbidden by symmetry, allowing quantum adiabatic computation to proceed safely.

3 Methodology

3.1 Success probability of a configuration \vec{S}

The success probability of a configuration \vec{S} or $\{S_i\}_{i=1}^{N_o}$ is defined as the probability that the signs $\{s_i\}_{i=1}^{N_o}$ of the coherent states $\{|s_i|\alpha\rangle\}_{i=1}^{N_o}$ of each oscillator match with the signs of the target configuration $\{S_i\}_{i=1}^{N_o}$.

The quantum state can be expressed as:

$$|\psi\rangle = C_n \left(\otimes_{i=1}^{N_o} |s_i f(t)\rangle + \otimes_{i=1}^{N_o} |-s_i f(t)\rangle \right) \quad (81)$$

Here, C_n represent the normalization constant. Therefore, the success probability of the configuration $\{S_i\}_{i=1}^{N_o}$ corresponds to the probability that the first oscillator has sign $S_1 = s_1$, the second $S_2 = s_2$, and so on.

Since the function $f(t) \in \mathbb{R}$, the coherent states have real amplitudes, and the imaginary component does not affect the probability. Therefore, only the sign alignment contributes to the probability estimation.

Thus, the probability of a configuration \vec{S} is:

$$P(\vec{S}) = \int_{S_1} \int_{S_2} \cdots \int_{S_{N_o}} dx_1 dx_2 \cdots dx_{N_o} \int_{\mathbb{R}} \int_{\mathbb{R}} \cdots \int_{\mathbb{R}} dy_1 dy_2 \cdots dy_{N_o} W(x_1, x_2, \dots, x_{N_o}, y_1, y_2, \dots, y_{N_o}) \quad (82)$$

Here, the integral \int_{S_i} depends on the value of the spin S_i :

$$\int_{S_i=1} = \int_{\mathbb{R}^+} \quad \int_{S_i=-1} = \int_{\mathbb{R}^-} \quad (83)$$

Therefore, using 9, the integral over the momentum can be integrated out:

$$P(\vec{S}) = \int_{s_1} \int_{s_2} \cdots \int_{s_{N_o}} dx_1 dx_2 \cdots dx_{N_o} \rho(x_1, x_2, \dots, x_{N_o}) \quad (84)$$

This expression allows us to define a measurement operator corresponding to each configuration:

$$M(\vec{S}) = \otimes_{i=1}^{N_o} M_i(S_i) \quad (85)$$

Where:

$$M_i(+) = \int_0^\infty dx_i |x_i\rangle \langle x_i| \quad (86)$$

$$M_i(-) = \int_{-\infty}^0 dx_i |x_i\rangle \langle x_i| \quad (87)$$

M_i are positive measured operators that perform a measurement of the sign of the quadrature amplitude x_i of the i -th oscillator. Therefore, the probability of observing the configuration $\{S_i\}_{i=0}^{N_o}$ can be expressed in term of the density matrix as:

$$P(\vec{S}) = \text{Tr}(\rho M(\vec{S})) \quad (88)$$

Therefore, the PVM $\{M(\vec{S}_i)\}_{i=0}^{2^{N_o}}$ is used to perform projective measurements on the final state in order to obtain the resulting signs of the amplitudes.

3.2 Simulations

In this study, the concept of bifurcation-based adiabatic computation proposed in [1, 24] is analysed. Furthermore, it is implemented using a different nonlinear oscillator [2], which is defined in a dissipative environment. To investigate the oscillators, simulations are performed to study the dynamics of both models under the amplification of nonlinear terms.

These models are defined in infinite-dimensional Hilbert spaces, which cannot be represented in a computer. Therefore, a cutoff $\dim(\mathcal{H}) = N$ is introduced for the Hilbert spaces of the oscillators. This cutoff must be sufficiently large to avoid affecting the outcomes of the simulations. The cutoff is chosen heuristically, taking into account both computational resources **J** required for the simulation and the degree of nonlinearity of the oscillators. The latter influences the choice of cutoff, since higher nonlinearities lead to the occupation of higher configurations in the Hilbert space.

All numerical simulations in this project were performed using the Python library for quantum systems, QuTip [53], which implements numerical methods for solving the Schrödinger equation and the Lindblad master equation. The simulation code is available in [54].

3.2.1 KPO

For the study of KPO oscillators, the amplification of the pump $p(t)$ in the system is modeled as a linear function:

$$p(t) = \frac{p_\Delta}{K} t \quad (89)$$

Where p_Δ is the slope of the increment of $p(t)$, expressed in units of K . The value of p_Δ determines the rate at which changes are introduced into the system. Throughout this study, p_Δ is chosen such that the changes can be considered adiabatic. However, it is important to note that large values of $p(t)$ may introduce cutoff effects in the simulations, leading to non-physical results **B**, **C**.

Furthermore, the cutoff used for this oscillator depends on the number of coupled oscillators. In the case of 4 coupled oscillators, $N = 14$, whereas for 3 oscillators, $N = 20$. The difference in cutoff values arises from computational considerations **J**, **C**: simulations with four coupled oscillators requires significantly greater computational resources than those with three.

3.2.2 Dissipative oscillators

As discussed in 2.3, the driving strength is amplified according to 79. This function differs with the linear increment used for KPO oscillators, since here the goal is for the state to converge to a steady state when $\frac{t}{\tau} \gg 1$, which requires $\eta(t) \rightarrow \eta_f$.

For this oscillator, the cutoff value is set to $N = 30$ when oscillators are coupled, which is higher than in the KPO case. This is because proper cat-state generation occurs in the regime $\frac{\eta}{\gamma_m} \gg 1$. In this regime, the dominant process is the exchange of two photons with the driving field, while dissipation via four-photon emission becomes less relevant. As a result, transitions to higher-energy states appear, making a larger cutoff necessary. The cutoff is chosen heuristically from simulations of the steady state for a single oscillator, by increasing N until the steady state no longer changes with higher values of N and taking into account the computational resources required **J**.

4 Results and discussion

In this study, the KPO oscillator presented in [1] is discussed. As at starting point, it is ensured that the model generates cat states after the bifurcation as discussed in 2.2. Once this has been confirmed, the system of oscillators is applied to solve the Ising model using the quantum computation method described in 2.2.2.

Furthermore, the applicability of the dissipative oscillators introduced in [2] for the quantum computation is studied. First, the mean-field approximation of a single oscillator is validated to ensure its accuracy. Next, the dissipative oscillators are coupled using the interaction term introduced in [1], and the resulting model is analysed within the mean-field framework to determine whether it converges to the states predicted by the approximation. Then, the quantum computation method proposed in [1] is adapted to the dissipative oscillator model of [2]. Finally, this system is used to solve the Ising model, in direct analogy to the KPO case.

Finally, both oscillators are employed to evaluate their performance on more complex problems, such as the Hopfield model [55], as well as the application of this protocol to the computation of an eigenvector associated with specified eigenvalues.

4.1 Result with the KPO oscillators

I begin by studying the case of KPO oscillators to verify the validity of the results reported in [1]. The simulations presented in this section were performed as described in 3.2.1, using the Adams method [56].

4.1.1 Overlap with the theoretical result

The model discussed in 2.2 and presented in [1, 24] predicts the generation of a cat state after the bifurcation, whose coherent amplitudes correspond to the mean-field results. To verify the generation of the cat states after the bifurcation, the Schrödinger equation is solved by the Adams method [56], with the coupling coefficients defined in 2.2. Based on the simulation results and the theoretical cat state after the bifurcation for a configuration of signs $\{S_i\}_{i=1}^{N_o}$, 2.2.2:

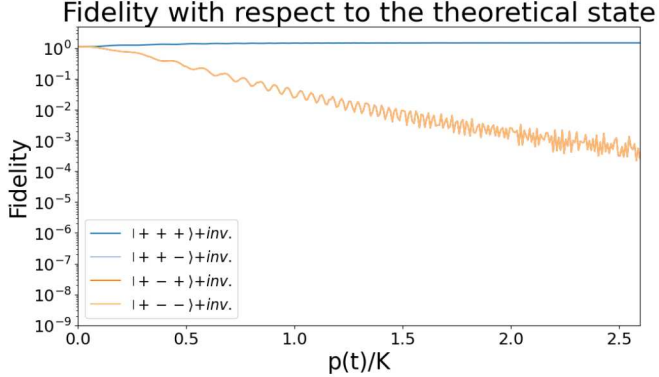
$$\left| \vec{S} \right\rangle = C_n \left(\otimes_{i=1}^{N_o} \left| S_i \sqrt{\frac{p(t)}{K}} \right\rangle + \otimes_{i=1}^{N_o} \left| -S_i \sqrt{\frac{p(t)}{K}} \right\rangle \right) \quad (90)$$

The fidelity between the simulated and the theoretical state 90 after the bifurcation is computed as a function of the pump strength $\frac{p(t)}{K}$, for all the possible configurations of signs \vec{S} :

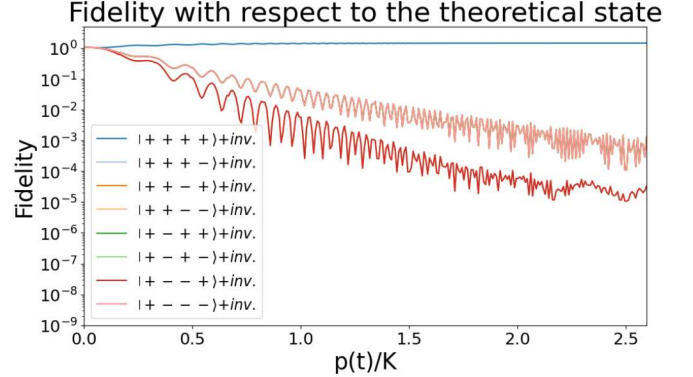
$$F = \left| \langle \vec{S} | \psi \rangle \right|^2 \quad (91)$$

If the theoretical model 2.2 is correct, the fidelity with the configuration $\{S_i\}_{i=1}^{N_o}$ that minimizes the Ising energy will be maximal. Meanwhile, the fidelity with others configurations should approach zero for large values of p .

The obtained results in the simulation:



Overlap between the simulation results and the theoretical state as a function of p for 3 coupled oscillators. The simulation parameters are $p(0) = 0$, $p(1000/K) = 10K$, $\xi_0 = 0.5K$ and $N = 20$.



Overlap between the simulation results and the theoretical state as a function of p for 4 coupled oscillators. The simulation parameters are $p(0) = 0$, $p(800/K) = 8K$, $\xi_0 = 0.5K$ and $N = 14$.

Table 3: Overlap between the simulation and theoretical result $|\psi\rangle \sim \otimes_{i=1}^{N_o} |s_i \sqrt{p/K}\rangle + \otimes_{i=1}^{N_o} |-s_i \sqrt{p/K}\rangle$ as a function of the parameter p . The couplings that has been chosen for the simulation are $J_{ij} = 1 - \delta_{ij}$ (δ_{ij} is the Kronecker delta). Not all configurations are shown in the picture because the symmetry $E(\vec{s}) \rightarrow E(-\vec{s})$ has been exploited. Therefore, each line corresponds to the sum of the fidelity $F(s) + F(-s)$.

Since the couplings have been set to $J_{ij} = 1 - \delta_{ij}$, the ground state for the Hamiltonian will be a configuration with all the spins up or down. These configurations corresponds to $|--- \dots\rangle$ and $|+++ \dots\rangle$. This can be seen in both figures, where the overlap between the simulation state and all the configurations different from the ground state goes to zero. Meanwhile, the fidelity with the lowest energy configuration remain more or less constant.

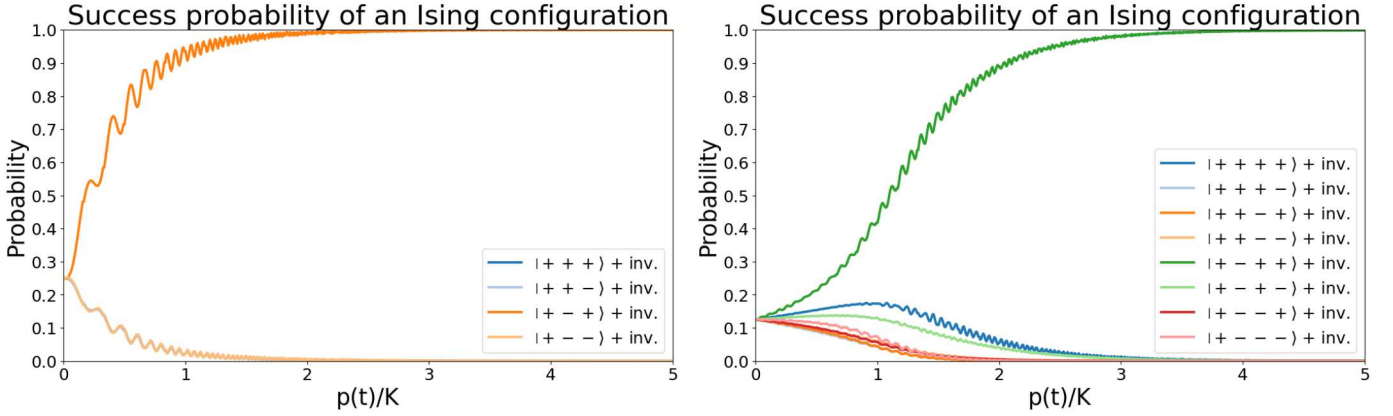
Moreover, a question that may arise is the following: if there is N_o coupled oscillators, and only half of them are plotted due to the inversion symmetry, why are there only 2 and 3 curves in the two figures instead of 4 and 8, respectively? This is because the chosen couplings are $J_{ij} = 1 - \delta_{ij}$, which introduces an additional symmetry in the Ising energy. Specifically, the energy is invariant under the permutations of the spins: $E(s) = pE(s)$, with $p \in S_{N_o}$ is an element of the permutation group of order N_o . As a result, many configurations becomes energetically equivalent, and the number of different energy levels is reduced. Therefore, the results in both figures show that the evolution of a configuration depends solely on its energy, rather than on the individuals values of the spins.

These results demonstrate that the theoretical model successfully generates cat states after the bifurcation. This confirms the validity of the mean-field approximation and the presence of a bifurcation in the model.

4.1.2 Success probability of the Ising model with and without an external field

After confirming that cat states are properly generated, the model is applied to solve the Ising problem with and without an external field. The oscillators are coupled according to 2.2.2, with parameters chosen to remain in the adiabatic regime. The system starts in the vacuum state $|0\rangle$ with $p(0) = 0$, and the pump strength is then increased linearly according to 89 to amplify the non linear terms. The parameter $p(t)$ is increased until the system undergoes the bifurcation, which is the situation where the system solve the Ising model, as discussed in 2.2.2. Therefore, the time-dependent Schrödinger equation is solved using the Adams method [56], and the success probability of each configuration of signs \vec{S} is computed using the PVM introduced in 3.1 as a function of $\frac{p(t)}{K}$. The success probability is plotted as a function of $p(t)/K$ to track the system's evolution. These results will indicate whether the system of oscillators converges to a configuration that solves the Ising model or not. If it does, the success probability of the ground state will be maximized, while the probabilities of the others states will tend to zero.

The obtained results for the simulation:

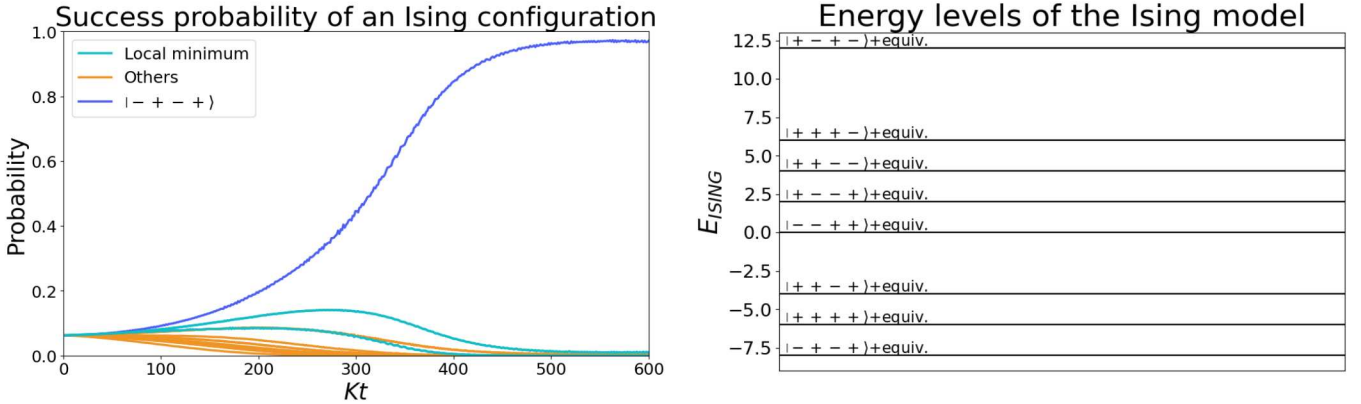


Success probability of each configuration as a function of p for 3 coupled oscillators. The simulation parameters are: $p(0) = 0$, $p(1000/K) = 10K$, $\xi_0 = 0.5K$ and $N = 20$. The couplings that has been chosen for the simulation are $J_{1,2} = -1.4$, $J_{1,3} = 0.8$ and $J_{2,3} = -0.3$. The ground state correspond with $\vec{s} = (1, -1, 1)$ and $\vec{s}' = (-1, 1, -1)$.

Success probability of each configuration as a function of p for 4 coupled oscillators. The simulation parameters are: $p(0) = 0$, $p(500/K) = 5K$, $\xi_0 = 0.5K$ and $N = 14$. The couplings that has been chosen for the simulation are $J_{1,2} = -1.4$, $J_{1,3} = 0.8$, $J_{1,4} = 0.9$, $J_{2,3} = -0.3$, $J_{2,4} = 1$ and $J_{3,4} = 1.1$. The ground state correspond with $\vec{s} = (1, -1, 1, 1)$ and $\vec{s}' = (-1, 1, -1, -1)$.

Table 4: Success probability of each configuration as a function of p for the Ising model without external field. Not all configurations are shown in the picture because the symmetry $E(\vec{s}) \rightarrow E(-\vec{s})$ has been exploited. Therefore, each line corresponds to the sum of the probabilities $P(s) + P(-s)$.

Both pictures show that the adiabatic evolution converge toward the ground state of the Ising model. Moreover, the speed of the convergence to the ground state in both cases is nearly the same. This result could imply that the time required to reach the solution of the model does not strongly depend on the number of coupled oscillators.



Success probability of each configuration of the Ising model with an external field for 4 coupled KPOs. The system is subject to an external field with $\vec{h} = (3, -2, 2, -3)$. The simulation parameters are: $p(0) = 0$, $p(300/K) = 6K$, $\xi_0 = 0.2K$ and $N = 14$.

Energy levels of the Ising model for 4 spins in an external field $\vec{h} = (3, -2, 2, -3)$.

Table 5: Left: Success probability of each Ising configuration as a function of the parameter p with an external field. The system is subject to an external field $\vec{h} = (3, -2, 2, -3)$, and the chosen couplings are $J_{ij} = 1 - \delta_{ij}$. Right: Energy levels of the Ising model corresponding to the same external field

The picture shows that the success probability of the ground state increases over time. Although the ground state does not reach a probability of 1, its probability is maximized. This instance is more complex than the previous two, as there is now more than one local minimum in the system. Nevertheless, the adiabatic computation is still able to solve the problem.

These results show that the model can be employed to solve the Ising problem with and without an external field. Moreover, the results obtained are consistent with those reported in [1, 24].

4.2 Dissipative oscillators

Now, the dissipative oscillators are studied. The study begins with the mean-field approximation for a single oscillator, followed by an examination of the case in which the oscillators are coupled and their applicability to quantum computation. Finally, the dissipative oscillator is used to solve the Ising model, both with and without an external field, in direct analogy to the procedure applied to the KPO oscillator. The simulations presented in this section were performed as described in 3.2.2, using the Adams method in combination with the quantum jump trajectories [35, 46, 57, 58] approach to simulate the systems.

4.2.1 Validity of the mean field approximation of the dissipative oscillators

The mean-field results provide an approximation of the system dynamics. However, as an approximation, they may fail to match the results obtained from numerical integration of the Lindblad equation. To assess the validity of the mean-field approximation, the Lindblad equation is solved using the Adams method [56], with a driving strength varying according to 79.

The simulation results are plotted as a function of $t\gamma_m$ and compared with the dynamics predicted by the mean-field approximation. In particular, once the system reaches the steady state, the coherence amplitudes obtained from the simulation should correspond to those predicted by the mean-field model. However, after the bifurcation, a cat state is generated, causing the expected value of the annihilation operator to vanish because the state follows both branches of the bifurcation, which cancel each other. In contrast, the mean-field approximation follows classical dynamics and converge to one of the lobes. To assess the convergence to the fixed point, the simulation results are projected onto the positive and negative position axes in the Wigner function representation, using the projector operators defined in 3.1.

Therefore, the results correspond to $\langle a \rangle_\rho$ and $\langle a \rangle_{M\rho M}$ (this is the expected value of the annihilation operator for the density matrix projected onto the positive position quadrature) as a function of $t\gamma_m$, where ρ is the density matrix obtained from the simulation and M is the projector. If the simulation matches the mean-field prediction, the expected values should converge to those predicted by the mean-field.

The obtained results are:

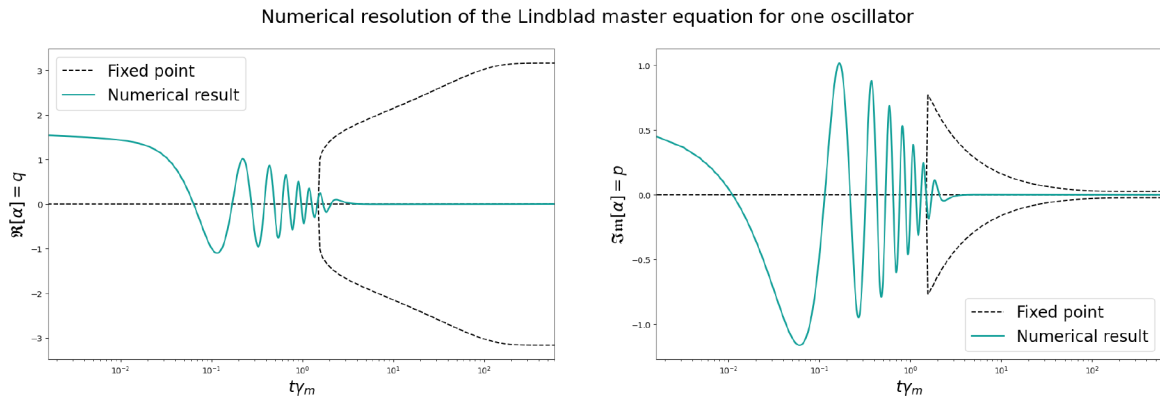


Figure 6: Numerical resolution of the Lindblad equation with $N = 30$, $\eta_f = 1000\gamma_m$, $\Delta = 30\gamma_m$ and $\tau = 100/\gamma_m$

The expectation value of the annihilation operator shows that the oscillators exhibits an oscillatory phase before the bifurcation. However, since the steady state after the bifurcation corresponds to a cat state, the system simultaneously explores both branches. As a consequence, the expectation value of the annihilation operator

vanishes after the bifurcation. This occurs because the contributions from α and $-\alpha$ cancel each other out. To verify the validity of the results beyond the bifurcation, the system's density matrix has been projected onto the positive position quadrature. This procedure avoids the aforementioned cancellation and allows us to confirm whether the simulation converges to the fixed points predicted on the mean-field approximation:

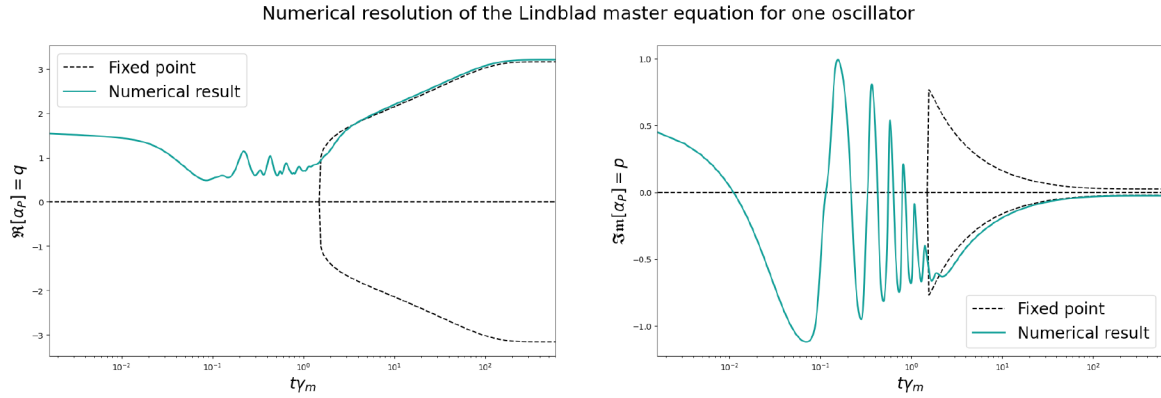


Figure 7: Numerical resolution of the Lindblad equation with $N = 30$, $\eta_f = 1000\gamma_m$, $\Delta = 30\gamma_m$ and $\tau = 100/\gamma_m$. The density matrix has been projected over the positive position quadrature to avoid the cancellation of the expected value of the annihilation operator.

The figure shows excellent agreement between the simulation results and the mean-field approximation, as the trajectory after the bifurcation converges toward the solution predicted by the mean-field analysis. The discrepancy observed before the bifurcation arise because the mean-field equations are derived by approximating the expectation value of a with the coherent amplitude. In contrast, the result presented here correspond to the normalized expectation value of MaM .

On the other hand, it is important to recall the conditions under which the mean-field approximation is derived ($a \approx \alpha$ and $|\alpha| \rightarrow \infty$). These conditions are illustrated in the following figures:

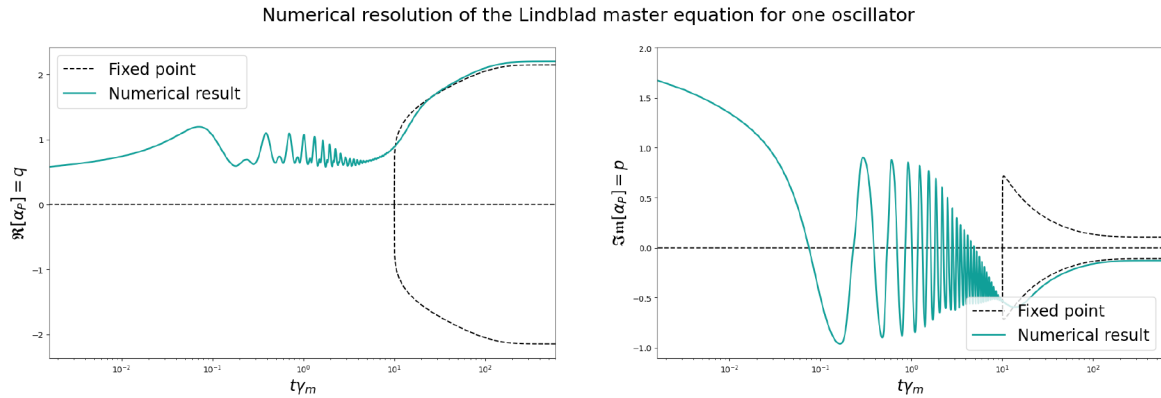


Figure 8: Numerical resolution of the Lindblad equation with $N = 30$, $\eta_f = 100\gamma_m$, $\Delta = 20\gamma_m$ and $\tau = 100/\gamma_m$

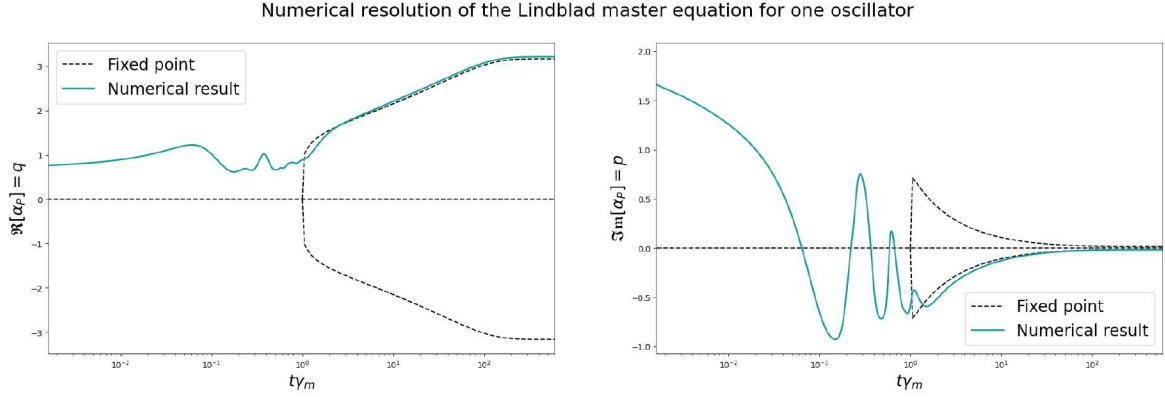


Figure 9: Numerical resolution of the Lindblad equation with $N = 30$, $\eta_f = 1000\gamma_m$, $\Delta = 20\gamma_m$ and $\tau = 100/\gamma_m$

As is shown in the pictures, when the $\eta_f = 1000\gamma_m$ the results approach the curve predicted by the mean-field approximation after the bifurcation more closely than in the case $\eta_f = 100\gamma_m$.

These results support the validity of the mean-field approximation for dissipative oscillators. As discussed in 4.2.1, its accuracy improves as $\frac{\eta}{\gamma_m} \rightarrow \infty$. However, the simulation results do not exhibit total convergence to the numerical curves of the theoretical fixed points. This discrepancy arises because the mean-field approximation neglects the effect of squeezing on the cat states, whereas the numerical solution incorporates it.

4.2.2 Coupled dissipative oscillators

In this section, the oscillators are going to be coupled using the same interaction term as in [1], and the mean-field approximation is derived to study the effects of the coupling on the dynamics. The mean-field analysis focuses on the case of two coupled oscillators, for which a general analytical solution exists. Additionally, the situation with N_o oscillators is considered, with some constraints imposed on the couplings to obtain an analytical result. Following the same procedure as for a single oscillator, the validity of the mean-field is checked using 79 as driving strength. However, since the Hilbert space dimension is larger in this case, the equations are solved using quantum jump trajectories [35, 46, 57, 58]. Finally, the potential application of this oscillator for quantum adiabatic computation, as in [1], is discussed depending on the preceding results.

The discussion in 4.2.1 suggest the possibility of using this oscillator to perform quantum adiabatic computation for solving combinatorial problems, as in [1]. The main idea is to employ cat-state generation, starting from the ground state of H_2 with $\eta = 0$, and generate cat states by passing through the bifurcation. If the process is carried out adiabatically, the system will remain in the ground state. Consequently, beyond and sufficiently far from the bifurcation, the coefficients of the cat states can be measured, corresponding to the solution of the desired problem. To achieve this, the following interaction term between the oscillators is introduced to solve Ising-like problems:

$$H_2 = \sum_{i=1}^{N_o} \Delta_i a_i^\dagger a_i - i\eta \left(a_i^2 - (a_i^\dagger)^2 \right) - \frac{\xi_0}{2} \sum_{i,j=1}^{N_o} J_{i,j} (a_i a_j^\dagger + a_j a_i^\dagger) + \xi_0 \sigma(t) \sum_{i=1}^{N_o} h_i (a_i + a_i^\dagger) \quad (92)$$

Here, the parameter ξ_0 represents a coupling constant with units of energy, and $\sigma(t)$ is a time-dependent coupling coefficient. Moreover, $J_{i,j} = J_{j,i}$ denotes the weight matrix describing the interactions between oscillators, while $\{h_i\}_{i=1}^{N_o}$ corresponds with an external field.

First, the effect of the coupling on the dynamic has been studied in the case of $\vec{h} = 0$ in E for two coupled oscillators. The results of the mean-field approximation show that there are again two phases. In the first phase, the only fixed-point solution is the trivial one $\alpha_i = 0$, where i denotes the oscillator index. In the second phase, the system undergoes another bifurcation when $\left| \frac{\xi_0}{4\eta} - \frac{\Delta}{2\eta} \right| = 1$, which leads to the generation of cat states. This indicates that the coupling shifts the bifurcation point, causing cat-state generation to occur earlier than in the single-oscillator case, since $\Delta, \xi_0 > 0$. Beyond the bifurcation, two possible solutions can be found depending on value of the coupling

$J_{i,j}$ between oscillators. If the coupling is positive, the coherent phase for both oscillators is given by:

$$\alpha_i = \pm \left(\frac{\eta}{\gamma_m} \right)^{1/6} \left[1 - \left(\frac{\xi_0}{4\eta} - \frac{\Delta}{2\eta} \right)^2 \right]^{1/12} \left\{ \cos \left[\frac{1}{2} \arctan \left(\frac{\frac{\xi_0}{4\eta} - \frac{\Delta}{2\eta}}{\sqrt{1 - \left(\frac{\xi_0}{4\eta} - \frac{\Delta}{2\eta} \right)^2}} \right) \right] - i \sin \left[\frac{1}{2} \arctan \left(\frac{\frac{\xi_0}{4\eta} - \frac{\Delta}{2\eta}}{\sqrt{1 - \left(\frac{\xi_0}{4\eta} - \frac{\Delta}{2\eta} \right)^2}} \right) \right] \right\} \quad (93)$$

The validity of the mean-field approximation was verified by solving the Lindblad master equation, as in the single-oscillator case. The resulting solution is:

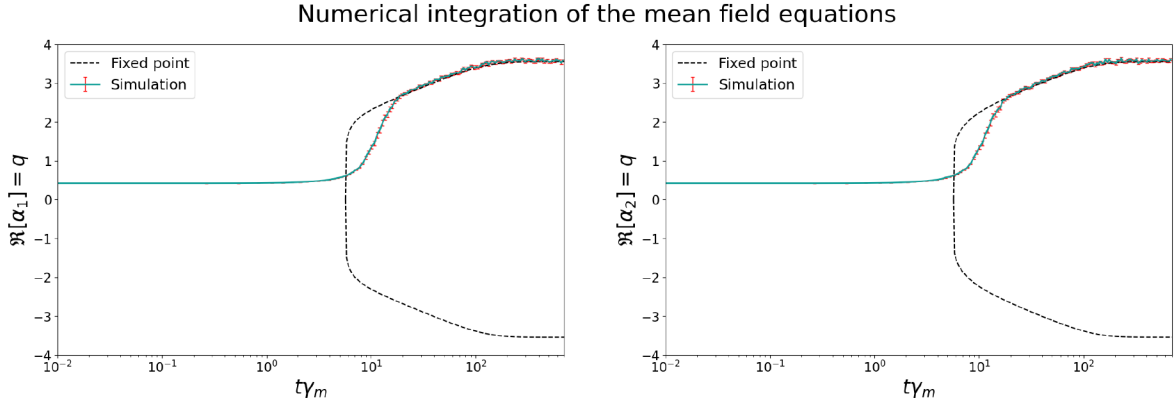


Figure 10: Numerical solution of the Lindblad equation for two oscillators was performed using the quantum jump method with $N = 30$, $\eta_f = 2000\gamma_m$, $\xi_0 = 150\gamma_m$, $\Delta = 300\gamma_m$, $\tau = 100/\gamma_m$ and 100 trajectories.

The simulation result corresponds to the expectation value of the annihilation operator over the quantum state, projected onto the positive region of the Wigner function. These results demonstrate that the simulation results converges closely to the values obtained from the mean-field approximation.

The solution for N_o coupled oscillators has also been computed in E under the constraint $\sum_{k=1}^{N_o} J_{l,k} = \sum_{k=1}^{N_o} J_{n,k}$ for $\forall l, n$. As shown in E, an analytical solution can be obtained in that case, which corresponds to the phase amplitude 93 but with the coupling constant replaced by $\xi = \xi_0 \sum_{k=1}^{N_o} J_{l,k}$. Therefore, the dynamic will be equivalent to the case of two oscillators.

Furthermore, the presence of coupling breaks the \mathbb{Z}_2 symmetry of each individual oscillator. As a result, the system no longer exhibits a well-defined parity under a parity transformation applied to a single oscillator. However, the full set of oscillators retains a global \mathbb{Z}_2 symmetry under a simultaneous transformation of all oscillators:

$$Z = \otimes_{i=1}^{N_o} Z_2 \longrightarrow [H_{\text{Coupling}}, Z] = 0 \quad (94)$$

This is proved in F. Due to the existence of this symmetry, \mathcal{L} can be discomposed into 4^{N_o} blocks with 2^{N_o} steady states, as shown in [45], where N_o is the number of coupled oscillators. From the mean-field analysis, it is known that all oscillators have approximately the same coherence amplitude, and the final state must exhibit a well-defined global parity. Therefore, the steady states of the system with $h_i = 0$ are:

$$|CAT^\pm(\vec{s})\rangle = C_n \left(\otimes_{i=1}^{N_o} |s_i \alpha, \xi\rangle_i \pm \otimes_{i=1}^{N_o} |-s_i \alpha, \xi\rangle_i \right) \quad (95)$$

Here, the subindex i denotes the oscillator associated with that ket, ξ represents the squeezing parameter of the state and α corresponds to the coherent amplitude obtained from the mean-field analysis. The vector \vec{s} , with $s_i \in \{-1, 1\}$, specifies the sign of the coherent amplitude of each oscillator. Permutations and sign changes of the coefficients give rise to different steady states. These signs are quantities measured after the adiabatic evolution to obtain the solution of the problem.

On the other hand, when $\vec{h} \neq 0$, the \mathbb{Z}_2 symmetry is broken and the system no longer exhibits a symmetry. As a consequence, the final state does not possess a well-defined parity and reduces to the tensor product of the lobes:

$$|\psi_f(\vec{s}')\rangle = \otimes_{i=1}^{N_o} |s_i \alpha, \xi_i\rangle \quad (96)$$

The system undergoes a bifurcation leading to the generation of the cat states, and the state is measured sufficiently far from the bifurcation. At this stage, the driving strength is large enough that the harmonic oscillator term and the coupling term can be treated as perturbations. Consequently, the corrections introduced by the coupling can be computed using first-order perturbation theory:

$$E_{corr} = \sum_{k=1}^{N_o} \Delta_k (\eta/\gamma_m)^{1/3} + \xi_0 \left[-\left(\frac{\eta}{\gamma_m} \right)^{1/3} \sum_{k,j=1}^{N_o} J_{k,j} s_k s_j + 2\sigma(t) (\eta/\gamma_m)^{1/6} \sum_{i=1}^{N_o} h_i s_i \right] \quad (97)$$

The mean-field analysis in E shows that, in the regime of $\eta \gg \Delta, \xi_0$, the coherence phase can be approximated as $\alpha \approx \left(\frac{\eta}{\gamma_m} \right)^{1/6}$. This approximation is used to compute the first-order correction to the energy. As shown in 97, when $h_i = 0$, the correction to the ground-state energy of H_2 corresponds to the Ising energy:

$$E_{corr} = \sum_{k=1}^{N_o} \Delta_k (\eta/\gamma_m)^{1/3} - \xi_0 \left(\frac{\eta}{\gamma_m} \right)^{1/3} \sum_{k,j=1}^{N_o} J_{k,j} s_k s_j \quad (98)$$

However, if $h_i \neq 0$ and the coefficient $\sigma(t)$ is chosen such that, in the limit $\frac{\eta}{\gamma_m} \rightarrow \infty$, we have $\sigma(t) \rightarrow (\eta/\gamma_m)^{1/6}$, the corresponding energy correction becomes:

$$E_{corr} = \sum_{k=1}^{N_o} \Delta_k (\eta/\gamma_m)^{1/3} + 2(\eta/\gamma_m)^{1/3} \xi_0 \left[-\frac{1}{2} \sum_{k,j=1}^{N_o} J_{k,j} s_k s_j + \sum_{i=1}^{N_o} h_i s_i \right] \quad (99)$$

In this case, the energy correction corresponds to the Ising energy in the presence of an external field. From this analysis, the coefficient $\sigma(t)$ has been chosen as $\sigma(t) = (\eta(t)/\gamma_m)^{1/6}$, since it does not affect the energy level structure at $\eta = 0$. For large driving strengths, this choice is $\sigma(t) = (\eta_f/\gamma_m)^{1/6}$ also satisfied the requirement to reproduce the Ising energy in the presence of an external field. Therefore, if the initial state is the ground state of the Hamiltonian and η is increased adiabatically, the final state after the evolution will correspond to the solution of the Ising problem. In this section, the driving strength is incremented according to 79.

Therefore, the quantum computation scheme with this oscillator follows the same procedure discussed for the cat-state generation in 2.3.1. The system is initially prepared in the ground state of H_2 with driving strength $\eta = 0$, and all oscillators are coupled according to the scheme introduced in 92. This initial state has positive symmetry, so the cat state generated after the bifurcation will corresponds to an even cat state 95 if $h_i = 0$. Otherwise, for $h_i \neq 0$, the resulting state after the bifurcation is given by 96. The driving strength is then increased according to 79. If the nonlinear terms in the Hamiltonian are enhanced adiabatically, the set of oscillators remains in the ground state after the bifurcation. Once the system is sufficiently far from the bifurcation, the signs of the coherent amplitudes of the final state are measured. This produces a vector \vec{s} , where the measured coefficients s_i correspond to the vector that minimizes the energy in 98 if $h_i = 0$, or 99 if $h_i \neq 0$.

However, to apply this scheme for solving of Ising-like problems, the ground state at $\eta = 0$ must be the vacuum state $\otimes_{i=1}^{N_o} |0\rangle$, independently of the couplings coefficients. If this condition is not satisfied, transitions to lower-energy

states may occur during the adiabatic evolution. To ensure this condition, the detuning Δ_i of each oscillator is chosen such that the Hamiltonian at $\eta = 0$ is a positive semidefinite matrix:

$$\langle H \rangle_\psi \geq 0 \quad (100)$$

There is no a unique choice of $\{\Delta_i\}_{i=1}^{N_o}$ that satisfies this condition, as noted in [1]. However, for the simulations presented in this study, the following choice is adopted:

$$\Delta_i = \Delta = \xi_0 N_o \quad (101)$$

Here, N_o denotes the number of couples oscillators. This choice ensures that the Hamiltonian is positive semidefinite matrix.

Finally, the energy levels are verified in the presence of a coupling to ensure that no level mixing occurs.

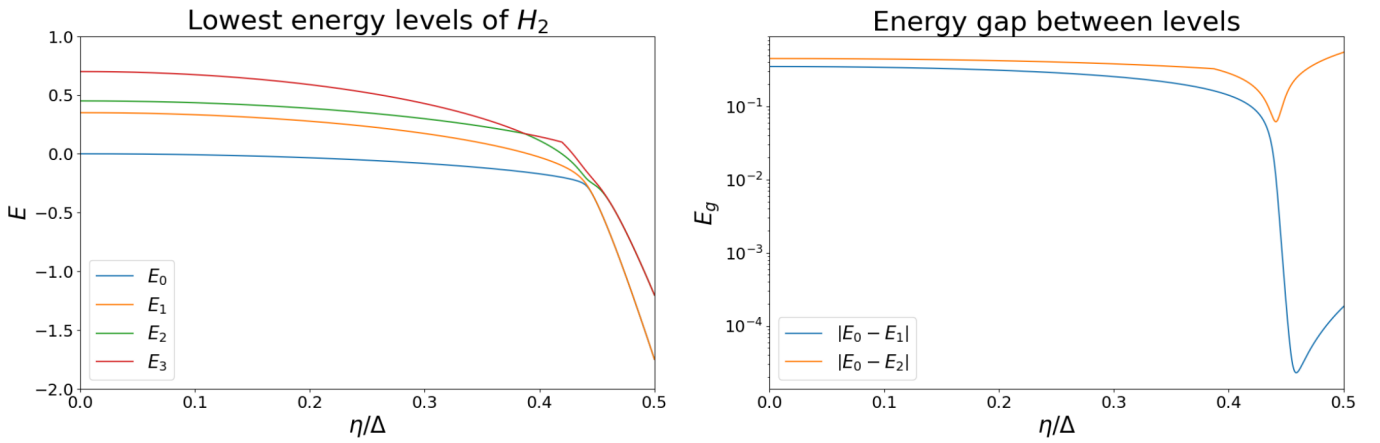


Figure 11: Lowest energy levels of two coupled oscillators with $h_i = 0$ oscillator as a function of the parameter $\frac{\eta_f}{\Delta} = 0.5$ and $\frac{\xi_0}{\Delta} = 0.125$.

The results are very similar to those obtained for a single oscillator, where the closest energy levels belong to different parity sectors, and after the bifurcation, all states become well separated again.

These results show that the presence of an interaction term affects to the cat-state generation. Specifically, the mean-field approximation for the fixed point after the bifurcation reveals that the functional form of the equation remains the same, with the substitution $\frac{\Delta}{2\eta} \rightarrow \frac{\xi_0}{4\eta} - \frac{\Delta}{2\eta}$. Moreover, the presence of the coupling enables control over the bifurcation point by choosing ξ_0 such that $\frac{\Delta}{2\eta} \rightarrow \frac{\xi_0}{4\eta} - \frac{\Delta}{2\eta} = 1$ for a desired value of η_f . These results may offer advantages for experimental implementations, as they allow the cat-state generation at lower driving strengths.

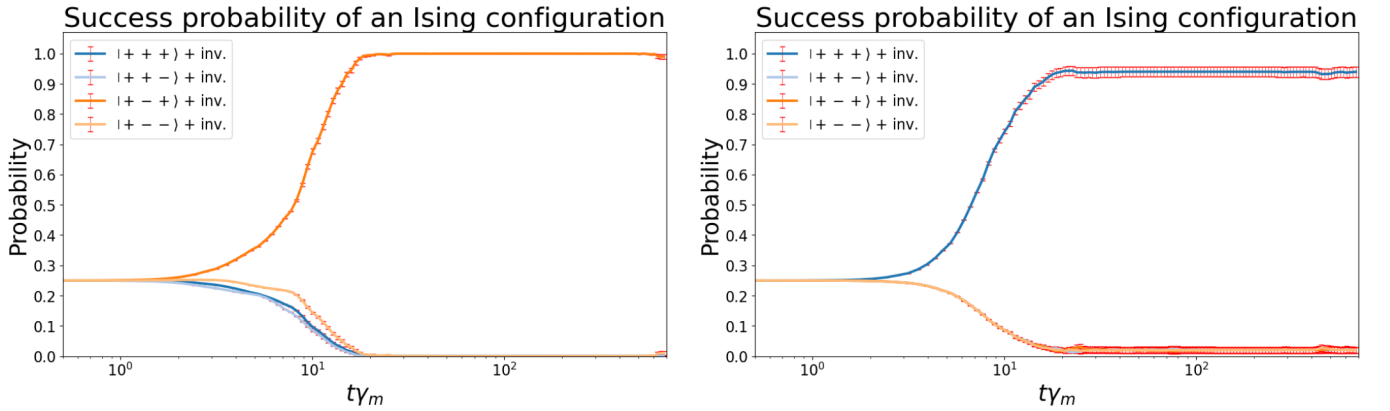
Furthermore, the symmetry of the coupled dissipative oscillators has been shown to be beneficial for quantum computation, as it prevents the possible appearance of a closed gap during the computational process. This result holds for both KPO and dissipative oscillators, and it provides an advantage over qubit-based quantum computers that lack such symmetry [48, 59]. In fact, as discussed in [1], since the first excited state corresponds to the odd cat state, if an error during the computation causes a transition from the ground state to the first excited state, the measured outcome would still be correct because the lobe amplitude are identical.

4.2.3 Results of the Ising model

In this section, the Ising model, both with and without an external field, is solved using the dissipative oscillators described in [2]. As in the case of the KPO oscillator, the oscillators are coupled according to [1]. The system is initialized in the vacuum state $|0\rangle$ with $\eta(0) = 0$, and the driving strength is then increased according to 79 to amplify

the non linear terms. The parameter $\eta(t)$ is increased until the system undergoes the bifurcation, where the cat states are generated 2.3, corresponding to the regime where the system solves the Ising model. The time-dependent Lindblad equation is solved using the quantum trajectories method with a cutoff of $N = 30$. The success probabilities of all the possible configurations \vec{s} are then calculated using the PVM introduced in 3.1 and are represented as a function of $t\gamma_m$ to track the system's evolution. As in the case of KPO oscillators, these results indicate whether the system of oscillators converges to a configuration that solves the Ising model or not. If it does, the success probability of the ground state will be maximized, while the probabilities of the others states will tend to zero.

The obtained results are:

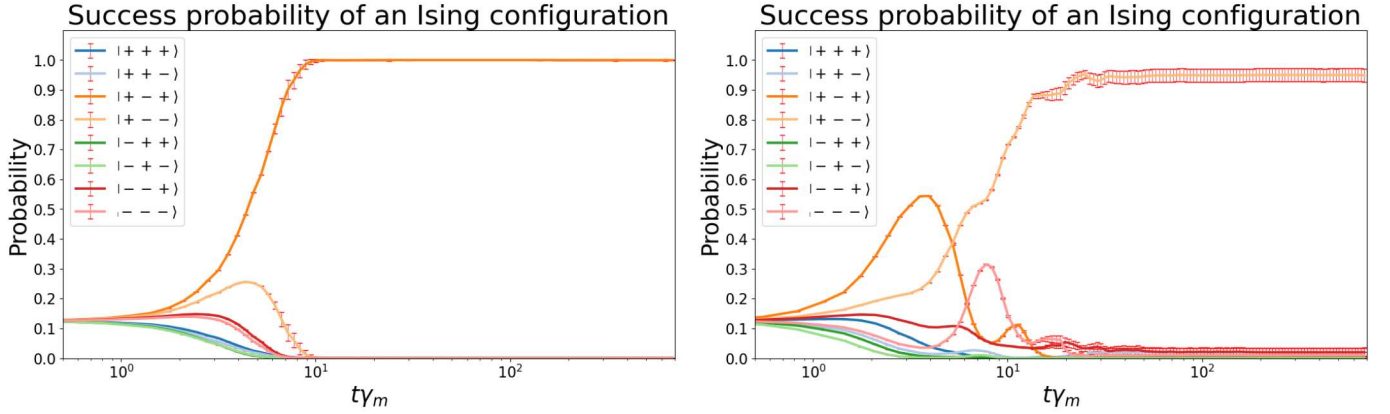


Success probability of each configuration as a function of $t\gamma_m$ for 3 coupled oscillators. The simulation parameters are $\tau = 300/\gamma_m$, $\eta(0) = 0$, $\eta(700/K) = 2000\gamma_m$, $\xi_0 = 200\gamma_m$, $\Delta = 600\gamma_m$, and a cutoff of $N = 30$. The coupling constants between the oscillators are $J_{i,i} = 0$, $J_{1,0} = J_{0,1} = -1.4$, $J_{1,2} = J_{2,1} = -0.3$ and $J_{0,2} = J_{2,0} = 0.8$. For this coupling the configuration the lowest-energy states correspond to $\vec{s} = (1, -1, 1)$ and $-\vec{s}$.

Success probability of each configuration as a function of $t\gamma_m$ for 3 coupled oscillators. The simulation parameters are $\tau = 300/\gamma_m$, $\eta(0) = 0$, $\eta(700/K) = 2000\gamma_m$, $\xi_0 = 200\gamma_m$, $\Delta = 600\gamma_m$ and a cutoff of $N = 30$. The coupling constants between the oscillators are $J_{i,j} = 1 - \delta_{i,j}$. For this coupling the configuration, the lowest-energy states correspond to $\vec{s} = (1, 1, 1)$ and $-\vec{s}$.

Table 6: Success probability of each configuration of the Ising model for 3 coupled oscillators with different coupling constants. These results are obtained in the case where the Ising model is not subject to an external field, $\vec{h} = 0$. The results demonstrate that the model is able to solve the Ising problem, since configurations with maximum probability correspond to the Ising ground-state solution.

The simulations show that the systems is able to solve the Ising model in the absence of an external field. In both figures, the success probability of the lowest-energy configuration is maximized.



Success probability of each configuration as a function of $t\gamma_m$ for 3 coupled oscillators. The simulation parameters are $\tau = 300/\gamma_m$, $\eta(0) = 0$, $\eta(700/K) = 2000\gamma_m$, $\xi_0 = 200\gamma_m$, $\Delta = 600\gamma_m$ and a cutoff of $N = 30$. The coupling constants between the oscillators are $J_{ii} = 0$, $J_{1,0} = J_{0,1} = -1.4$, $J_{1,2} = J_{2,1} = -0.3$ and $J_{0,2} = J_{2,0} = 0.8$. For this coupling, the configuration with the lowest energy corresponds to $\vec{s} = (1, -1, 1)$ in the presence of an external field of $\vec{h} = (-2.2, 3.1, -1.1)$.

Success probability of each configuration as a function of $t\gamma_m$ for 3 coupled oscillators. The simulation parameters are $\tau = 300/\gamma_m$, $\eta(0) = 0$, $\eta(700/K) = 2000\gamma_m$, $\xi_0 = 200\gamma_m$, $\Delta = 600\gamma_m$ and a cutoff of $N = 30$. The coupling constants between the oscillators are $J_{ii} = 0$, $J_{1,0} = J_{0,1} = 0.8$, $J_{1,2} = J_{2,1} = -0.9$ and $J_{0,2} = J_{2,0} = 0.7$. For this coupling, the configuration with the lowest energy corresponds to $\vec{s} = (1, -1, -1)$ and in the presence of an external field of $\vec{h} = (-2.2, 3.1, -1.1)$.

Table 7: Success probability of each configuration of the Ising model for 3 coupled oscillators with different coupling constants. These results are obtained in the case where the Ising model is subject to an external field $\vec{h} \neq 0$. The coupling coefficient used in the simulations is $\sigma(t) = \left(\frac{\eta(t)}{\gamma_m}\right)^{1/6}$.

As in the previous case, the probability reaches a maximum for the configuration that minimizes the Ising energy, but now with an external field applied.

These results show that the dissipative oscillator can solve the Ising model both with and without an external field. In all cases, the oscillator system produces a solution with a success probability greater than 0.9. Therefore, dissipative oscillators can be considered capable of performing quantum computation, comparable to KPO oscillators.

Nevertheless, all simulations performed with KPO oscillators indicate that the success probability of the obtained configurations is higher than in the case of dissipative oscillators. However, it should be noted that the KPO simulations presented here were conducted in a closed system that does not account for dissipation. When dissipation is included in the KPO simulations, as in [24], the success probability of solving the Ising model decreases by several tenths.

4.3 Applications

Now, both oscillators are applied to solve the Hopfield network and for the determination of eigenvectors.

4.3.1 Hopfield model

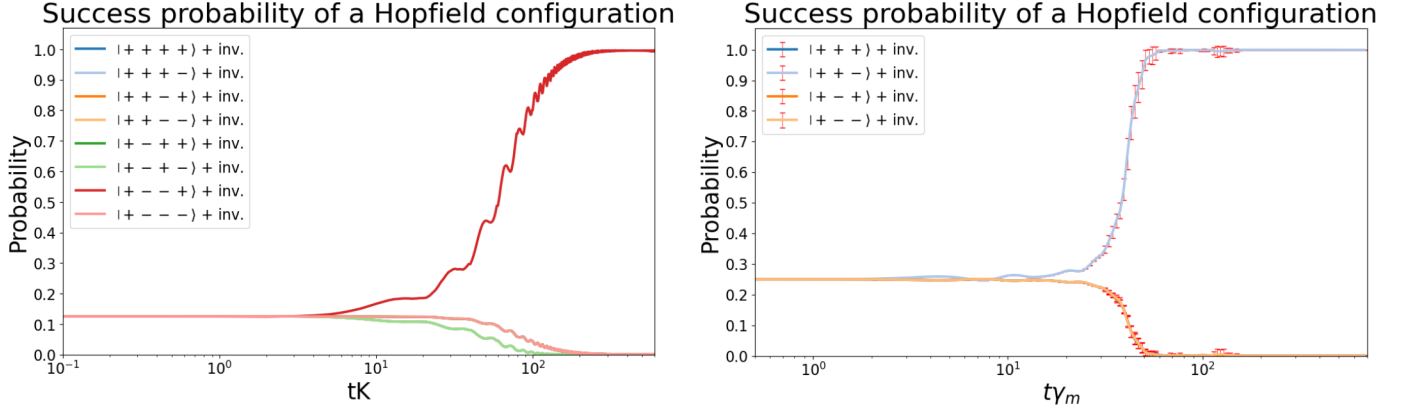
Now, both oscillators are employed to solve the Hopfield model [55]. As explained in A, the coupling coefficients between the oscillators are chosen according to 115 to store a pattern. Meanwhile, the rest of the model remains the same as in the case of the Ising model.

The problem is studied with four oscillators for the KPO case and three for the dissipative oscillators due to the computational resources J. The same procedure used to solve the Ising model in 4.1.2, 4.2.3 for both types of oscillators is followed here. Consequently, the success probability of each possible memory configuration is computed

to evaluate the systems' ability to retrieve stored memories.

Since the Hopfield model can store multiple memories, we also investigate the effect of ground-state degeneracy on the success probability by encoding more than one memory in the system. This is accomplished by modifying the couplings of the model according to A. The subsequent steps follow the same procedure as in the case of the Ising model and the network with a single stored pattern.

The obtained results are:



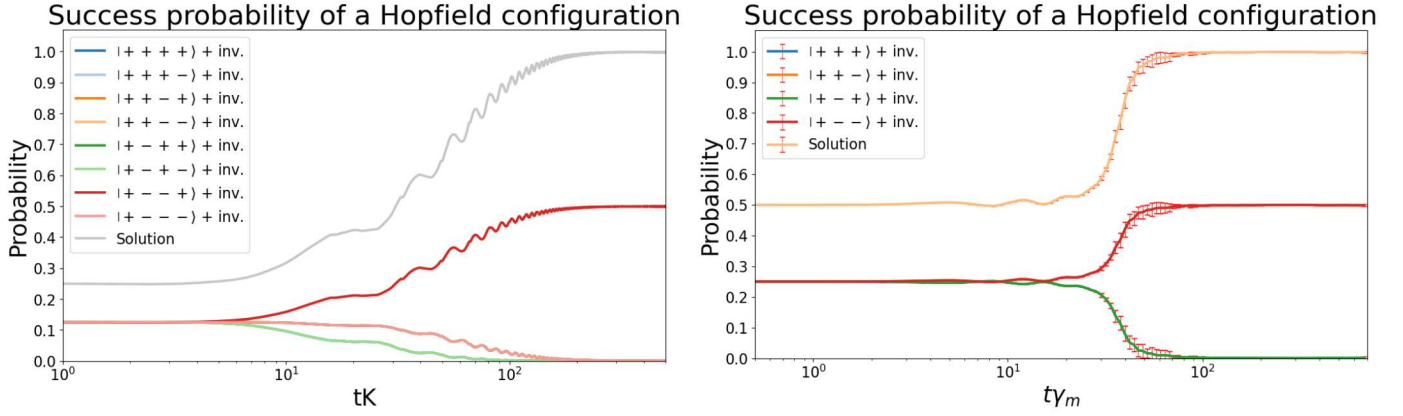
Success probability of each configuration as a function of tK for 4 coupled oscillators. The simulation parameters are $p(0) = 0$, $p(1000/K) = 6K$, $\xi = 0.5K$ and $N = 14$. The stored pattern in the system is $(1, -1, -1, 1)$.

Success probability of each configuration as a function of $t\gamma_m$ for 3 coupled oscillators. The simulation parameters are $\tau = 300.0/\gamma_m$, $\eta(0) = 0$, $\eta(700/K) = 2000\gamma_m$, $\xi = 200\gamma_m$, $\Delta = 600\gamma_m$ and a cutoff of $N = 30$. The pattern stored in the system is $\vec{s} = (1, 1, -1)$.

Table 8: The left plot shows the success probability of each configuration as function of tK for KPO oscillators. Meanwhile, the right plot shows the success probability of each configuration as a function of $t\gamma_m$ for dissipative oscillators. The couplings for the simulation correspond to those of the Hopfield model 115

In this situation, the coupling correspond to the Hopfield model. Thus, the coupling values can now be either -1 or 1 , allowing to the ground state of the model to correspond to a store pattern. As shown in the picture, even though the couplings have been changed, the system is still able to converge to the ground state of the model. The fact that the number of curves observed are less than 2^{N_o} is because in the Hopfield model a patter ξ^μ and its anti-pattern $-\xi^\mu$ have the same energy. In fact, for the case of 3 oscillators the system presents only two energy levels one associated for the ground state (stored pattern) and the second for all the remaining states. Meanwhile, in the case of 4 coupled oscillators there are 3 energy levels. Moreover, when the KPO reach the solution for the Hopfield model, the success probability does not settle to a plateau like in the case of dissipative oscillators because there are still some oscillators at that regime.

In the situation where there is more than one pattern stored in the network the success probability:



Success probability of each configuration as a function of tK for 4 coupled oscillators. The simulation parameters are $p(0) = 0$, $p(1000/K) = 6K$, $\xi = 0.5K$ and $N = 14$. The patterns stored in the system are $(1, -1, -1, 1)$ and $(1, 1, -1, -1)$.

Success probability of each configuration as a function of $t\gamma_m$ for 3 coupled oscillators. The simulation parameters are $\tau = 300.0/\gamma_m$, $\eta(0) = 0$, $\eta(700/K) = 2000\gamma_m$, $\xi = 200\gamma_m$, $\Delta = 600\gamma_m$ and a cutoff of $N = 30$. The patterns stored in the system are $(1, 1, -1)$ and $(1, -1, -1)$.

Table 9: The left plot shows the success probability of each configuration as function of tK for KPO oscillators. Meanwhile, the right plot shows the success probability of each configuration as function of $t\gamma_m$ for dissipative oscillators. The couplings for the simulation correspond to those of the Hopfield model 115. The curve labelled *solution* shows that the summation of the success probability of measure any of the ground states.

The success probability observed for both oscillators are identical (neglecting the squeezing for the dissipative oscillators); in each case, the oscillator system successfully retrieves the stored memories. After the bifurcation, since the ground state is degenerate, the system converges to a linear combination of all the ground states, resulting in the final state:

$$|\psi_f\rangle \approx \frac{1}{2P} \sum_{n=1}^P \left(\otimes_{i=1}^{N_o} |s_{n,i}\alpha_i\rangle + \otimes_{i=1}^{N_o} |-s_{n,i}\alpha_i\rangle \right) \quad (102)$$

As a consequence, the probability of independently measuring each ground state decreases, while the probability of measuring a ground state approaches 1.

The results obtained in 4.3.1 show that the oscillator network is capable of solving the Hopfield model. Moreover, these results demonstrate the ability of oscillator systems to address problems with degenerate ground states. Specifically, the model is able to identify all the solutions of the network without collapsing into a single configuration, resulting in a state that represents an equal-weight superposition of all solutions. This result makes it possible to obtain all the ground states of the problem simply by measuring the final state. Although the Hopfield model is relatively simple, it has a wide range of applications in combinatorial optimization, such as the Travelling Salesman Problem [8, 60, 61], medical image segmentation [62], the maximum clique problem [63], and harmonic current estimation [64]. Moreover, the development of Modern Hopfield Neural networks [65] is based on the classical discrete Hopfield model [55]. Therefore, these results may open a way for future applications in more complex models within the field of deep learning.

4.3.2 Eigenvector problem

Finally, the KPO oscillator [1] and the dissipative oscillator [2] are employed to solve the eigenvector problem. Specifically, given a real symmetric matrix \mathbf{M} and a known eigenvalue λ , the objective is to determine the eigenvector of \mathbf{M} corresponding to λ . To this end, the following couplings are incorporated into the Hamiltonian of each oscillator:

- Constant term:

$$H^{1)} = \sum_{i,j,p=1}^d \sum_{k,l=1}^q 2^{2r-k-l-2} M_{i,p} M_{i,p}^\dagger - \lambda \sum_{i,j=1}^d \sum_{k,l=1}^q 2^{2r-k-l-2} M_{i,j}^\dagger - \lambda \sum_{i,j=1}^d \sum_{k,l=1}^q 2^{2r-k-l-2} M_{i,j} + \lambda^2 \sum_{i=1}^d \sum_{k,l=1}^q 2^{2r-k-l-2} \quad (103)$$

- Non-interacting term:

$$\begin{aligned} H^{2)} = & \sum_{i,j,p=1}^d \sum_{k,l=1}^q 2^{2r-k-l-2} M_{i,p} M_{i,p}^\dagger (a_{i,k} + a_{i,k}^\dagger + a_{j,k} + a_{j,k}^\dagger) + \\ & - \lambda \sum_{i,j=1}^d \sum_{k,l=1}^q 2^{2r-k-l-2} M_{i,j}^\dagger (a_{i,k} + a_{i,k}^\dagger + a_{j,k} + a_{j,k}^\dagger) - \lambda \sum_{i,j=1}^d \sum_{k,l=1}^q 2^{2r-k-l-2} M_{i,j} (a_{i,k} + a_{i,k}^\dagger + a_{j,k} + a_{j,k}^\dagger) + \\ & + \lambda^2 \sum_{i=1}^d \sum_{k,l=1}^q 2^{2r-k-l-2} (a_{i,k} + a_{i,k}^\dagger) \end{aligned} \quad (104)$$

- Interacting term:

$$\begin{aligned} H^{3)} = & \sum_{i,j,p=1}^d \sum_{k,l=1}^q 2^{2r-k-l-2} M_{i,p} M_{i,p}^\dagger (a_{i,k} + a_{i,k}^\dagger) (a_{j,l} + a_{j,l}^\dagger) + \\ & - \lambda \sum_{i,j=1}^d \sum_{k,l=1}^q 2^{2r-k-l-2} M_{i,j}^\dagger (a_{i,k} + a_{i,k}^\dagger) (a_{j,l} + a_{j,l}^\dagger) - \lambda \sum_{i,j=1}^d \sum_{k,l=1}^q 2^{2r-k-l-2} M_{i,j} (a_{i,k} + a_{i,k}^\dagger) (a_{j,l} + a_{j,l}^\dagger) + \\ & + \lambda^2 \sum_{i=1}^d \sum_{k,l=1}^q 2^{2r-k-l-2} (a_{i,k} + a_{i,k}^\dagger) (a_{i,l} + a_{i,l}^\dagger) \end{aligned} \quad (105)$$

With their corresponding coupling constants for each oscillator. Here, $M_{i,j}$ denotes the matrix from which the eigenvector is to be computed, and λ is the eigenvalue associated with that eigenvector. The constant term can be disregarded in practice, as it uniformly shifts all energy levels. However, it is retained here because it provides a better interpretability of the corrections introduced to the energy levels **I**. The reason behind the choice of these interaction Hamiltonians is discussed in **I**. The coupling coefficients for each oscillator, as described in **I**, are given by:

- KPO:

$$\begin{aligned} \alpha(t) &= \frac{p(t) - \Delta \tanh(p(t)/\Delta)}{K} \\ \beta(t) &= \frac{1}{2} \sqrt{\frac{p(t) - \Delta \tanh(p(t)/\Delta)}{K}} \\ \gamma(t) &= \frac{1}{4} \end{aligned} \quad (106)$$

- Dissipative oscillators:

$$\begin{aligned} \alpha(t) &= \left(\frac{\eta(t)}{\gamma_m} \right)^{1/3} \\ \beta(t) &= \frac{1}{2} \left(\frac{\eta(t)}{\gamma_m} \right)^{1/6} \\ \gamma(t) &= \frac{1}{4} \end{aligned} \quad (107)$$

These coefficients are chosen to ensure that the corrections that they introduce to the ground-state energy, enable the solution of the eigenvector problem.

To investigate this problem, the two oscillators were employed using these couplings to evaluate their performance in a more complex situation than previously considered. Simulations of both oscillators with these coupling coefficients were performed to solve the problem. For the KPO oscillator system, the Adams method [56] was used with 4 coupled oscillators. In contrast, the simulations of the dissipative oscillators were carried out using the quantum jump approach [58] with 2 coupled oscillators and for 100 trajectories.

The algorithm to solve the problem proceeds as follows. Consider a real symmetric matrix $M_{i,j} = M_{j,i}$ and one of its eigenvalues λ . Following a procedure analogous to that used for the Ising model, the system is initialized in the ground state of the Hamiltonian with the interaction term defined previously. The driving strength of the Hamiltonian is then gradually increased until the system undergoes a bifurcation, generating cat states and thereby solving the eigenvector problem.

After the simulation, the final state is measured to obtain the result. The measurement yields a vector $\vec{s} = \{s_i\}$, corresponding to the final state $\otimes_{i=1}^{N_o} |s_i f(t_f)\rangle$, analogous to the case of the Ising model. This solution can be mapped to the coefficients of the eigenvector \vec{x} being computed. Each eigenvector coefficient x_i is represented in a binary form using q bits \mathbf{I} :

$$x_i = \sum_{j=1}^q 2^{r-j-1} b_{i,j} \quad (108)$$

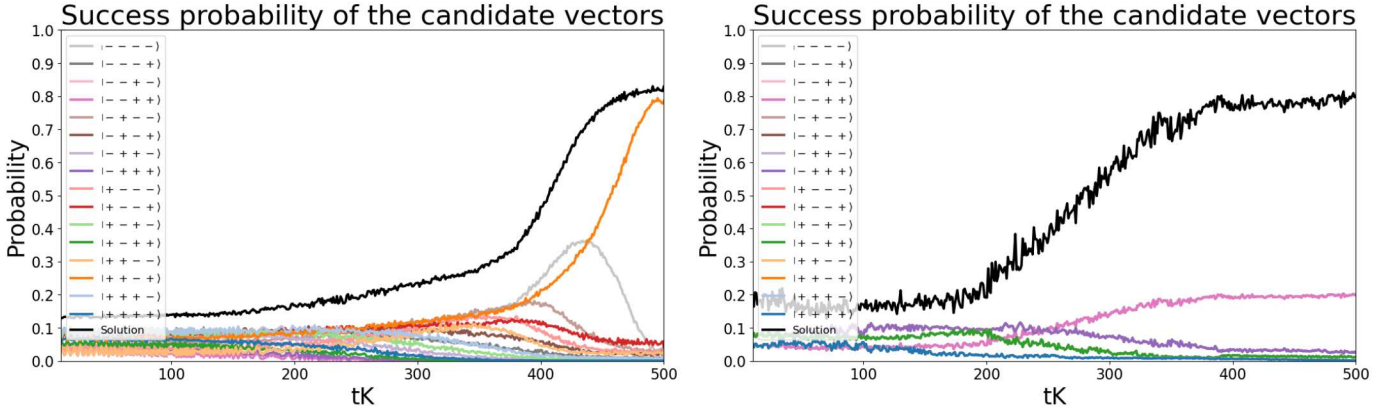
Here, r denotes the number of bits used to represent the real part of a coefficient, and $b_{i,j}$ represents j -th bit associated to the i -th coefficient. The simulation yields values $s_i \in \{-1, 1\}$. By mapping a bit value of 0 to -1 , an analogy can be drawn between the binary representation of the coefficients and the results. In this mapping, the first q elements of the measured vector \vec{s} correspond to the first coefficient, the elements with $q < i < 2q$ corresponds to the second coefficient, and so on.

For example, if the outcome of the computation is $|+ - - +\rangle$, the associated eigenvector is:

$$|+ - - +\rangle \rightarrow \begin{cases} (+-) \rightarrow x_1 = 2 \\ (-+) \rightarrow x_2 = 1 \end{cases} \rightarrow \vec{x} = (2, 1) \quad (109)$$

To evaluate the performance of these models in solving the eigenvector problem, the success probability of the solutions is computed as a function of time for different matrices $M_{i,j}$ as well as with the Ising model. Additionally, a histogram of the success probability is generated to analyse the frequency of successfully obtaining the correct eigenvector. To construct this histogram, 1000 simulations were performed for each oscillator using random matrices as input. The success probability is calculated as the sum of all the configurations that yield equivalents eigenvectors.

The results obtained for the eigenvector determination using KPO oscillators are as follows:



Success probability of each eigenvector candidate as a function of Kt for four coupled oscillators. The simulation parameters are $p(0) = 0$, $p(700/K) = 5K$, $\Delta = 2K$, $\xi_0 = 0.5K$, with a cutoff for the Hilbert space of $N = 14$. The given matrix elements are $M_{1,1} = 2.731$, $M_{1,2} = M_{2,1} = -2.364$ and $M_{2,2} = 9.037$, whose eigenvector corresponding to the larger eigenvalue is $\vec{v} = \frac{1}{\sqrt{10}} (3, 1)$. Consequently, the configurations associated with vectors proportional to this eigenvector is $|++--\rangle$.

Success probability of each eigenvector candidate as a function of Kt for four coupled oscillators. The simulation parameters are $p(0) = 0$, $p(700/K) = 5K$, $\Delta = 2K$, $\xi_0 = 0.5K$, with a cutoff for the Hilbert space of $N = 14$. The given matrix elements are $M_{1,1} = 15.756$, $M_{1,2} = M_{2,1} = 0.0$ and $M_{2,2} = 0.309$, whose eigenvector corresponding to the larger eigenvalue is $\vec{v} = (0, 1)$. Consequently, the configurations associated with vectors proportional to this eigenvector are $|--++\rangle$, $|--+-\rangle$ and $|---+\rangle$.

Table 10: Success probability of each eigenvector candidate for different input matrices. The figure shows that, in both cases, the model maximizes the probability the probability of the configurations that solve the equation $(\mathbf{M} - \lambda \mathbf{I}) \vec{x} = 0$. The curve labelled *solution* corresponds to the sum of the success probabilities of all configurations that satisfy this equation, demonstrating that the model correctly solve the problem.

Both figures show that the system of KPO oscillators maximizes the probability of configurations that solve the equation $(\mathbf{M} - \lambda \mathbf{I}) \vec{x} = 0$. In the left figure, it corresponds to the state $|++--\rangle$. In the right figure, it corresponds to the states $|--++\rangle$, $|--+-\rangle$ and $|---+\rangle$, as all these configurations are proportional to the eigenvector $\vec{v} = (0, 1)$.

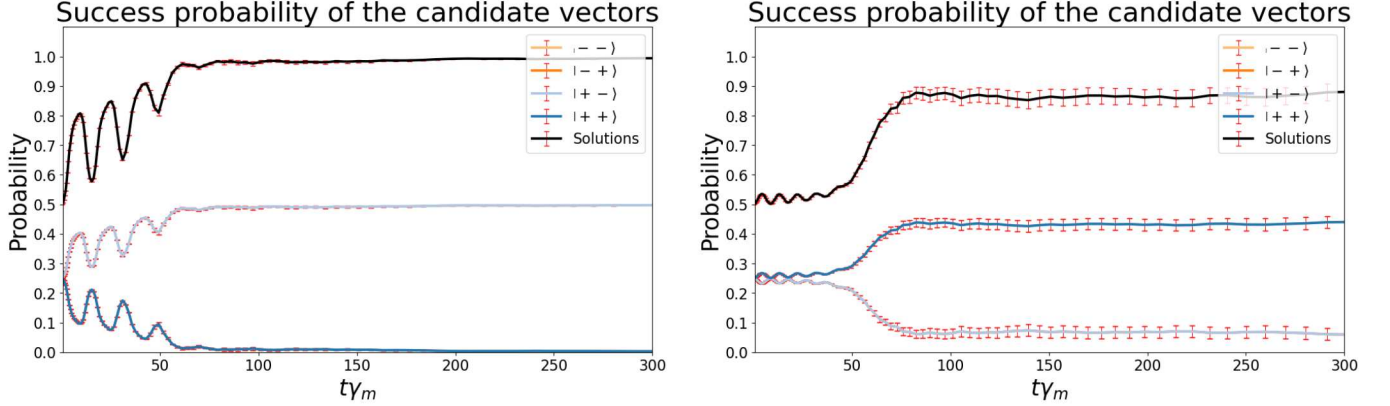
However, as can be seen in both figures, the success probability of obtaining a solution of the system $(\mathbf{M} - \lambda \mathbf{I}) \vec{x} = 0$, is greater than the sum of the probabilities of the aforementioned states. This happens because the state $|---\rangle$, which corresponds to the null vector $\vec{0}$, is always a solution regardless of the values of \mathbf{M} and λ . Therefore, the curve labelled *solution* (black line), which also accounts for probability $\vec{0}$ as valid solution, exhibits a higher success probability of measuring a solution to the system of equations.

The system does not converge to the non-vanishing configuration because both the null vector and the non-vanishing solution produce the same correction to the ground-state energy, resulting in degeneracy. Additionally, the presence of the terms such as a_i breaks the parity symmetry, so the final state forms a linear combination of all the states that satisfy the eigenvector equation:

$$|\psi_f\rangle = \sum_{\vec{s}_{\text{sol}}} c_i \left(\otimes_{j=1}^{N_o} |s_j f(t)\rangle \right) \quad (110)$$

where c_i are the normalized coefficients of each state, and the summation runs over all states \vec{s} that correspond to vectors \vec{x} solving the system.

In the case of dissipative oscillators:



The given matrix elements are $M_{1,1} = 0.299$, $M_{1,2} = M_{2,1} = 0.0$ and $M_{2,2} = 2.474$. Its eigenvector corresponding to the lowest eigenvalue is $\vec{v} = (0, 1)$. Therefore, the configurations associated with a vector proportional to this eigenvector is $|-\rangle$.

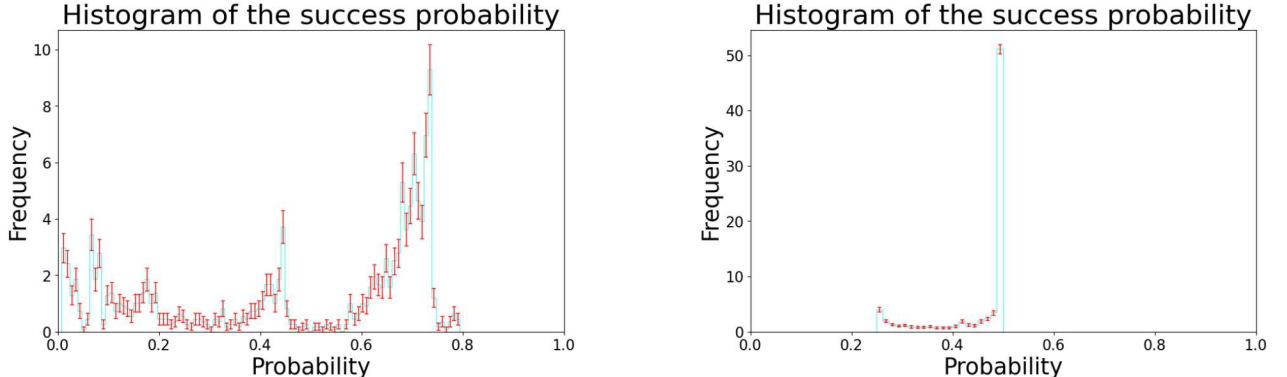
The given matrix elements are $M_{1,1} = 0.886$, $M_{1,2} = M_{2,1} = -0.686$ and $M_{2,2} = 0.886$. Its eigenvector corresponding to the lowest eigenvalue is $\vec{v} = \frac{1}{\sqrt{2}}(1, 1)$. Therefore, the configurations associated with a vector proportional to this eigenvector is $|+\rangle$.

Table 11: Success probability of each configuration as a function of $t\gamma_m$ for two coupled oscillators. The simulation parameters are $\tau = 300/\gamma_m$, $\eta(0) = 0$, $\eta(1000/\gamma_m) = 2000\gamma_m$, $\xi_0 = 300\gamma_m$, $\Delta = 600\gamma_m$, with a cutoff of $N = 30$. The figure shows that, in both cases, the dissipative oscillators successfully solve the eigenvalue equation. The curve labelled *solution* (black line) represents the sum of the success probabilities of all configurations that satisfy $(\mathbf{M} - \lambda\mathbf{I}) \vec{x} = 0$. These results were obtained by solving the Lindblad master equation using the quantum jump method with 100 trajectories.

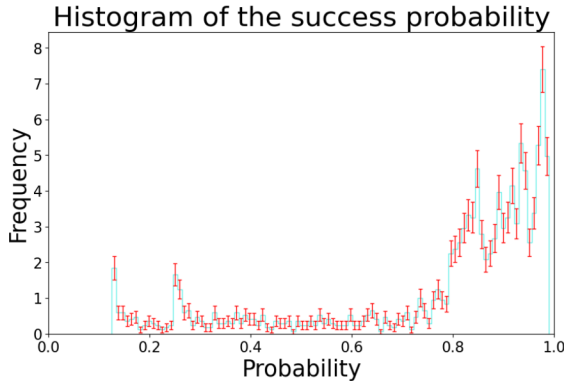
The figure shows that the system is able to converge to the solutions of the eigenvector equation $(\mathbf{M} - \lambda\mathbf{I}) \vec{x} = 0$. However, the success probability of individual configurations that solve the system is lower than in the case of the KPO oscillators. Conversely, the total success probability, obtained by summing over all the solutions, is much higher than in the KPO case, as the curve labelled *solution* approaches unity in both instances.

In the case of the dissipative oscillators, mean-field analysis shows that the fixed points to the different combinations of spins $|\vec{s}\rangle = \otimes_{i=1}^{N_o} |s_i f(t)\rangle$ with $s_i \in \{-1, 1\}$. For the eigenvector problem, the steady states thus correspond to all possible eigenvectors that can be spanned by a set of N_o spins. Since the initial state is the ground state and the evolution is performed adiabatically, the final state will corresponds with the configurations that solve the eigenvector problem. Therefore, it is the same situation that at 4.3.1 and with the KPOs.

To evaluate model's performance, the problem was solved for 1000 instances. The histogram of the resulting success probabilities is shown below:

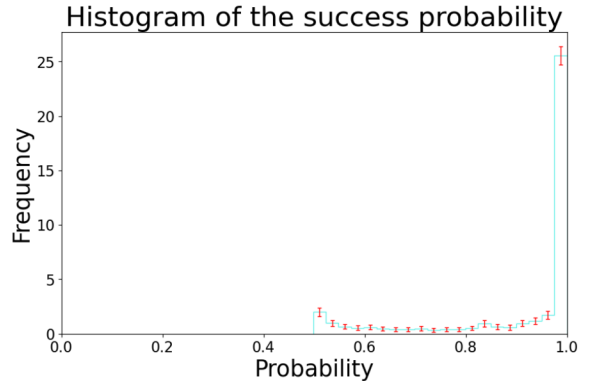


Histogram of the success probability for computing the correct eigenvector using KPO oscillators. The histogram was generated from 1000 instances obtained by solving the eigenvalue problem for random matrix configurations with four coupled oscillators. The simulations parameters are $p(0) = 0$, $p(700/K) = 5K$, $\Delta = 2K$, $\xi_0 = 0.5K$, and a Hilbert space cutoff of $N = 14$. The success probabilities of obtaining a solution different than the trivial solution.



Histogram of the success probability for computing the correct eigenvector using KPO oscillators. The histogram was generated from 1000 instances obtained by solving the eigenvalue problem for random matrix configurations with four coupled oscillators. The simulations parameters are $p(0) = 0$, $p(700/K) = 5K$, $\Delta = 2K$, $\xi_0 = 0.5K$, and a Hilbert space cutoff of $N = 14$. The success probabilities of obtaining a solution.

Histogram of the success probability for computing the correct eigenvector using dissipative oscillators. The histogram was generated from 1000 instances obtained by solving the eigenvalue problem for random matrix configurations with two coupled oscillators. The simulation parameters are $\tau = 300/\gamma_m$, $\eta(0) = 0$, $\eta(1000/\gamma_m) = 2000\gamma_m$, $\xi_0 = 300\gamma_m$, $\Delta = 600\gamma_m$, and a Hilbert space cutoff of $N = 30$. The success probabilities of obtaining a solution different than the trivial solution.

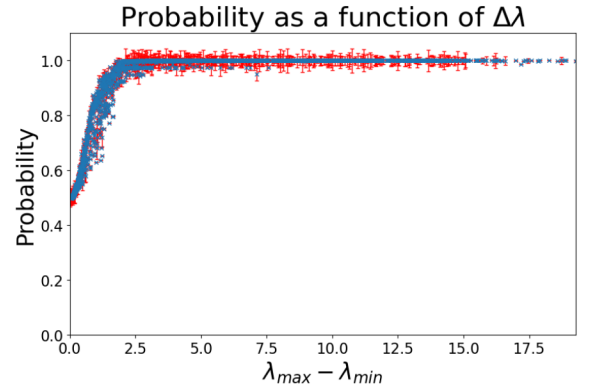
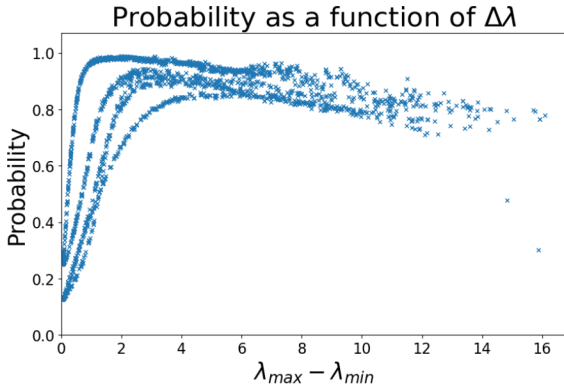


Histogram of the success probability for computing the correct eigenvector using dissipative oscillators. The histogram was generated from 1000 instances obtained by solving the eigenvalue problem for random matrix configurations with two coupled oscillators. The simulation parameters are $\tau = 300/\gamma_m$, $\eta(0) = 0$, $\eta(1000/\gamma_m) = 2000\gamma_m$, $\xi_0 = 300\gamma_m$, $\Delta = 600\gamma_m$, and a Hilbert space cutoff of $N = 30$. The success probabilities of obtaining a solution.

Table 12: Histogram of the success probability for solving the eigenvector problem with random matrices. The results show that successful determinations of the eigenvector occur more frequently than the failures.

These results show that the oscillators systems can successfully solve the eigenvector problem. In fact, the histogram indicates that the dissipative oscillators achieve a higher overall success rate than KPO oscillators. Even though the success probability of non-vanishing solutions remains below 0.5. Furthermore, the histogram reveals that the probability of obtaining incorrect solutions is higher for KPO oscillators rather than for dissipatives ones.

Furthermore, the solutions that are not retrieved correctly are due to the gap between the eigenvalues, $\lambda_{max} - \lambda_{min}$:



Histogram of the success probability for computing the correct eigenvector with KPO oscillators as a function of the eigenvalue $\Delta\lambda = \lambda_{max} - \lambda_{min}$. The histogram was generated from 1000 instances obtained by solving the eigenvalue problem for random matrix configurations with four coupled oscillators. The simulations parameters are $p(0) = 0$, $p(700/K) = 5K$, $\Delta = 2K$, $\xi_0 = 0.5K$, and a Hilbert space cutoff of $N = 14$.

Histogram of the success probability for computing the correct eigenvector with dissipative oscillators as a function of the eigenvalue $\Delta\lambda = \lambda_{max} - \lambda_{min}$. The histogram was generated from 1000 instances obtained by solving the eigenvalue problem for random matrix configurations with two coupled oscillators. The simulation parameters with $\tau = 300/\gamma_m$, $\eta(0) = 0$, $\eta(1000/\gamma_m) = 2000\gamma_m$, $\xi_0 = 300\gamma_m$, $\Delta = 600\gamma_m$ and a cutoff of $N = 30$.

Table 13: Histogram of the success probability for solving the eigenvector problem with random matrices, showing that successful determinations of the eigenvector occur more frequently than failures.

The model's failures to solve the eigenvector problem for some matrices is related with the gap between the eigenvalues of \mathbf{M} , which is a characteristic similar to the presented by others models like [66]. When this gap is small, the success probability of obtaining the correct solution with both oscillators decreases drastically. This occurs because the energy gap between the ground and first excited state shrinks as $\Delta\lambda$ decreases, making the problem more difficult to solve.

These results shows that the solutions obtained from the dissipative oscillators are more consistent than those from the KPOs. As shown in the right figure, the success probability reaches a plateau for dissipative oscillators, whereas for the KPOs it appears to decrease as the eigenvalue gap $\Delta\lambda$ increases.

The results obtained show that both oscillator types are capable of solving the eigenvalue problem. However, the success probability achieved for non-trivial solutions is generally not very high. The highest values are obtained for the KPO, yet they do not exceed 0.8. On the other hand, the results also show that the dissipative oscillators are able to solve the eigenvector problem in almost all cases, converging either to the trivial or non-trivial solution. Moreover, the histograms indicate that while KPO oscillators can also solve the problem, but their performance is inferior to that of dissipative oscillators.

The proposed method for the eigenvector determination shares some similarities with the quantum algorithm for solving linear systems of equations, namely the Harrow-Hassidim-Lloyd algorithm (HHL) [66]. The HHL algorithm is designed to solve linear systems of the form $\mathbf{M}\vec{x} = \vec{b}$ by encoding the independent term into an initial quantum state $|\psi_0\rangle$ as:

$$|\psi_0\rangle = \sum_{i=1} b_i |i\rangle \quad (111)$$

The key idea of the algorithm is to apply the quantum phase estimation procedure [67] to invert the matrix \mathbf{M} , yielding a final quantum state of the form:

$$|\psi_f\rangle = \sum_{i,j=1} (M^{-1})_{i,j} b_j |j\rangle = \sum_{i=1} x_i |i\rangle \quad (112)$$

Where the coefficients x_i correspond to the solution of the system of equations.

The HHL algorithm can be related to the problem of eigenvector determination, since it relies on the fact that an eigenvalue λ associated with a given eigenvector is already known. This allows the problem to be reformulated as:

$$(\mathbf{M} - \lambda\mathbf{I}) \vec{x} = 0 \quad (113)$$

Which corresponds to a homogeneous linear system of equations. Therefore, in practice the HHL algorithm and the proposed method for eigenvector determination solve equivalent problems. In fact, the method proposed for eigenvector determination in I can be easily adapted to solve linear systems of equations by replacing the function $F(\vec{x})$ with:

$$F(\vec{x}) = \left(M\vec{x} - \vec{b} \right)^\dagger \left(M\vec{x} - \vec{b} \right) = \sum_{i=1}^d b_i b_i + \sum_{i,j,k=1}^d x_i x_k M_{i,j}^\dagger M_{j,k} - \sum_{i,j=1}^d x_i b_j M_{i,j} - \sum_{i,j=1}^d b_i x_j M_{i,j}^\dagger \quad (114)$$

The proposed algorithm for eigenvector determination shows certain advantages over the HHL algorithm when dealing with different types of matrices \mathbf{M} . While the HHL algorithm requires \mathbf{M} to be invertible, this is not a constraint for the method proposed here. As a result, the present algorithm can handle undetermined systems of equations, such as 113, whereas the HHL algorithm cannot. Indeed, the HHL algorithm cannot even encode the system 113 because the independent term is $\vec{0}$, which leads to $|\psi_0\rangle = 0$, rendering the algorithm inapplicable.

It is true that [66] proposes a generalization of the HHL algorithm to address non-invertible matrices, at the cost of doubling the number of qubits used for the initial state. However, this generalization only yields the projection of the vector \vec{b} onto the well-conditioned subspace of \mathbf{M} , rather than an actual solution. In contrast, the algorithm proposed here is capable of computing the exact solutions of the problem.

Conversely, the scalability of the HHL algorithm is significantly better than that of the proposed eigenvector method. In HHL, the number of qubits required to encode the vector \vec{x} is $n = \lceil \log_2(N) \rceil$. In contrast, the proposed method requires at least qN oscillators, where N is the number of entries in the solution vector and q is the number of bits assigned to represent each entry. Consequently, the proposed algorithm suffers from a significant scalability limitation.

While the eigenvector method exhibits features that can make it advantageous over HHL, such as the ability to handle a wider class of systems of equations. Its poor scalability renders HHL more practical for future real-world applications.

5 Conclusions

The simulations of the KPO oscillators performed in this work confirm the validity of the cat-state generation reported in [1], as demonstrated by the computed fidelity between the simulated cat states and the theoretical prediction. Furthermore, the simulations show that the KPO model successfully solves the Ising model both with and without an external field, demonstrating its capability to address combinatorial optimization problems. These results are consistent with the findings reported in [1], supporting the conclusion that the obtained results are correct.

Moreover, the simulations demonstrates that a single dissipative oscillator can generate even and odd cat states by crossing the bifurcation by an increasing driving strength. This is in agreement with both mean-field predictions and Lindblad master equation simulations. Despite the presence of squeezing, the system converges to the coherent states predicted of the mean-field theory. Finally, the resolution of the Ising model with dissipative oscillators verifies their capability to implement the quantum computation approach proposed in [1], which was one of the main objectives in this work.

Since both types of oscillators successfully solve the Ising model, they can naturally be extended to address QUBO problems, due to the equivalence between the QUBO and Ising formulations discussed in G. Consequently, this quantum computing approach provides a promising framework for tackling combinatorial optimization tasks using actual quantum adiabatic computing instead of quantum annealing H.

The results of Hopfield network demonstrate that both oscillators are able to solve the Hopfield model and retrieve the stored patterns within the network. Moreover, the simulations confirm that even in cases of higher ground-state degeneracy, the oscillators are still capable of retrieving the correct solutions.

Similarly, the results for the eigenvector problem indicate that both of the quantum oscillator models are able to solve the eigenvector problem. Although the scalability of this eigenvector computation protocol is limited, it still returns correct solutions. Furthermore, the method exhibits certain characteristics that offer improvements over the HHL algorithm [66]. These findings fulfil the final objective established for the work.

6 Future work

In this study, a brief introduction to a quantum computation using bifurcations was presented, following the approach of [1]. Moreover, this framework was extended to other nonlinear oscillators defined in purely dissipative systems, as in [2]. Nevertheless, there remain avenues for further research beyond the scope of this work.

All simulations and results presented here are based on the coupling proposed by [1], given by $\sum_{i,j=1} a_i a_j^\dagger + a_j a_i^\dagger$. The coupling coefficients $J_{i,j}$ were employed to solving the Ising model. However, this approach assumes $J_{i,j} = J_{j,i}$, which restricts the method to solving Ising QUBOs with symmetric coefficients. Consequently, it would be interesting to explore a generalization of this model to the case where the matrix \mathbf{J} is not symmetric.

Moreover, the dissipative oscillators used in this study were previously investigated by [2, 34] in the context of quantum associative memories. Their work relied on the presence of metastable states in the dissipative oscillator to develop these memories. However, their analysis was limited to the case of a single oscillator. Therefore, it would be interesting to study the impact of the interaction term on metastability in multi-oscillator systems, with the aim of potentially improving the performance of associative memories.

Furthermore, in this study the dissipative oscillator was analysed for the case $(n, m) = (2, 4)$, since this is the regime in which cat states are generated. However, the dynamics change significantly for other values of the exponents, as shown in [2]. Therefore, generalizing the solution of the mean-field equations presented here for the coupled oscillators would be valuable for studying a wider range of coupled systems.

Additionally, simulations using 114 can be performed to provide a better comparison with the HHL algorithm.

Finally, although the model is purely quantum, the computation is classical, since the measurement outcomes are 1 or -1 . Nonetheless, exploring new Hamiltonians for the oscillators could enable genuinely quantum outcomes after the bifurcation. A potential application of this generalization is the design of a purely quantum Hopfield network, where the stored memories correspond to quantum states, as in [2, 34].

A Hopfield model

The Hopfield model, introduced by John Hopfield in [55], is a network model with associative memory. This system is capable of storing p patterns or memories thanks to a weight matrix J_{ij} , which encodes the patterns as energy minima. As a result, when a random input is provided to the system, it evolved toward the stored closest pattern to that input. In this way, the system remembers one of the memorized states.

The dynamic of the Hopfield network are governed by:

$$E = -\frac{1}{2} \sum_{i \neq j}^N J_{ij} \sigma^i \sigma^j \quad J_{ij} = \frac{1}{N} \sum_{\mu=1}^p \xi_i^\mu \xi_j^\mu \quad (115)$$

Here, E represent the energy of the network, $\sigma^i \in \{-1, 1\}$ is the state of the i -th neurons, J_{ij} are the synaptic weights of the system, N the number of neurons, and ξ^μ denotes the patterns to be stored.

The overlap with pattern μ is then defined as:

$$m_z^\mu = \frac{1}{N} \sum_i \xi_i^\mu \sigma^i \quad (116)$$

The overlap is a measure of the degree of similarity between the current state of the system and the stored pattern or memory μ . To better understand the network's behavior, we can do an analogy with the Ising model, where each neuron corresponds with a node. The state of a neuron can be identified with the spin of a node: a fired neuron corresponds to $\sigma^i = 1$, analogous with a spin aligned along the z axis, while $\sigma^i = -1$ correspond with an anti-aligned spin.

Thus, the physical interpretation of the overlap is the degree of similarity between the current and stored pattern. Therefore, the idea behind the model is to study the network's ability to remember stored patterns when an input is given to the network.

B Limit of the amplification of the non-lineal Hamiltonian for the KPO

In this section, I will discuss a limit of the performance of the simulation for the KPO oscillators. Simulations show an odd behaviour for large values of p :

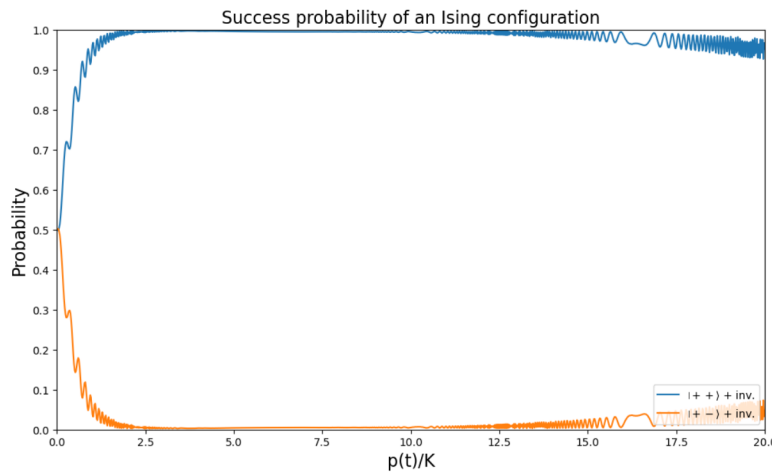


Figure 12: Success probability of a configuration as a function of p for 2 coupled oscillators. The simulation parameters are $p(0) = 0$, $p(1000/K) = 20K$, $\xi_0 = 0.5K$ and $N = 20$.

The picture shows that around $p \sim \frac{N}{2} = 10$, the quantum state no longer converge toward the theoretical state. In general, for simulations with more than 2 coupled oscillators this behaviour appears for $p \leq \frac{N}{2}$. This occurs because, in this regime, the photon pump is so strong that the total Hamiltonian is approximately $H \approx H_{NL}$, making the term $H = \frac{K}{2} (a^\dagger)^2 a^2$ negligible. As a result, the dynamic can be divided in 3 regimes:

- $p(t) \rightarrow 0$:

$$H = \sum_i \left(\Delta_i a_i^\dagger a_i + \frac{K}{2} (a_i^\dagger)^2 a_i^2 \right) - \frac{\xi_0}{2} \sum_i \sum_j J_{ij} (a_i^\dagger a_j + a_j^\dagger a_i) \quad (117)$$

In this regime, the photon pump becomes negligible because $p(t) \approx 0$. Consequently, the ground state at this stage corresponds to the vacuum $|0\rangle$.

- $p(t) \sim K$:

$$\begin{aligned} H &= \sum_i \left(\Delta_i a_i^\dagger a_i + \frac{K}{2} (a_i^\dagger)^2 a_i^2 - \frac{p(t)}{2} (a_i^2 + (a_i^\dagger)^2) \right) - \frac{\xi_0}{2} \sum_i \sum_j J_{ij} (a_i^\dagger a_j + a_j^\dagger a_i) \\ &= \sum_i \left(\frac{K}{2} (a_i^\dagger)^2 a_i^2 - \frac{p(t)}{2} (a_i^2 + (a_i^\dagger)^2) \right) + H_p \end{aligned} \quad (118)$$

In this regime, the pump is of order $\mathcal{O}(K)$, so the detuning and the Ising part of the Hamiltonian become smaller than the non-linear terms. These two contributions can therefore be treated as perturbations of the non linear Hamiltonian H_p . This leads to an evolution that generates cat states, which can be used to solve the Ising model. Up this point, this is the regime in which the simulations outcomes have physical meaning.

- $p(t) \gg K$:

$$H = \sum_i \left(\Delta_i a_i^\dagger a_i + \frac{K}{2} (a_i^\dagger)^2 a_i^2 - \frac{p(t)}{2} (a_i^2 + (a_i^\dagger)^2) \right) - \frac{\xi_0}{2} \sum_i \sum_j J_{ij} (a_i^\dagger a_j + a_j^\dagger a_i) = -\frac{p(t)}{2} \sum_i (a_i^2 + (a_i^\dagger)^2) + H_p \quad (119)$$

In this regime, the pump strength is much larger than the term proportional to K , allowing the latter to be treated as a small perturbation to the system Hamiltonian H_p . Because the system undergoes an adiabatic evolution, the final state approximates the ground state of the Hamiltonian $H = -\frac{p(t)}{2} (a^2 + (a^\dagger)^2)$ with corrections arising from the perturbation.

This explains why the system no longer converge to the solution of the Ising model. In this regime, the ground state is no longer a cat state. To check this hypothesis the overlap between the quantum state and the ground state of H_{NL} is computed:

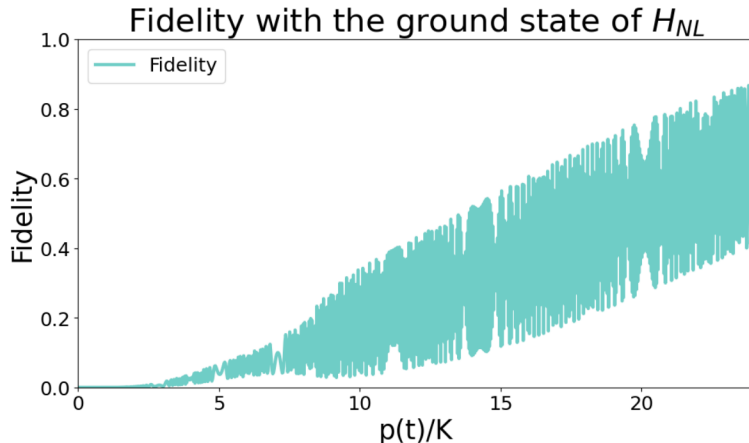


Figure 13: Overlap with the ground state H_{NL} with the simulation result as function of p for 4 coupled oscillators. The simulation parameters are $K = 1.0$, $p(0) = 0$, $p(1200/K) = 24K$, $\xi_0 = 0.5K$ and $N = 14$. The couplings that has been chosen for the simulation are $J_{ij} = 1 - \delta_{ij}$ (δ_{ij} is the Kronecker delta).

As shown in the figure, for large values of p , the overlap with the ground state of H_{NL} increases, which is consistent with the previous discussion. Moreover, as discussed in C, the ground state of H_{NL} is unbounded for below, as it corresponds to the inverted potential of the harmonic oscillator. Because the system undergoes adiabatic evolution, it tends toward the ground state of H_{NL} , whose energy is $E_g = -\infty$. However, such energy values cannot be reached in a computational simulations because the Hilbert space spanned by $\{|n\rangle\}_{n=0}^{\infty}$ is truncated by a cutoff N , limiting the basis to $\{|n\rangle\}_{n=0}^N$. As a result, the ground state energy obtained from the simulations is $E_g = f(N) > -\infty$ energy. Therefore, for sufficiently large values of p , the choice of cutoff N significantly affects the simulation results, as shown in C.

C Energy of the ground state of the H_{NL}

The situation that is going to be analyzed is when $p \gg K$. In this regime, the Hamiltonian of the non linear oscillator can be approximated by only H_{NL} :

$$H \approx H_{\text{NL}} = -\frac{p}{2} \left(a^2 + (a^\dagger)^2 \right) \quad (120)$$

Now, taking into account that $a \sim x + iy$, the Hamiltonian can be rewritten as:

$$H \sim p (y^2 - x^2) \quad (121)$$

This is quite similar to the Hamiltonian of the harmonic oscillator:

$$H \sim (y^2 + x^2) \quad (122)$$

The potential in the harmonic oscillator corresponds to:

$$V(x) \sim x^2 \quad (123)$$

This corresponds with an attractive potential, which is why the harmonic oscillator has bounded states and a discrete energy spectrum. However, in our system, the potential has the same shape but with the opposite sign, making it a repulsive potential. Since the potential is repulsive, the energy is no longer bounded from below. As a result, the higher energy states of the harmonic oscillator will now minimize the energy.

This implies that the lowest-energy state in our system corresponds to the highest excitation vector in the Hilbert space, $|N\rangle \in \mathcal{H}$. Ideally, the Hilbert space \mathcal{H} is infinite dimensional, but since infinite dimensional spaces cannot be simulated on classical computers, we impose a cutoff N to the dimension.

Consequently, the minimum energy state will corresponds to $|N\rangle$, causing the system to tends toward this cutoff state. This leads to a strong dependence on the energy on N , making the simulation results for sufficiently large p incorrect.

Now, the goal is to verify that the ground state of H_{NL} is not bounded for below and check that it depends on the imposed cutoff. To this end, an upper bound for the ground state energy will be estimated using the variational principle. The idea is to study wether this upper bound decrease without limit as a function of p , and how it behaves with respect to the value of the cutoff N .

$$E_0 \leq \langle \alpha | H | \alpha \rangle \quad (124)$$

The state used to set the upper bound will be a coherent state α , since prior to the dominance of the nonlinear terms, the system evolves as a linear combination of coherent states. However, in this section, the finite size of the Hilbert space due to the cutoff, will be explicitly taken into account in order to explain the simulation results. Therefore, the normalized coherent state is defined as:

$$|\alpha\rangle = \frac{e^{-\alpha^2}}{\sqrt{\Gamma(N+1, \alpha^2)}} \sum_{n=0}^N \frac{\alpha^n}{\sqrt{n!}} |n\rangle \quad (125)$$

Here, N denotes the cutoff of the Hilbert space used in the simulation, and $\Gamma(N+1, \alpha^2)$ is the regularized incomplete upper gamma function, it is defined as [68]:

$$\Gamma(N, x) = \frac{1}{\Gamma(N)} \int_x^\infty dt e^{-t} t^{N-1} \quad (126)$$

Here, $\Gamma(N)$ stands for the Gamma function. Using this state, the expected value of the Hamiltonian is computed as follows:

$$\langle \alpha | \frac{K}{2} (a^\dagger)^2 a^2 - \frac{p}{2} (a^2 + (a^\dagger)^2) | \alpha \rangle \quad (127)$$

The first term:

$$\langle \alpha | (a^\dagger)^2 a^2 | \alpha \rangle = \frac{e^{-\alpha^2}}{\Gamma(N+1, \alpha^2)} \sum_{k,n=0}^N \frac{\alpha^{n+k}}{\sqrt{n!k!}} \langle k | (a^\dagger)^2 a^2 | n \rangle = \alpha^4 e^{-\alpha^2} e_{N-1}(\alpha^2) \quad (128)$$

Here, e_n denotes the exponential series truncated after $N+1$ terms [68]:

$$e_N(\alpha) = \sum_{n=0}^{N-1} \frac{\alpha^n}{n!} = \Gamma(N, \alpha) e^\alpha \quad (129)$$

The evaluation of the first term yields:

$$\langle \alpha | (a^\dagger)^2 a^2 | \alpha \rangle = \alpha^4 \Gamma(N-1, \alpha^2) \quad (130)$$

The result of the second term is:

$$\langle \alpha | a^2 + (a^\dagger)^2 | \alpha \rangle = \frac{e^{-\alpha^2}}{\Gamma(N+1, \alpha^2)} \sum_{n,k=0}^N \frac{\alpha^{n+k}}{\sqrt{n!k!}} \langle k | (\sqrt{n(n-1)} | n-2 \rangle + \sqrt{(n+2)(n+1)} | n+2 \rangle) \quad (131)$$

$$\frac{2e^{-\alpha^2}}{\Gamma(N+1, \alpha^2)} \sum_{n=0}^{N-2} \frac{\alpha^{2n+2}}{n!} = 2\alpha^2 \Gamma(N-1, \alpha^2) \quad (132)$$

Therefore, the expected value of the Hamiltonian is:

$$\langle \alpha | H | \alpha \rangle = \left[\frac{K}{2} \alpha^4 - p \alpha^2 \right] \frac{\Gamma(N-1, \alpha^2)}{\Gamma(N+1, \alpha^2)} \quad (133)$$

Finally, to observe that the ground state of the Hamiltonian in this regime is not lower bounded, and increasing p produce transitioning to states of progressively lower energy, which depends on the cutoff. The value of α that minimize the inequality is computed. To achieve this task, a new parameter $x = \alpha^2$ is defined:

$$f(x) = \left(\frac{K}{2} x^2 - px \right) \frac{\Gamma(N-1, x)}{\Gamma(N+1, x)} \longrightarrow f'(x) = (Kx - p) \frac{\Gamma(N-1, x)}{\Gamma(N+1, x)} + \left(\frac{K}{2} x^2 - px \right) \frac{d}{dx} \left[\frac{\Gamma(N-1, x)}{\Gamma(N+1, x)} \right] = 0 \quad (134)$$

This equation is difficult to solve analytically, and for a given value of N and p , numerical solutions can be found. However, since the goal is to obtain an analytical expression depending on N and p , a few approximations are made.

First, it is assumed that in the simulations $p \leq N$. This restriction is based on the fact that for larger values of p , the effect of the Hilbert space cutoff becomes significant, leading to simulation results physically unreliable.

Moreover, from this point onward, it is assumed that $x \sim N/2$. This choice is based the results from 12, where boundary effects begin to appear around this value.

Furthermore, to ensure that the simulation results are meaningful, the cutoff N must be sufficiently large to approximate the real system dynamics. Thus, it will be assumed that N is large enough to approximate $N+1 \approx N$.

Now, the fact that $\frac{d}{dx} \left[\frac{\Gamma(N-1,x)}{\Gamma(N+1,x)} \right] \approx 0$ is shown, which allows to neglect this term. To demonstrate this, the following relationship between the incomplete gamma functions defined in [68] is used:

$$1 = \Gamma(N, x) + \gamma(N, x) \quad (135)$$

Here, the function $\gamma(N, x)$ corresponds with the lower incomplete gamma function [68]:

$$\gamma(N, x) = \frac{1}{\Gamma(N)} \int_0^x dt e^{-t} t^{N-1} \quad (136)$$

Therefore, the resultant function:

$$\frac{\Gamma(N-1, x)}{\Gamma(N+1, x)} = \frac{\Gamma(N-1, x)}{1 - \gamma(N+1, x)} \quad (137)$$

The function γ is a monotonically non-decreasing function, so I aim to show that it is upper bounded for the situation in which $x = N/2$. While it is known by definition that $\gamma(N, x) \leq 1$, the goal here is to find an upper bound that decrease with the increase of N :

$$\gamma(N+1, N/2) = \frac{1}{\Gamma(N+1)} \int_0^{N/2} dt e^{-t} t^N = \frac{1}{\Gamma(N+1)} \sum_{k=0}^{\frac{N}{2}-1} \int_k^{k+1} dt e^{-t} t^N \leq \frac{1}{\Gamma(N+1)} \sum_{k=0}^{\frac{N}{2}-1} e^{-k} k^N \quad (138)$$

Since it is already known that $\gamma(N, x) \leq 1$, it is verified that the proposed upper bound does not exceed 1, as exceeding this value would result in a less accurate estimation than the known bound. This expression can be rewritten in terms of the polylogarithm function, as defined in [69]:

$$\text{Li}_n(x) = \sum_{k=1}^{\infty} \frac{x^k}{k^n} \quad \text{Li}_{n+1}(x) = \int_0^x dt \frac{\text{Li}_n(t)}{t} \quad (139)$$

The function is defined on $D = \{z \in \mathbb{C} / |z| < 1\}$, but it admits an analytic extension in the situation for $n > 0$, as presented in [69].

$$\text{Li}_n(x) = \frac{x}{\Gamma(n)} \int_0^{\infty} dt \frac{t^{n-1}}{e^t - x} \quad (140)$$

Therefore, the upper bound can be expressed as:

$$\frac{1}{\Gamma(N+1)} \sum_{k=0}^{\frac{N}{2}-1} e^{-k} k^N \leq \frac{1}{\Gamma(N+1)} \sum_{k=0}^{\infty} e^{-k} k^N = \frac{1}{\Gamma(N+1)} \text{Li}_{-N}(e^{-1}) \quad (141)$$

In this situation, taking into account that N is sufficiently large, the following limit can be used [70, 71, 72, 73]:

$$\lim_{s \rightarrow -\infty} \text{Li}_s(e^\mu) \longrightarrow \Gamma(1-s)(-\mu)^{s-1} \quad (142)$$

For this situation:

$$\text{Li}_{-N}(e^{-1}) \longrightarrow \Gamma(N+1) \quad (143)$$

Therefore, the first term can be expressed as:

$$\frac{1}{\Gamma(N+1)} \text{Li}_{-N}(e^{-1}) \longrightarrow 1 \quad (144)$$

Consequently:

$$\frac{1}{\Gamma(N+1)} \sum_{k=0}^{\frac{N}{2}-1} e^{-k} k^N \leq \frac{1}{\Gamma(N+1)} \text{Li}_{-N}(e^{-1}) \longrightarrow 1 \quad (145)$$

Therefore, the obtained bound does not exceed 1. Next, the Stirling approximation for the Γ function, $\ln N! = N \ln N - N + \frac{1}{2} \ln N$ [74], is applied. This allows the expression to be rewritten as:

$$\frac{1}{\Gamma(N+1)} \sum_{k=0}^{\frac{N}{2}-1} e^{-k} k^N = \sum_{k=0}^{\frac{N}{2}-1} e^{N[1+\ln(\frac{k}{N})]-k-\frac{1}{2}\ln N} \leq \frac{N}{2} e^{N[1+\ln(\frac{(N/2-1)}{N})]-N/2+1-\frac{1}{2}\ln N} \quad (146)$$

Now, assuming that $N \gg 1$:

$$\frac{N}{2} e^{N[1+\ln(\frac{(N/2-1)}{N})]-N/2+1-\frac{1}{2}\ln N} = \frac{\sqrt{N}}{2} e^{N[\frac{1}{2}-\ln 2]+1} \quad (147)$$

Since $\frac{1}{2} - \ln 2 = -0.193 < 0$, this upper bound decrease exponentially. This implies that, for sufficiently large N , $\gamma \leq e^{-aN} \lll 1$, with $a > 0$.

This justify the Taylor expansion to first order $\frac{1}{1-\gamma(N+1,x)} = 1 + \gamma + \mathcal{O}(\gamma^2)$:

$$\frac{\Gamma(N-1,x)}{1-\gamma(N+1,x)} = \Gamma(N-1,x) (1 + \gamma(N+1,x)) \quad (148)$$

The derivative of this function:

$$\begin{aligned} \frac{d}{dx} \left[\frac{\Gamma(N-1,x)}{\Gamma(N+1,x)} \right] &= -\frac{x^{N-2} e^{-x}}{\Gamma(N-2)} (1 + \gamma(N+1,x)) + \frac{\Gamma(N-1,x)}{\Gamma(N+1)} x^N e^{-x} = \\ &\quad \frac{x^N e^{-x}}{\Gamma(N-2)} \left[\frac{\Gamma(N-1,x)}{N(N-1)} - \frac{1 + \gamma(N+1,x)}{x^2} \right] \end{aligned} \quad (149)$$

The summation within brackets is now analyzed:

$$\frac{\Gamma(N-1,x)}{N(N-1)} - \frac{1 + \gamma(N+1,x)}{x^2} \quad (150)$$

The fact that both gamma functions have upper bounds, due to being regularized ($\Gamma(N-1,x) < 1$ and $1 + \gamma(N-1,x) < 2$), is taken into account. As previously discussed, $x \sim N/2$ is assumed:

$$\frac{\Gamma(N-1,x)}{N(N-1)} - \frac{1 + \gamma(N+1,x)}{x^2} \sim \frac{1}{N^2} - \frac{4}{N^2} \sim -\frac{1}{N^2} \quad (151)$$

Therefore, the behavior of the derivative is:

$$\frac{d}{dx} \left[\frac{\Gamma(N-1,x)}{\Gamma(N+1,x)} \right] = -\frac{x^N e^{-x}}{\Gamma(N-2)} = N^{-2} \sim -N^{-2} \frac{N^N e^{-N/2}}{2^N (N-2)!} \sim N^{-2} \sim -N^{-2} \frac{N^N e^{-N/2}}{2^N \sqrt{N-2}} \left(\frac{e}{N-2} \right)^{N-2} \quad (152)$$

Here, the Stirling approximation has been used, along with the assumption that $x \sim N/2$. Expanding the expression, we find:

$$\frac{d}{dx} \left[\frac{\Gamma(N-1, x)}{\Gamma(N+1, x)} \right] \sim e^{-N} \quad (153)$$

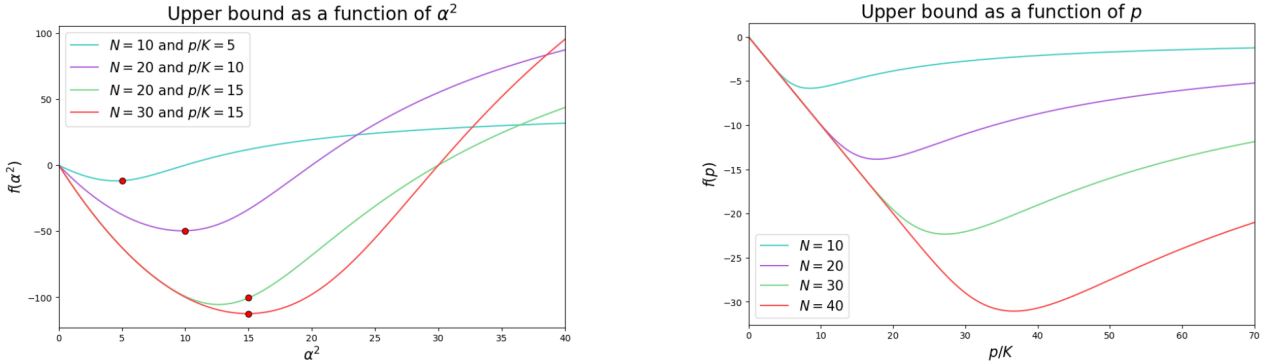
Therefore, since the cutoff used on the simulations is of order $N \geq 13$, the derivative will be of order $\mathcal{O}(10^{-6})$, while the other terms are of order $\mathcal{O}(1)$. Thus, the derivative can be neglected. Moreover, because the derivative is negligible, the function $\frac{\Gamma(N-1, x)}{\Gamma(N+1, x)} \approx \text{cte}$ can be approximated as a constant. Therefore, the derivative of the function $f(x)$ becomes:

$$f'(x) = (Kx - p) \frac{\Gamma(N-1, x)}{\Gamma(N+1, x)} + \left(\frac{K}{2} x^2 - px \right) \frac{d}{dx} \left[\frac{\Gamma(N-1, x)}{\Gamma(N+1, x)} \right] \approx (Kx - p) A = 0 \quad (154)$$

Where $A = \left[\frac{\Gamma(N-1, x_{\min})}{\Gamma(N+1, x_{\min})} \right]$. The resultant equation is straightforward and lead to the solution $x_{\min} = p/K$. Therefore, the upper bound for the energy of the H_{NL} is:

$$E_0 \leq \langle \alpha | H_{\text{NL}} | \alpha \rangle = \frac{-p}{2K} \frac{\Gamma(N-1, p/K)}{\Gamma(N+1, p/K)} \quad (155)$$

Since the function $\frac{\Gamma(N-1, p/K)}{\Gamma(N+1, p/K)} \geq 0$, increasing the photon pump leads to progressively lower energy values, resulting in a system that cannot be reliably simulated on a computer.



$f(\alpha^2)$ function for different values of N and p . This figure shows that the estimation of the minima (red dot) of the upper bound is correct, despite all the approximations. Even for situations where $\alpha^2 \neq N/2$, the approximation of the minimum is quite good.

This figure shows the value of the upper bound of the energy when it is minimized ($\alpha^2 = p/K$). The picture shows that the upper bound decrease when p and N increase. This matches the simulation results and proves that the energy of the ground state depends on N for large p .

D Mean-field approximation for one oscillator

The mean-field equation for the dissipative oscillator 67 was computed in [2]:

$$\dot{\alpha} = -\frac{\gamma_1}{2}\alpha - i\Delta\alpha - n\eta (\alpha^*)^{n-1} e^{-in\theta} - \frac{m}{2}\gamma_m |\alpha|^{2(m-1)} \alpha \quad (156)$$

This equation is obtained by neglecting the correlations between the operators in the Heisenberg picture, $\langle a^x (a^\dagger)^y \rangle \approx \langle a^x \rangle \langle (a^\dagger)^y \rangle$ in the limit $|\alpha|^2 \rightarrow \infty$. For the case of interest, where $(n, m) = (2, 4)$ and $\gamma_1 = 0$, the equation simplifies. This corresponds to the strong symmetry regime, where the steady states are cat states with even and odd parity. The amplitude of the coherent component of these states can be determined using the mean-field approximation,

which corresponds to the fixed points of 156. In this case the equation reduces to:

$$\dot{\alpha} = -i\Delta\alpha - 2\eta\alpha^*e^{-i2\theta} - 2\gamma_m |\alpha|^6 \alpha \quad (157)$$

α is the coherent amplitude of the lobes, which is generally a complex number. Analyzing the fixed points of this equation provides information about the coherent component of the resulting cat states. Therefore, the following system is solved to determine the fixed points:

$$\begin{cases} \dot{\alpha} = -i\Delta\alpha - 2\eta\beta e^{-i2\theta} - 2\gamma_m \alpha^4 \beta^3 \\ \dot{\beta} = i\Delta\beta - 2\eta\alpha e^{-i2\theta} - 2\gamma_m \alpha^3 \beta^4 \end{cases} \quad (158)$$

Here, β represent the complex conjugate of α . The phase θ produces a rotation of the final result on the Wigner function space. Therefore, the equations can be simplified by taking $\theta = \frac{\pi}{2}$, which ensures that the lobes of the final pattern lie along the position axis in the Wigner function. The fixed points of these equations are computed:

$$\begin{cases} 0 = -i\frac{\Delta}{2\gamma_m}\alpha + \frac{\eta}{\gamma_m}\beta - \alpha^4\beta^3 \\ 0 = i\frac{\Delta}{2\gamma_m}\beta + \frac{\eta}{\gamma_m}\alpha - \alpha^3\beta^4 \end{cases} \quad (159)$$

These equations allow us to express all the parameters of the oscillator in units of γ_m . Therefore, all the parameters are rescaled by γ_m :

$$\frac{\Delta}{\gamma_m} \longrightarrow \Delta$$

$$\frac{\eta}{\gamma_m} \longrightarrow \eta \quad (160)$$

$$t\gamma_m \longrightarrow t$$

Now, the system of equations:

$$\begin{cases} 0 = -i\frac{\Delta}{2}\alpha + \eta\beta - \alpha^4\beta^3 \\ 0 = i\frac{\Delta}{2}\beta + \eta\alpha - \alpha^3\beta^4 \end{cases} \quad (161)$$

The first solution found is the trivial solution $(\alpha, \beta) = (0, 0)$, which corresponds to the squeezed vacuum state of the oscillator. To determine amplitudes of the cat state lobes, one must look for the nontrivial solutions:

$$\begin{cases} 0 = -i\frac{\Delta}{2}\alpha + \eta\beta - \alpha^4\beta^3 \\ 0 = i\frac{\Delta}{2}\beta + \eta\alpha - \alpha^3\beta^4 \end{cases} = \begin{cases} 0 = -i\frac{\Delta}{2} + \eta\frac{\beta}{\alpha} - \alpha^3\beta^3 \\ 0 = i\frac{\Delta}{2} + \eta\frac{\alpha}{\beta} - \alpha^3\beta^3 \end{cases} \quad (162)$$

The following equation can be obtained:

$$-i\frac{\Delta}{2} + \eta\frac{\beta}{\alpha} = i\frac{\Delta}{2} + \eta\frac{\alpha}{\beta} \quad (163)$$

Now, two new variables are defined $c = \frac{\alpha}{\beta}$ and $b = \frac{\Delta}{\eta}$. Therefore, using these variables the previous equation can be solved, which result on:

$$c = \frac{1}{2} \left[-ib \pm \sqrt{4 - b^2} \right] \quad (164)$$

Using now the fact that $\alpha = c\beta$ and the previous equations, the solution for α and β is obtained:

$$\beta^6 = h^6 = \frac{i\frac{\Delta}{2} + \eta c}{c^3} \quad \alpha = c \left(\frac{i\frac{\Delta}{2} + \eta c}{c^3} \right)^{1/6} \quad (165)$$

Now, recalling that $\alpha = q + ip$, the solution can be expressed in terms of the variables of position q and momentum p :

$$\begin{cases} \alpha = q + ip \\ \beta = q - ip \end{cases} \longrightarrow \begin{cases} q = (c+1)\frac{h}{2} \\ p = (c-1)\frac{hi}{2} \end{cases} \quad (166)$$

There are two regimes in terms of the value of $b = \frac{\Delta}{\eta}$:

- $b > 2$: In this case, c is an pure imaginary number, while $h = \frac{i\frac{\Delta}{2} + i\eta|c|}{-i|c|^3} = -\frac{\frac{\Delta}{2} + \eta|c|}{|c|^3} \in \mathbb{R}$. Therefore, the result for the position and momentum is:

$$\begin{cases} q = (c+1)\frac{h}{2} \\ p = (c-1)\frac{hi}{2} \end{cases} \longrightarrow \begin{cases} q = (i|c|+1)\frac{h}{2} \in \mathbb{C} \\ p = (i|c|-1)\frac{hi}{2} \in \mathbb{C} \end{cases} \quad (167)$$

Since the position and momentum are real variables, this result does not have physical sense. Therefore, there is only one fixed point for $b > 2$, which correspond to the trivial solution. The stability of this fixed point can be analysed using linear stability analysis $\alpha = \delta\alpha$ and $\beta = \delta\beta$.

$$\begin{pmatrix} \delta\dot{\alpha} \\ \delta\dot{\beta} \end{pmatrix} = \begin{pmatrix} -i\frac{\Delta}{2} & \eta \\ \eta & i\frac{\Delta}{2} \end{pmatrix} \begin{pmatrix} \delta\alpha \\ \delta\beta \end{pmatrix} \quad (168)$$

The eigenvalues of this matrix are:

$$\lambda_+ = \eta \frac{\sqrt{4 - (\frac{\Delta}{\eta})^2}}{2} \quad \lambda_- = -\eta \frac{\sqrt{4 - (\frac{\Delta}{\eta})^2}}{2} \quad (169)$$

If $b^2 = \left(\frac{\Delta}{\eta}\right)^2 > 2$, both eigenvalues are complex; therefore, this fixed point corresponds to a center. However, when $\frac{\Delta}{\eta}$ decreases below 2, the eigenvalues become real. In this regime, the fixed point becomes a saddle point, exhibiting different stability along the two distinct directions:

$$|\lambda_+\rangle = \begin{pmatrix} -2i \frac{i(\frac{\Delta}{\eta})}{1+i\sqrt{4-(\frac{\Delta}{\eta})^2}} \\ 1 \end{pmatrix} \quad |\lambda_-\rangle = \begin{pmatrix} -2i \frac{i(\frac{\Delta}{\eta})}{1-i\sqrt{4-(\frac{\Delta}{\eta})^2}} \\ 1 \end{pmatrix} \quad (170)$$

- $b^2 = \left(\frac{\Delta}{\eta}\right)^2 < 4$: In this regime, there is a possibility of finding a h such that $q, p \in \mathbb{R}$, since now c is not longer pure imaginary:

$$c = \frac{1}{2} \left[-ib \pm \sqrt{4 - b^2} \right] = e^{\pm i \arctan\left(\frac{b}{\sqrt{4-b^2}}\right)} \quad (171)$$

The value of c is just a phase, it allow to simplify the expression for h :

$$h^6 = \frac{\frac{i\Delta}{2} + \eta c}{c^3} = \left(\frac{i\Delta}{2} + \eta c \right) (c^*)^3 \quad (172)$$

Extracting η and using that $c = \frac{1}{2} [-ib \pm \sqrt{4 - b^2}]$:

$$h^6 = \frac{\eta}{2} \sqrt{4 - b^2} e^{\mp 3i \arctan\left(\frac{b}{\sqrt{4-b^2}}\right) + i\pi l} \quad (173)$$

With l being 0 if the positive branch of c is selected and 1 otherwise. Therefore, the value of h is:

$$h = \left(\frac{\eta}{2}\right)^{1/6} (4 - b^2)^{1/12} e^{\mp \frac{i}{2} \arctan\left(\frac{b}{\sqrt{4-b^2}}\right) + i\frac{\pi}{6}l + \frac{2ik\pi}{6}} \quad (174)$$

Here $k \in \{0, 1, 2, 3, 4, 5\}$ indicates the different solutions of the root. Finally, the solution for the position and momentum can be obtained from:

$$\begin{cases} q = (c + 1)\frac{h}{2} \\ p = (c - 1)\frac{hi}{2} \end{cases} \quad (175)$$

$$q = \left(\frac{\eta}{2}\right)^{1/6} (4 - b^2)^{1/12} e^{\mp \frac{i}{2} \arctan\left(\frac{b}{\sqrt{4-b^2}}\right) + i\frac{\pi}{6}l + \frac{2ik\pi}{6}} \frac{1}{2} \left(e^{\pm i\frac{1}{2} \arctan\left(\frac{b}{\sqrt{4-b^2}}\right)} + e^{\mp i\frac{1}{2} \arctan\left(\frac{b}{\sqrt{4-b^2}}\right)} \right) e^{\pm \frac{i}{2} \arctan\left(\frac{b}{\sqrt{4-b^2}}\right)} \quad (176)$$

The only values of l and k that leads to a real solutions are $l = 0$ and $k = 0, 3$. Therefore, there are two fixed points, $\alpha = q + ip$ with:

$$q = \pm \left(\frac{\eta}{2}\right)^{1/6} \left(4 - \left(\frac{\Delta}{\eta}\right)^2\right)^{1/12} \cos \left[\frac{1}{2} \arctan \left(\frac{\Delta}{\eta \sqrt{4 - \left(\frac{\Delta}{\eta}\right)^2}} \right) \right] \quad (177)$$

And momentum:

$$p = \mp \left(\frac{\eta}{2}\right)^{1/6} \left(4 - \left(\frac{\Delta}{\eta}\right)^2\right)^{1/12} \sin \left[\frac{1}{2} \arctan \left(\frac{\Delta}{\eta \sqrt{4 - \left(\frac{\Delta}{\eta}\right)^2}} \right) \right] \quad (178)$$

In the situation in which $b = \frac{\Delta}{\eta} \rightarrow 0$, the expressions are simplified to:

$$q = \pm \left(\frac{\eta}{\gamma_m}\right)^{1/6} \quad p = 0 \quad (179)$$

They correspond to two stable fixed points. The parameter Δ regulates the oscillations by changing their frequency but not the amplitude. This is logical since this term represents the harmonic oscillator part of the system, Δ can be identified as its frequency.

The parameter η regulates the amplitude of the cat states' lobes and the separation between fixed points. Furthermore, the value of eta determines the validity of the mean-field approximation, which holds when $|\alpha|^2 \gg 1$.

Therefore, the point $\frac{\Delta}{\eta} = 2$ defines a phase transition between a phase with sustained oscillations and another one with fixed stable points:

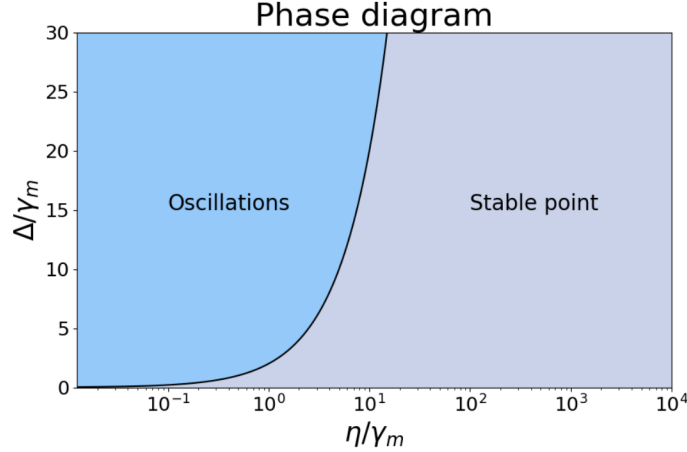


Figure 14: Phase diagram of the dissipative oscillator introduced in [2] for the special cas $\gamma_1 = 0$ and $(n, m) = (2, 4)$ (strong symmetry). The diagram was obtained by solving the mean-field equations derived in [2] for the parameter of interest. The system initially exhibits a phase where the linear stability analysis reveals purely imaginary eigenvalues. In this regime, the oscillator undergoes oscillations in both position and momentum. Conversely, when the pump falls below the threshold $\frac{\Delta}{\eta} = 2$, two new stable fixed points emerge, corresponding to the coherence phases of the cat state.

To check the validity of the solutions, the mean-field equations has been solved numerically:

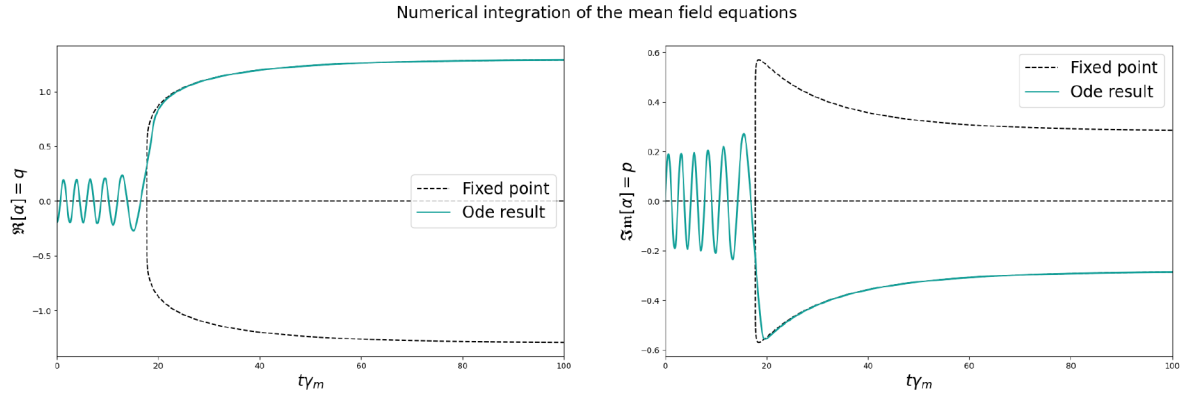


Figure 15: Numerical resolution of the mean-field equations with $\eta_f = 6\gamma_m$, $\Delta = 5\gamma_m$ and $\tau = 40/\gamma_m$

The trajectory on the phase space is:

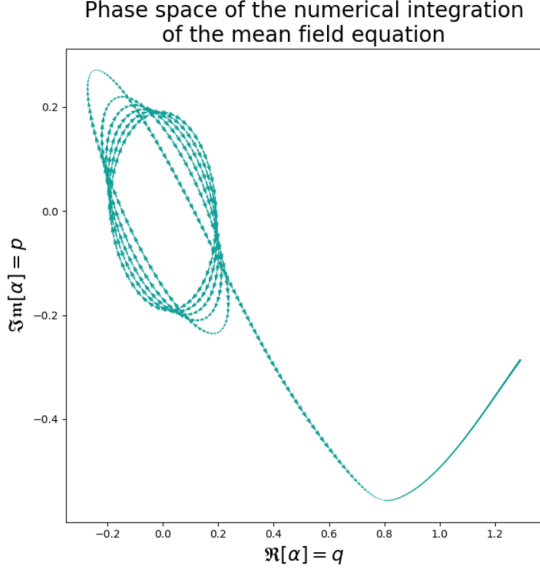


Figure 16: Phase trajectory of the numerical integration of the mean-field equations with $\eta_f = 6\gamma_m$, $\Delta = 5\gamma_m$ and $\tau = 100/\gamma_m$. The picture shows a phase transition between a phase characterized by the presence of oscillations and other with fixed stable points

We observe that the simulation results match the analytical results obtained under the mean-field approximation.

E Mean-field approximation of the Ising model for two oscillators with $\vec{h} = 0$

To begin analysing the behaviour of the system with coupled oscillators, the mean-field equations are studied. The mean-field equations with an Ising-like coupling are:

$$\begin{cases} \dot{\alpha}_l = -i\frac{\Delta}{2}\alpha_l + \eta\beta_l - \alpha_l^4\beta_l^3 + \frac{i\xi_0}{4}\sum_{k=1} J_{l,k}\alpha_k \\ \dot{\beta}_l = i\frac{\Delta}{2}\beta_l + \eta\alpha_l - \alpha_l^3\beta_l^4 - \frac{i\xi_0}{4}\sum_{k=1} J_{l,k}\beta_k \end{cases} \quad (180)$$

Here, the subindex l denotes the l -th oscillator, and all equations have been divided by 2, introducing this factor into the time variable. We now analyse the case of two coupled oscillators for which $J_{i,j} = 1 - \delta_{i,j}$. In this case, the mean-field equations of the coupled system are:

$$\begin{cases} \dot{\alpha}_1 = -i\frac{\Delta}{2}\alpha_1 + \eta\beta_1 - \alpha_1^4\beta_1^3 + \frac{i\xi_0}{4}\alpha_2 \\ \dot{\beta}_1 = i\frac{\Delta}{2}\beta_1 + \eta\alpha_1 - \alpha_1^3\beta_1^4 - \frac{i\xi_0}{4}\beta_2 \\ \dot{\alpha}_2 = -i\frac{\Delta}{2}\alpha_2 + \eta\beta_2 - \alpha_2^4\beta_2^3 + \frac{i\xi_0}{4}\alpha_1 \\ \dot{\beta}_2 = i\frac{\Delta}{2}\beta_2 + \eta\alpha_2 - \alpha_2^3\beta_2^4 - \frac{i\xi_0}{4}\beta_1 \end{cases} \quad (181)$$

The subindex 1 and 2 indicate the oscillator associated with each coherent amplitude. Now, the fixed points of this dynamical system are computed. It is straightforward to verify that one fixed point is the trivial solution $\alpha_i, \beta_i = 0$. Therefore, from now on we focus on non-vanishing solutions. Dividing all the equations by η and defining $b = \frac{\Delta}{\eta}$

and $a = \frac{\xi_0}{\eta}$, we obtain:

$$\left\{ \begin{array}{l} 0 = -i\frac{b}{2}\alpha_1 + \beta_1 - \eta^{-1}\alpha_1^4\beta_1^3 + \frac{ia}{4}\alpha_2 \\ 0 = i\frac{b}{2}\beta_1 + \alpha_1 - \eta^{-1}\alpha_1^3\beta_1^4 - \frac{ia}{4}\beta_2 \\ 0 = -i\frac{b}{2}\alpha_2 + \beta_2 - \eta^{-1}\alpha_2^4\beta_2^3 + \frac{ia}{4}\alpha_1 \\ 0 = i\frac{b}{2}\beta_2 + \alpha_2 - \eta^{-1}\alpha_2^3\beta_2^4 - \frac{ia}{4}\beta_1 \end{array} \right. \quad (182)$$

Now, if the nonlinear terms in the first (multiplied by β_1) and the third equation (multiplied by β_2) are equated to those in the second equation (multiplied by α_1) and the fourth equation (multiplied by α_2), respectively. The system of equations can be rewritten as:

$$\left\{ \begin{array}{l} 0 = ib\beta_1\alpha_1 + \alpha_1^2 - \beta_1^2 - \frac{ia}{4}(\beta_2\alpha_1 + \alpha_2\beta_1) \\ 0 = ib\beta_2\alpha_2 + \alpha_2^2 - \beta_2^2 - \frac{ia}{4}(\beta_2\alpha_1 + \alpha_2\beta_1) \\ 0 = -i\frac{b}{2}\alpha_1 + \beta_1 - \eta^{-1}\alpha_1^4\beta_1^3 + \frac{ia}{4}\alpha_2 \\ 0 = -i\frac{b}{2}\alpha_2 + \beta_2 - \eta^{-1}\alpha_2^4\beta_2^3 + \frac{ia}{4}\alpha_1 \end{array} \right. \quad (183)$$

From the previous results, it is known that after the bifurcation the modulus of the coherent amplitude is the same for all the oscillators. Therefore, we perform the following substitution:

$$\alpha_i = xe^{i\phi_i} \quad \beta_i = xe^{-i\phi_i} \quad (184)$$

This allows the previous system of equations to be rewritten as:

$$\left\{ \begin{array}{l} 0 = b + 2\sin(2\phi_1) - \frac{a}{2}\cos(\phi_1 - \phi_2) \\ 0 = b + 2\sin(2\phi_2) - \frac{a}{2}\cos(\phi_1 - \phi_2) \\ 0 = -i\frac{b}{2}e^{i\phi_1} + e^{-i\phi_1} - \eta^{-1}x^6e^{i\phi_1} + \frac{ia}{4}e^{i\phi_2} \\ 0 = -i\frac{b}{2}e^{i\phi_2} + e^{-i\phi_2} - \eta^{-1}x^6e^{i\phi_2} + \frac{ia}{4}e^{i\phi_1} \end{array} \right. \quad (185)$$

From the first and second equations, it follows that $\phi_1 = \phi_2$ by the equating the terms involving $\cos(\phi_1 - \phi_2)$ in both equations. Using this condition, the common phase ϕ can be determined by solving:

$$0 = b + 2\sin(2\phi) - \frac{a}{2} \longrightarrow \sin(2\phi) = \frac{a}{4} - \frac{b}{2} \quad (186)$$

Now, using the remaining equations, the modulus of the coherent amplitude can be determined:

$$0 = -i\frac{b}{2}e^{i\phi} + e^{-i\phi} - \eta^{-1}x^6e^{i\phi} + \frac{ia}{4}e^{i\phi} \longrightarrow x = \eta^{1/6} \left[1 - \left(\frac{a}{4} - \frac{b}{2} \right)^2 \right]^{1/12} \quad (187)$$

This corresponds to the modulus of the coherent amplitude. Using this result, the position and momentum can be obtained by transforming from polar to Cartesian coordinates:

$$\begin{aligned} q &= \eta^{1/6} \left[1 - \left(\frac{\xi_0}{4\eta} - \frac{\Delta}{2\eta} \right)^2 \right]^{1/12} \cos \left[\frac{1}{2} \arctan \left(\frac{\frac{\xi_0}{4\eta} - \frac{\Delta}{2\eta}}{\sqrt{1 - (\frac{\xi_0}{4\eta} - \frac{\Delta}{2\eta})^2}} \right) \right] \\ p &= \eta^{1/6} \left[1 - \left(\frac{\xi_0}{4\eta} - \frac{\Delta}{2\eta} \right)^2 \right]^{1/12} \sin \left[\frac{1}{2} \arctan \left(\frac{\frac{\xi_0}{4\eta} - \frac{\Delta}{2\eta}}{\sqrt{1 - (\frac{\xi_0}{4\eta} - \frac{\Delta}{2\eta})^2}} \right) \right] \end{aligned} \quad (188)$$

Now, the stability of the origin is analysed through a linear stability analysis of the fixed points. The Jacobian at this point is given by:

$$\begin{pmatrix} \dot{\delta\alpha_1} \\ \dot{\delta\beta_1} \\ \dot{\delta\alpha_2} \\ \dot{\delta\beta_2} \end{pmatrix} = \begin{pmatrix} -\frac{i\Delta}{2} & \eta & \frac{i\xi_0}{4} & 0 \\ \eta & -\frac{i\Delta}{2} & 0 & -\frac{i\xi_0}{4} \\ \frac{i\xi_0}{4} & 0 & -\frac{i\Delta}{2} & \eta \\ 0 & -i\frac{\xi_0}{4} & \eta & \frac{i\Delta}{2} \end{pmatrix} \cdot \begin{pmatrix} \delta\alpha_1 \\ \delta\beta_1 \\ \delta\alpha_2 \\ \delta\beta_2 \end{pmatrix}. \quad (189)$$

The eigenvalues of the matrix are computed to determine the stability of the fixed point, yielding:

$$\begin{aligned} \lambda_1^\pm &= \pm i\eta \sqrt{\left(\frac{a}{4} - \frac{b}{2}\right)^2 - 1} \\ \lambda_2^\pm &= \pm i\eta \sqrt{\left(\frac{a}{4} + \frac{b}{2}\right)^2 - 1} \end{aligned} \quad (190)$$

Thus, this fixed point behaves like a center, giving rise to a phase with oscillations. The stability of the nontrivial solution is also determined:

$$\begin{pmatrix} -4\sqrt{1 - \left(\frac{\xi_0}{4\eta} - \frac{\Delta}{2\eta}\right)^2} - \frac{i\Delta}{2\eta} & 1 - 3\sqrt{1 - \left(\frac{\xi_0}{4\eta} - \frac{\Delta}{2\eta}\right)^2} e^{i\varphi} & \frac{i\xi_0}{4\eta} & 0 \\ 1 - 3\sqrt{1 - \left(\frac{\xi_0}{4\eta} - \frac{\Delta}{2\eta}\right)^2} e^{-i\varphi} & \frac{i\Delta}{2\eta} - 4\sqrt{1 - \left(\frac{\xi_0}{4\eta} - \frac{\Delta}{2\eta}\right)^2} & 0 & -\frac{i\xi_0}{4\eta} \\ \frac{i\xi_0}{4\eta} & 0 & -4\sqrt{1 - \left(\frac{\xi_0}{4\eta} - \frac{\Delta}{2\eta}\right)^2} - \frac{i\Delta}{2\eta} & 1 - 3\sqrt{1 - \left(\frac{\xi_0}{4\eta} - \frac{\Delta}{2\eta}\right)^2} e^{i\varphi} \\ 0 & -\frac{i\xi_0}{4\eta} & 1 - 3\sqrt{1 - \left(\frac{\xi_0}{4\eta} - \frac{\Delta}{2\eta}\right)^2} e^{-i\varphi} & \frac{i\Delta}{2\eta} - 4\sqrt{1 - \left(\frac{\xi_0}{4\eta} - \frac{\Delta}{2\eta}\right)^2} \end{pmatrix}$$

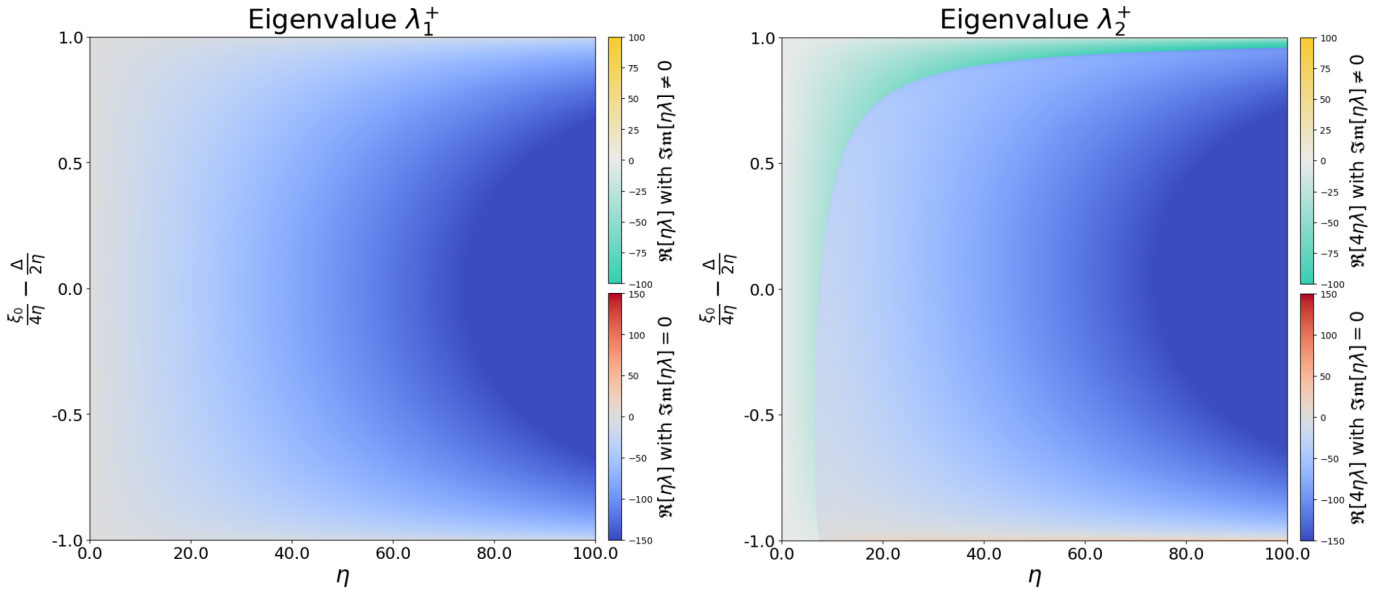
Here, φ denotes:

$$\varphi = \arcsin \left(\frac{\xi_0}{4\eta} - \frac{\Delta}{2\eta} \right) \quad (191)$$

Now, a new parameter, $Q = \frac{\xi_0}{4\eta} - \frac{\Delta}{2\eta}$ is defined. The eigenvalues of the Jacobian are then:

$$\begin{aligned}\lambda_1^\pm &= -4\sqrt{1-Q^2} \pm \sqrt{10(1-Q^2) - 6\cos(\varphi)\sqrt{1-Q^2}} \\ \lambda_2^\pm &= -4\sqrt{1-Q^2} \pm \sqrt{9(1-Q^2) - 6\cos(\varphi)\sqrt{1-Q^2} + (1-(Q+b)^2)}\end{aligned}\quad (192)$$

It is clear that λ_1^- and λ_2^- are negative. Therefore, to assess the stability of the fixed point, it is necessary to examine the sign of the real parts of λ_1^+ and λ_2^+ .



Eigenvalue λ_1^+ as a function of $\frac{\xi_0}{4\eta} - \frac{\Delta}{2\eta}$ and η .

Eigenvalue λ_1^+ as a function of $\frac{\xi_0}{4\eta} - \frac{\Delta}{2\eta}$ and η for $\Delta = 15\gamma_m$.

Table 15: The two eigenvalues are represented using a heat map. The color of the heat map indicates the value of the real part of the eigenvalues, while different color regions distinguish whether the eigenvalues are complex or real. It is observed that both eigenvalues have regions where they are real. However, λ_2^+ exhibits a large area where it is a complex number with negative real part, implying that convergence toward the fixed point in this direction occurs with oscillations. In contrast, λ_1^+ is negative and real for all values, indicating that the fixed point is stable along this direction. The same applies to λ_2^+ , but the convergence toward the fixed point depends on the specific region of the parameter space.

For λ_2^+ , the value of Δ affects the regions where the eigenvalue is complex or real. Larger values of Δ correspond to a larger region where $\lambda_2^+ \in \mathbb{C}$, indicating oscillatory behaviour. Since the eigenvalues have negative real parts, the fixed point remains stable.

The numerical resolution of the equations agree with the analytical result:

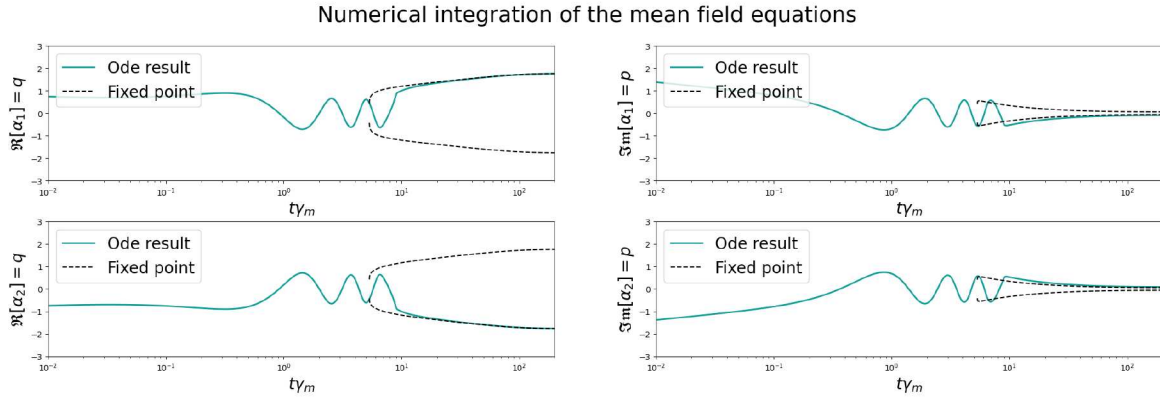
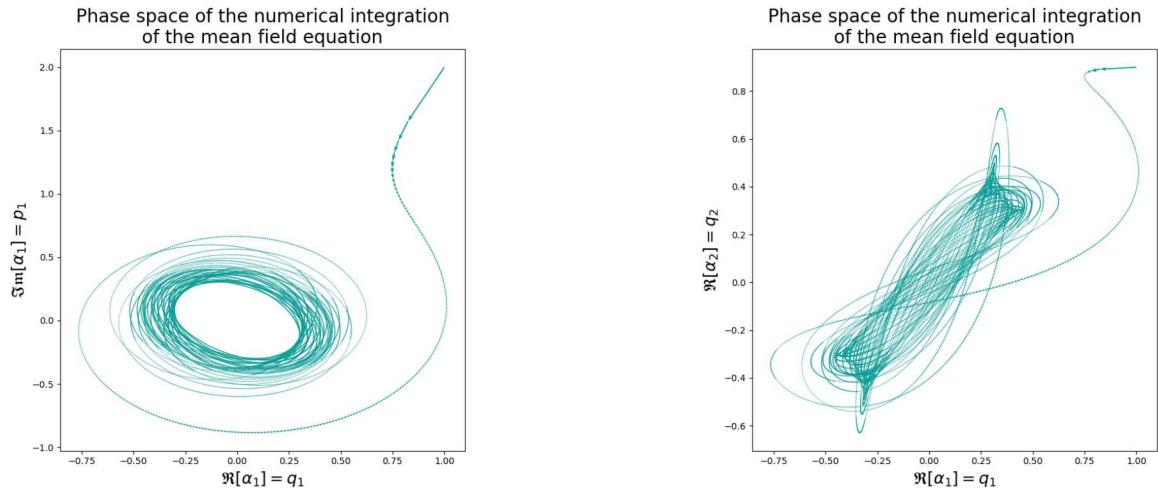


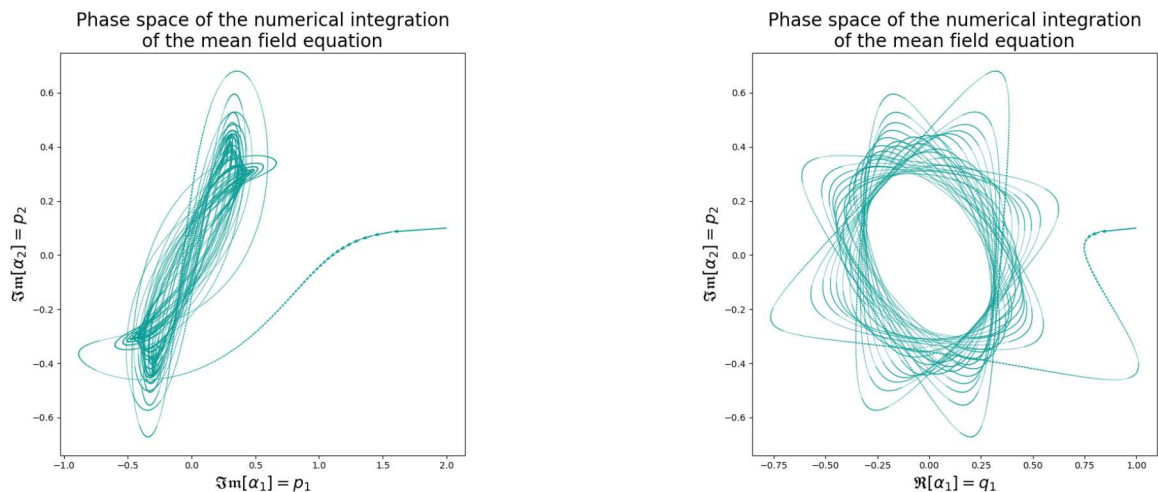
Figure 17: Numerical resolution of the mean-field equations for two coupled oscillators was performed with $\eta_f = 30\gamma_m$, $\Delta = 5\gamma_m$, $\xi_0 = 2\gamma_m$ and $\tau = 80/\gamma_m$. The initial points for the solver were $\alpha_1 = 1 + 2i$, $\alpha_2 = -1 - 2i$

The trajectory in phase space, when $\left| \frac{\xi_0}{4\eta} - \frac{\Delta}{2\eta} \right| \geq 1$, exhibits oscillations, and the dynamic does not settle to a fixed point:



Trajectory followed by the mean-field approximation in the phase space seen from the plane q_1 vs p_1 .

Trajectory followed by the mean-field approximation in the phase space seen from the plane q_2 vs q_1 .



Trajectory followed by the mean-field approximation in the phase space seen from the plane p_2 vs p_1 .

Trajectory followed by the mean-field approximation in the phase space seen from the plane p_2 vs q_1 .

Table 16: Phase-space trajectory of the coupled oscillators with initial conditions $\alpha_1 = 1 + 2i$ and $\alpha_2 = 0.9 + 0.1i$. The integration time was $t_m = 60/\gamma_m$, and the simulation parameters were $\eta_f = 2\gamma_m$, $\Delta = 10\gamma_m$, $\tau = 80/\gamma_m$ and $\xi_0 = 5\gamma_m$.

Following the same procedure, solutions of the form $x_1 = -x_2$ can also be found. The fixed point is:

$$\begin{aligned} q_1 &= \pm \eta^{1/6} \left[1 - \left(\frac{\xi_0}{4\eta} + \frac{\Delta}{2\eta} \right)^2 \right]^{1/12} \cos \left[\frac{1}{2} \arctan \left(\frac{\frac{\xi_0}{4\eta} + \frac{\Delta}{2\eta}}{\sqrt{1 - \left(\frac{\xi_0}{4\eta} + \frac{\Delta}{2\eta} \right)^2}} \right) \right] \\ p_1 &= \mp \eta^{1/6} \left[1 - \left(\frac{\xi_0}{4\eta} + \frac{\Delta}{2\eta} \right)^2 \right]^{1/12} \sin \left[\frac{1}{2} \arctan \left(\frac{\frac{\xi_0}{4\eta} + \frac{\Delta}{2\eta}}{\sqrt{1 - \left(\frac{\xi_0}{4\eta} + \frac{\Delta}{2\eta} \right)^2}} \right) \right] \\ q_2 &= \mp \eta^{1/6} \left[1 - \left(\frac{\xi_0}{4\eta} + \frac{\Delta}{2\eta} \right)^2 \right]^{1/12} \cos \left[\frac{1}{2} \arctan \left(\frac{\frac{\xi_0}{4\eta} + \frac{\Delta}{2\eta}}{\sqrt{1 - \left(\frac{\xi_0}{4\eta} + \frac{\Delta}{2\eta} \right)^2}} \right) \right] \\ p_2 &= \pm \eta^{1/6} \left[1 - \left(\frac{\xi_0}{4\eta} + \frac{\Delta}{2\eta} \right)^2 \right]^{1/12} \sin \left[\frac{1}{2} \arctan \left(\frac{\frac{\xi_0}{4\eta} + \frac{\Delta}{2\eta}}{\sqrt{1 - \left(\frac{\xi_0}{4\eta} + \frac{\Delta}{2\eta} \right)^2}} \right) \right] \end{aligned} \quad (193)$$

This corresponds to the previous solution under the transformation $\xi_0 \rightarrow -\xi_0$. Therefore, the stability analysis is the previous one.

These results have been obtained for the case of two oscillators, but they can be generalized to N_o coupled oscillators under certain conditions. Accordingly, the following system of $2N_o$ equations will be analysed:

$$\begin{cases} \dot{\alpha}_l = -i\frac{\Delta}{2}\alpha_l + \eta\beta_l - \alpha_l^4\beta_l^3 + \frac{i\xi_0}{4}\sum_{k=1}^{N_o} J_{l,k}\alpha_k \\ \dot{\beta}_l = i\frac{\Delta}{2}\beta_l + \eta\alpha_l - \alpha_l^3\beta_l^4 - \frac{i\xi_0}{4}\sum_{k=1}^{N_o} J_{l,k}\beta_k \end{cases} \quad (194)$$

To analyse the dynamic of the model, the fixed points are computed. Thus, the following system of equations is solved:

$$\begin{cases} 0 = -i\frac{\Delta}{2}\alpha_l + \eta\beta_l - \alpha_l^4\beta_l^3 + \frac{i\xi_0}{4}\sum_{k=1}^{N_o} J_{l,k}\alpha_k \\ 0 = i\frac{\Delta}{2}\beta_l + \eta\alpha_l - \alpha_l^3\beta_l^4 - \frac{i\xi_0}{4}\sum_{k=1}^{N_o} J_{l,k}\beta_k \end{cases} \quad (195)$$

Following the same steps as in two-oscillators case, and considering that the coherence amplitude of each oscillator is given by $\alpha_l = x_l e^{i\phi_l}$:

$$\begin{cases} 0 = \Delta x_l^2 + 2\eta x_l^2 \sin(2\phi_l) - \frac{\xi_0}{2} \sum_{k=1}^{N_o} J_{l,k} x_l x_k \cos(\phi_l - \phi_k) \\ 0 = -i\frac{\Delta}{2}x_l e^{i\phi_l} + \eta e^{-i\phi_l} x_l - x_l^7 e^{i\phi_l} + \frac{i\xi_0}{4} \sum_{k=1}^{N_o} J_{l,k} e^{i\phi_k} x_k \end{cases} \quad (196)$$

To solve the system of equations, we again assume that the coherence amplitudes of the lobes are equal, $x_l = x_k = x$. This assumption is motivated by the fact that the coupling term is introduced as a perturbation of the system. Consequently, the coherence amplitude of each oscillator should coincide with that of a single uncoupled oscillator, up to perturbations of order ξ_0 . Neglecting these perturbations, the coherence amplitudes of all the oscillators can

be taken as identical:

$$\begin{cases} 0 = \Delta + 2\eta \sin(2\phi_l) - \frac{\xi_0}{2} \sum_{k=1}^{N_o} J_{l,k} \cos(\phi_l - \phi_k) \\ 0 = -i\frac{\Delta}{2}e^{i\phi_l} + \eta e^{-i\phi_l} - x^6 e^{i\phi_l} + \frac{i\xi_0}{4} \sum_{k=1}^{N_o} J_{l,k} e^{i\phi_k} \end{cases} \quad (197)$$

Another simplifying assumption is that the phases of all oscillators are identical, $\phi_l = \phi_k = \phi$. This approximation holds when the system operates far from the bifurcation point, where the driving strength is sufficiently large to neglect coupling effects. Under this condition, the equations reduce to:

$$\begin{cases} 0 = \Delta + 2\eta \sin(2\phi) - \frac{\xi_0}{2} \sum_{k=1}^{N_o} J_{l,k} \\ 0 = -i\frac{\Delta}{2}e^{i\phi} + \eta e^{-i\phi} - x^6 e^{i\phi} + \frac{i\xi_0}{4} \sum_{k=1}^{N_o} J_{l,k} e^{i\phi} x_k \end{cases} \quad (198)$$

From the first equation, it is possible to obtain the phase of the oscillators:

$$\phi = \frac{1}{2} \arcsin \left(\frac{\Delta}{2\eta} - \frac{\xi_0}{4\eta} \sum_{k=1}^{N_o} J_{l,k} \right) \quad (199)$$

Since the phases of all the oscillators are identical, the following condition is obtained:

$$\phi_l = \phi_n \leftrightarrow \sum_{k=1}^{N_o} J_{l,k} = \sum_{k=1}^{N_o} J_{n,k} \quad (200)$$

Therefore, the solution obtained under the equal-phase assumption is valid in the case where $\sum_{k=1}^{N_o} J_{l,k} = \sum_{k=1}^{N_o} J_{n,k}$ for $\forall l, n$. This corresponds, for example, to the situation in which all the coupling strengths are identical, $J_{i,j} = J$. In this case, a new effective coupling strength can be defined as $\bar{\xi} = \xi_0 \sum_{k=1}^{N_o} J_{l,k}$. Under these assumptions, the problem reduces to the previous case of two oscillators:

$$\begin{aligned} q &= \eta^{1/6} \left[1 - \left(\frac{\bar{\xi}}{4\eta} - \frac{\Delta}{2\eta} \right)^2 \right]^{1/12} \cos \left[\frac{1}{2} \arctan \left(\frac{\frac{\bar{\xi}}{4\eta} - \frac{\Delta}{2\eta}}{\sqrt{1 - \left(\frac{\bar{\xi}}{4\eta} - \frac{\Delta}{2\eta} \right)^2}} \right) \right] \\ p &= \eta^{1/6} \left[1 - \left(\frac{\bar{\xi}}{4\eta} - \frac{\Delta}{2\eta} \right)^2 \right]^{1/12} \sin \left[\frac{1}{2} \arctan \left(\frac{\frac{\bar{\xi}}{4\eta} - \frac{\Delta}{2\eta}}{\sqrt{1 - \left(\frac{\bar{\xi}}{4\eta} - \frac{\Delta}{2\eta} \right)^2}} \right) \right] \end{aligned} \quad (201)$$

Since this case is identical to the previous one but with $\bar{\xi}$ replacing ξ_0 , the stability analysis and the dynamics remain the same as before.

F Parity symmetry for coupled dissipative oscillators

From [2], it is known that the dissipative oscillators exhibits a strong \mathbb{Z}_2 symmetry when they are decoupled. However, the addition of a coupling term $\sum_{i,j} J_{i,j} a_i a_j^\dagger$ breaks the individual symmetry of each oscillator, since $a_i \rightarrow -a_i$ no longer leaves the system invariant. Nevertheless, although the parity symmetry of a single oscillator is broken, the full system still preserves a global parity symmetry involving all oscillators:

$$Z = \otimes_{i=1}^{N_o} Z_2 \quad (202)$$

This parity correspond to the operation acting simultaneously over all the oscillators. As will be shown, it constitute a strong symmetry of the system. From the results of [2], it is clear that Z commutes with all the elements of the Lindbladian in the case of $\xi_0 = 0$. Therefore, It remains to demonstrate that, for $\xi_0 \neq 0$, the operator Z also commutes with the coupling term. The Z_n operator expressed in its natural basis is:

$$Z_2^{(i)} = e^{i\pi a^\dagger a} = \sum_{l=0} e^{-i\pi l} |l\rangle_i \langle l|_i \quad (203)$$

Which represent the parity operator acting over the oscillator i . To verify that Z is indeed a symmetry, I will show that $[H_c, Z] = 0$.

$$\sum_{i,j} J_{i,j} \left[a_i a_j^\dagger, Z \right] = \sum_{i,j} J_{i,j} \left[a_i a_j^\dagger, Z_2^{(i)} \otimes Z_2^{(j)} \right] \otimes_{k \neq i,j}^{N_o} Z_2^k \quad (204)$$

The commutator is analysed now:

$$a_i a_j^\dagger Z_2^{(i)} \otimes Z_2^{(j)} = \sum_{k,l=0} e^{i\pi(l+k)} \sqrt{l(k+1)} |l-1\rangle_i \langle l| \otimes |k+1\rangle_j \langle k|_j \quad (205)$$

$$Z_2^{(i)} \otimes Z_2^{(j)} a_i a_j^\dagger = \sum_{k,l=0} e^{i\pi(l+k)} \sqrt{k(l+1)} |l\rangle_i \langle l+1| \otimes |k\rangle_j \langle k-1|_j \quad (206)$$

Using the fact that k and l are dummy indices in the equation 206, the commutator can be expressed as:

$$\left[a_i a_j^\dagger, Z_2^{(i)} \otimes Z_2^{(j)} \right] = \sum_{l,k=0} e^{i\pi(l+k)} \sqrt{(k+1)l} \left[{}_{k+1}^{l-1}(ij)_k^l - {}_l^k(ij)_{l-1}^{k+1} \right] \quad (207)$$

Here, a more compact notation is used for the sake of readability:

$$|l\rangle_i \langle l+1| \otimes |k\rangle_j \langle k-1|_j = {}_k^l(ij)_{k-1}^{l+1} \quad (208)$$

This result has been obtained for $a_i a_j^\dagger$, but using the fact that the coupling coefficients satisfy $J_{i,j} = J_{j,i}$:

$$\left[a_i a_j^\dagger + a_j a_i^\dagger, Z_2^{(i)} \otimes Z_2^{(j)} \right] = \sum_{l,k=0} e^{i\pi(l+k)} \sqrt{(k+1)l} \left[{}_{k+1}^{l-1}(ij)_k^l - {}_l^k(ij)_{l-1}^{k+1} - {}_{k+1}^{l-1}(ij)_k^l + {}_l^k(ij)_{l-1}^{k+1} \right] = 0 \quad (209)$$

This shows that the commutator between Z_2 and the coupling term vanishes, implying that the system possesses a strong symmetry.

G QUBO

A quadratic unconstrained binary optimization problem or QUBO is a combinatorial optimization problem with binary decision variables. The importance of QUBO lies in the fact that many combinatorial problems arising in science, industry, and computer science can be reformulated as QUBO instances [4, 6, 13]. Consequently, advances in computational and mathematical methods for solving QUBO problems enable progress across a wide range of applications.

Definition: Let \mathbf{Q} be an $N \times N$ matrix and \vec{b} a row vector of \mathbb{R}^N . A QUBO is defined as [12]:

$$\text{maximize/minimize} \sum_{i,j=1}^N Q_{i,j} x_i x_j + \sum_{i=1}^N h_i x_i \quad (210)$$

Here, \vec{x} is a N -dimensional binary vector, with $x_i \in \{0, 1\}$. Thus, any QUBO problem is completely defined by the optimization direction (maximization or minimization), and the pair (\mathbf{Q}, \vec{b}) .

QUBO can also be interpreted from the perspective of graph theory. Let $G = (V, E)$ be a graph with $V \in \{1, 2, \dots, N\}$ and $(i, j) \in E$ if and only if $Q_{i,j} \neq 0$. G is called support graph of Q [12].

Furthermore, there is a close relation between QUBO and the Ising model, as any QUBO can be reformulated as an Ising problem [12]. The Ising model, which describes a magnetic material subject to an external field, has the following energy function:

$$E = \sum_{i,j=1}^N J_{i,j} y_i y_j + \sum_{i=1}^N y_i h_i \quad (211)$$

Where \vec{y} is an N -dimensional binary vector with $y_i \in \{-1, 1\}$. The main difference between QUBO and the Ising model lies in the domain of the variables: QUBO variables take values in $\{0, 1\}$, whereas Ising variables take values in $\{-1, 1\}$. Any combinatorial problem presented in terms of an Ising Hamiltonian is referred as an Ising QUBO.

Since the only difference is the variable domain, an Ising QUBO can be mapped to a standard QUBO through the changes of variables:

$$x_i = \frac{1}{2} (1 + y_i) \quad (212)$$

Applying this transformation yields the equivalent QUBO formulation with:

$$\mathbf{Q} = 4\mathbf{J} \quad b_i = 2h_i - 2 \left(\sum_{i,j=1}^N J_{i,j} + J_{j,i} \right) \quad (213)$$

H Quantum annealing

Quantum annealing is a concept closely related with quantum adiabatic computing 2.1.6, and they are usually introduced together [19, 20, 21, 22]. Quantum annealing can be seen as a relaxation of the strict constraints that define quantum adiabatic computing [20, 22], leading to a heuristic variational quantum algorithm. Therefore, it can be regarded as a more general framework than quantum adiabatic computing. It studies adiabatic and non-adiabatic processes, and scenarios where the dynamics are influenced by noisy environments that induce rapid transitions [20].

The generality of quantum annealing has motivated its application to real-world problems. The most prominent implementations are the D-Wave annealers, which employ superconducting qubits [22]. Nonetheless, the technology remains in an early stages, and no conclusive evidence shows that quantum annealing consistently outperforms classical simulated annealing [22]. In particular, it is still debated whether quantum annealing provides advantage in energy landscapes containing both high and low energy regions [21]. Despite these open questions, D-Wave annealers are the leading platform for exploring industry-relevant applications of quantum annealing. Solving a problem with this approach requires following a specific sequence of steps [22]:

- **Formulation:** Express the problem to be solved as a QUBO instance \mathbf{G} and represent it as a logical graph.
- **Minor-embedding:** Map the logical graph onto the physical hardware.
- **Programming:** Assign values to the parameters and set the coupling strengths between the qubits.
- **Initialization:** As in quantum adiabatic computing, the system is initialized in the ground state of a known Hamiltonian.

- **Annealing:** Evolve the system from the initial to the final Hamiltonian using predefined annealing schedules, with the objective to minimizing the system's energy. This is the stage in which the problem is solved.
- **Read out the solution:** The individual values of the qubits are read and stored, which serve as candidate solution.
- **Resampling:** Since the procedure is heuristic, there is not guarantee that the final state corresponds to the ground state of the model. Therefore, the previous two steps are repeated multiple times to obtain a set of candidate solutions.

These are the steps followed by current D-Wave annealers to solve a problem using quantum annealing. However, since completely isolated system cannot be realized in practice, these annealers are strongly affected by decoherence. As a result, solutions can only be obtained within a few microseconds before being lost due to decoherence [21].

The theoretical background of quantum annealing is similar to that of quantum adiabatic computing [19, 20, 21, 22, 75]. However, the constraints imposed by the adiabatic theorem are difficult to maintain in practice. For example, interaction with an environment can induce fluctuations that takes the system out from of the ground state. Moreover, the time required for adiabatic evolution depends on the energy spectrum, which is generally not known a priori [21, 22]. However, in quantum annealing, these conditions are relaxed: the transition time from H_i to H_f is chosen heuristically, and thus no longer guarantee that the system will remain in the ground state throughout the evolution [22].

Simulated annealing uses classical thermal fluctuations to enable transitions between local energy minima [16]. The annealing schedule is chosen to be sufficiently slow to allow the system to explore all the configurations. During the process, the thermal fluctuations are gradually reduced until the system settles into the global minimum.

Quantum annealing follows the same principle but replaces thermal fluctuations with quantum fluctuations [20, 21, 22]. Quantum fluctuations arising from tunnelling effect allow the system escape from local energy minima, since the probability of finding the system on the other side of a energy barrier is non-zero. These fluctuations are introduced by H_i , which introduces disorder with respect to the eigenstates of H_f . As in the classical scheme, the strength of the fluctuations is gradually reduced, with the expectation that the final state corresponds with to the ground state of H_f [21, 22]. Although a definitive performance advantage of quantum annealing over classical algorithms has not yet been demonstrated, the presence of superposition, entanglement, and tunnelling effects is believed to provide potential improvements [22, 47].

I Eigenvector determination

The adiabatic quantum computer studied here can also be employed to determine eigenvectors. In this approach, the eigenvalue is assumed to be known, and the task is to compute the associated eigenvector. This case is particularly relevant for large matrices where conventional methods become computationally demanding. For instance, the Power method [76] requires iterative updates of the eigenvector approximation until convergence, which can be costly since each iteration involves processing all vector entries. The total number of iterations depends on the spectral properties of the matrix and it may be prohibitively large. Similarly, the Jacobi method [76] applies successive rotations to diagonalize the matrix, but for high-dimensional systems, the required matrix multiplications become computationally intractable.

Conversely, I propose a quantum adiabatic method based on non linear oscillators to compute the eigenvectors of a matrix. This approach does not require multiple iterations to obtain the eigenvalue, nor does it relay on successive matrix multiplications. The method builds up on the previous discussion of solving the Ising model with non linear oscillators, where the spins of the Ising model, s_i , are identified with the creation and annihilation operators $a_i + a_i^\dagger$ [24]:

$$\sum_{i=1}^{N_o} h_i s_i \longrightarrow \sum_{i=1}^{N_o} h_i s_i (a_i + a_i^\dagger) \quad (214)$$

This makes it possible to associate each bit that represents a number with a corresponding oscillator.

Therefore, assume that we have a matrix \mathbf{M} of dimensions $d \times d$, for which one eigenvalue λ is already known. Our goal is to compute the eigenvector \vec{x} associated with this eigenvalue, ($\mathbf{M}\vec{x} = \lambda\vec{x}$). The eigenvector can be expressed as:

$$\vec{x} = \begin{pmatrix} x_1 \\ x_2 \\ \vdots \\ \vdots \\ x_d \end{pmatrix} = x_i \quad (215)$$

Each entry of the vector \vec{x} is encoded in binary numbers on a computer with a precision of q bits:

$$x_i = \sum_{k=1}^q 2^{r-k} b_{i,k} \quad (216)$$

Here, r denotes the number of bits used for the integer part of the number, while the remaining $q - r$ bits correspond to the decimal part. The variable $b_{i,k} \in \{0, 1\}$ represents the k -th bit of the i -th component of the eigenvector \vec{x} . However, the quantum computer provides outcomes for the eigenvectors in terms of $s \in \{-1, 1\}$ rather than $\{0, 1\}$. Consequently, it is necessary to perform the transformation $b_{i,k} \rightarrow s_{i,k}$:

$$b_{i,k} = \frac{1}{2}(1 + s_{i,k}) \quad (217)$$

Accordingly, the i -th component of the vector \vec{x} can be expressed as:

$$x_i = \sum_{k=1}^q 2^{r-k-1} (1 + s_{i,k}) \quad (218)$$

The eigenvalue problem is incorporated into the Hamiltonian, and the corresponding eigenvector is determined via adiabatic computing. To achieve this, it is necessary to encode the solution of the problem as the state that minimizes the total Hamiltonian's energy. In this framework, the ground state of the initial Hamiltonian is adiabatically mapped to the ground state of the final Hamiltonian.

To accomplish this, the eigenvalue problem $\mathbf{M}\vec{x} = \lambda\vec{x}$ must be reformulated as a minimization problem:

$$F(\vec{x}) = (\mathbf{M}\vec{x} - \lambda\vec{x})^\dagger (\mathbf{M}\vec{x} - \lambda\vec{x}) = \lambda^2 \sum_{i=1}^d x_i x_i^* + \sum_{i,j,k=1}^d x_i x_k^* M_{i,j}^\dagger M_{j,k} - \lambda \sum_{i,j=1}^d x_i x_j^* M_{i,j} - \lambda \sum_{i,j=1}^d x_i x_j^* M_{i,j}^\dagger \quad (219)$$

The values that minimize the function $F(\vec{x})$ are those for which $\mathbf{M}\vec{x} - \lambda\vec{x} = 0$, since $F(\vec{x}) \geq 0$. In fact, the problem in this form corresponds to an Ising QUBO problem [12]. The next step is to encode this function into the Hamiltonian, which requires expressing each components of the vector in terms of its binary representation 218.

From this point onward, it is assumed that all the components x_i of the eigenvector are real:

$$\sum_{i=1}^d x_i x_i = \sum_{i=1}^d \sum_{k,l=1}^q 2^{2r-k-l-2} (1 + s_{i,l}) (1 + s_{i,k}) = \sum_{i=1}^d \sum_{k,l=1}^q 2^{2r-k-l-2} (1 + s_{i,l} + s_{i,k} + s_{i,k}s_{i,l}) \quad (220)$$

$$\sum_{i,j=1}^d M_{i,j} x_i x_j = \sum_{i,j=1}^d \sum_{k,l=1}^q 2^{2r-k-l-2} M_{i,j} (1 + s_{i,l}) (1 + s_{i,k}) = \sum_{i,j=1}^d \sum_{k,l=1}^q 2^{2r-k-l-2} M_{i,j} (1 + s_{i,l} + s_{i,k} + s_{i,k}s_{i,l}) \quad (221)$$

$$\sum_{i,j=1}^d M_{i,j}^\dagger x_i x_j = \sum_{i,j=1}^d \sum_{k,l=1}^q 2^{2r-k-l-2} M_{i,j}^\dagger (1 + s_{i,l}) (1 + s_{i,k}) = \sum_{i,j=1}^d \sum_{k,l=1}^q 2^{2r-k-l-2} M_{i,j}^\dagger (1 + s_{i,l} + s_{i,k} + s_{i,k}s_{i,l}) \quad (222)$$

$$\begin{aligned} \sum_{i,j,p=1}^d M_{i,p} M_{p,j}^\dagger x_i x_j &= \sum_{i,j=1}^d \sum_{k,l=1}^q 2^{2r-k-l-2} M_{i,p} M_{p,j}^\dagger (1 + s_{i,l}) (1 + s_{i,k}) = \\ &\quad \sum_{i,j=1}^d \sum_{k,l=1}^q 2^{2r-k-l-2} M_{i,p} M_{p,j}^\dagger (1 + s_{i,l} + s_{i,k} + s_{i,k}s_{i,l}) \end{aligned} \quad (223)$$

However, to incorporate this into the Hamiltonian, the spins s_i must be replaced by the operators $a_i + a_i^\dagger$. The resulting operator is:

$$\lambda^2 \sum_{i=1}^d x_i x_i = \lambda^2 \sum_{i=1}^d \sum_{k,l=1}^q 2^{2r-k-l-2} + 2\lambda^2 \sum_{i=1}^d \sum_{k,l=1}^q 2^{2r-k-l-2} (a_{i,k} + a_{i,k}^\dagger) + \lambda^2 \sum_{i=1}^d \sum_{k,l=1}^q 2^{2r-k-l-2} (a_{i,k} + a_{i,k}^\dagger) (a_{i,l} + a_{i,l}^\dagger) \quad (224)$$

Here, the index i represents the component of the eigenvector, while l denotes the bit used for its representation. Moreover, each of these bits is encoded in a different oscillator; therefore, $a_{i,l}$ represents the annihilation operator of a distinct nonlinear oscillator. The corresponding the commutation relations are:

$$[a_{i,l}, a_{j,k}^\dagger] = \delta_{i,j} \delta_{l,k} \quad [a_{i,l}, a_{j,k}] = 0 \quad (225)$$

The remaining can similarly be represented in operator form:

$$\begin{aligned} \lambda \sum_{i,j=1}^d x_i x_j M_{i,j} &= \lambda \sum_{i,j=1}^d \sum_{k,l=1}^q 2^{2r-k-l-2} M_{i,j} + \lambda \sum_{i,j=1}^d \sum_{k,l=1}^q 2^{2r-k-l-2} M_{i,j} (a_{i,k} + a_{i,k}^\dagger + a_{j,k} + a_{j,k}^\dagger) + \\ &\quad + \lambda \sum_{i,j=1}^d \sum_{k,l=1}^q 2^{2r-k-l-2} M_{i,j} (a_{i,k} + a_{i,k}^\dagger) (a_{j,l} + a_{j,l}^\dagger) \end{aligned} \quad (226)$$

$$\begin{aligned} \lambda \sum_{i,j=1}^d x_i x_j M_{i,j}^\dagger &= \lambda \sum_{i,j=1}^d \sum_{k,l=1}^q 2^{2r-k-l-2} M_{i,j}^\dagger + \lambda \sum_{i,j=1}^d \sum_{k,l=1}^q 2^{2r-k-l-2} M_{i,j}^\dagger (a_{i,k} + a_{i,k}^\dagger + a_{j,k} + a_{j,k}^\dagger) + \\ &\quad + \lambda \sum_{i,j=1}^d \sum_{k,l=1}^q 2^{2r-k-l-2} M_{i,j}^\dagger (a_{i,k} + a_{i,k}^\dagger) (a_{j,l} + a_{j,l}^\dagger) \end{aligned} \quad (227)$$

$$\begin{aligned} \sum_{i,j,p=1}^d x_i x_j M_{i,p} M_{i,p}^\dagger = & \sum_{i,j,p=1}^d \sum_{k,l=1}^q 2^{2r-k-l-2} M_{i,p} M_{i,p}^\dagger + \sum_{i,j,p=1}^d \sum_{k,l=1}^q 2^{2r-k-l-2} M_{i,p} M_{i,p}^\dagger (a_{i,k} + a_{i,k}^\dagger + a_{j,k} + a_{j,k}^\dagger) + \\ & + \sum_{i,j,p=1}^d \sum_{k,l=1}^q 2^{2r-k-l-2} M_{i,p} M_{i,p}^\dagger (a_{i,k} + a_{i,k}^\dagger) (a_{j,l} + a_{j,l}^\dagger) \end{aligned} \quad (228)$$

Accordingly, the Hamiltonian contains three distinct types of terms, classified according to the combinations of annihilation operators they involve:

- **Constant term:**

$$H^{(1)} = \sum_{i,j,p=1}^d \sum_{k,l=1}^q 2^{2r-k-l-2} M_{i,p} M_{i,p}^\dagger - \lambda \sum_{i,j=1}^d \sum_{k,l=1}^q 2^{2r-k-l-2} M_{i,j}^\dagger - \lambda \sum_{i,j=1}^d \sum_{k,l=1}^q 2^{2r-k-l-2} M_{i,j} + \lambda^2 \sum_{i=1}^d \sum_{k,l=1}^q 2^{2r-k-l-2} \quad (229)$$

- **Non-interacting term:**

$$\begin{aligned} H^{(2)} = & \sum_{i,j,p=1}^d \sum_{k,l=1}^q 2^{2r-k-l-2} M_{i,p} M_{i,p}^\dagger (a_{i,k} + a_{i,k}^\dagger + a_{j,k} + a_{j,k}^\dagger) + \\ & - \lambda \sum_{i,j=1}^d \sum_{k,l=1}^q 2^{2r-k-l-2} M_{i,j}^\dagger (a_{i,k} + a_{i,k}^\dagger + a_{j,k} + a_{j,k}^\dagger) - \lambda \sum_{i,j=1}^d \sum_{k,l=1}^q 2^{2r-k-l-2} M_{i,j} (a_{i,k} + a_{i,k}^\dagger + a_{j,k} + a_{j,k}^\dagger) + \\ & + \lambda^2 \sum_{i=1}^d \sum_{k,l=1}^q 2^{2r-k-l-2} (a_{i,k} + a_{i,k}^\dagger) \end{aligned} \quad (230)$$

- **Interacting term:**

$$\begin{aligned} H^{(3)} = & \sum_{i,j,p=1}^d \sum_{k,l=1}^q 2^{2r-k-l-2} M_{i,p} M_{i,p}^\dagger (a_{i,k} + a_{i,k}^\dagger) (a_{j,l} + a_{j,l}^\dagger) + \\ & - \lambda \sum_{i,j=1}^d \sum_{k,l=1}^q 2^{2r-k-l-2} M_{i,j}^\dagger (a_{i,k} + a_{i,k}^\dagger) (a_{j,l} + a_{j,l}^\dagger) - \lambda \sum_{i,j=1}^d \sum_{k,l=1}^q 2^{2r-k-l-2} M_{i,j} (a_{i,k} + a_{i,k}^\dagger) (a_{j,l} + a_{j,l}^\dagger) + \\ & + \lambda^2 \sum_{i=1}^d \sum_{k,l=1}^q 2^{2r-k-l-2} (a_{i,k} + a_{i,k}^\dagger) (a_{i,l} + a_{i,l}^\dagger) \end{aligned} \quad (231)$$

Since the Hamiltonian contains terms proportional to a , it no longer exhibit a symmetry under transformation $a \rightarrow -a$. As consequence, the solution is no longer a cat state. Instead, it reduces to a tensor product of coherent states:

$$|\psi\rangle = \otimes_{i=1}^{N_o} |s_i f(t)\rangle \quad (232)$$

Here, N_o denotes the total number of oscillators used in the computation. Since q bits are assigned to each of the d entries of the eigenvector, it follows that $N_o = qd$. Moreover, because the system is governed by a time-dependent Hamiltonian, the phase of the coherent state is determined function $f(t)$, as it has been the case for the KPO oscillators [1] and dissipative oscillator. As in the case of the Ising model, these Hamiltonians are incorporated into the total Hamiltonian as a perturbation of the original one Hamiltonian:

$$H = \sum_{i=0}^{N_o} H_i + \xi_0 \left(\alpha(t) H^{(1)} + \beta(t) H^{(2)} + \gamma(t) H^{(3)} \right) \quad (233)$$

Here, ξ_0 is a proportionality constant with units of energy, and the functions $\alpha(t)$, $\beta(t)$ and $\gamma(t)$ are introduced to ensure that, once the system surpasses the bifurcation, the expected value of the perturbation corresponds to the equation 219, which provides the correction to the ground-state energy. To determine these functions, the expectation value of the perturbation with respect to the state in equation 232 is evaluated:

$$\langle \psi | H^{(1)} | \psi \rangle = \sum_{i,j,p=1}^d \sum_{k,l=1}^q 2^{2r-k-l-2} M_{i,p} M_{i,p}^\dagger - \lambda \sum_{i,j=1}^d \sum_{k,l=1}^q 2^{2r-k-l-2} M_{i,j}^\dagger - \lambda \sum_{i,j=1}^d \sum_{k,l=1}^q 2^{2r-k-l-2} M_{i,j} + \lambda^2 \sum_{i=1}^d \sum_{k,l=1}^q 2^{2r-k-l-2} \quad (234)$$

$$\begin{aligned} \langle \psi | H^{(2)} | \psi \rangle &= f(t) \sum_{i,j,p=1}^d \sum_{k,l=1}^q 2^{2r-k-l-2} M_{i,p} M_{i,p}^\dagger \left(s_{i,k} + s_{i,k}^\dagger + s_{j,k} + s_{j,k}^\dagger \right) + \\ &- \lambda f(t) \sum_{i,j=1}^d \sum_{k,l=1}^q 2^{2r-k-l-2} M_{i,j}^\dagger \left(s_{i,k} + s_{i,k}^\dagger + s_{j,k} + s_{j,k}^\dagger \right) - \lambda f(t) \sum_{i,j=1}^d \sum_{k,l=1}^q 2^{2r-k-l-2} M_{i,j} \left(s_{i,k} + s_{i,k}^\dagger + s_{j,k} + s_{j,k}^\dagger \right) + \\ &+ \lambda^2 f(t) \sum_{i=1}^d \sum_{k,l=1}^q 2^{2r-k-l-2} \left(s_{i,k} + s_{i,k}^\dagger \right) \end{aligned} \quad (235)$$

$$\begin{aligned} \langle \psi | H^{(3)} | \psi \rangle &= f^2(t) \sum_{i,j,p=1}^d \sum_{k,l=1}^q 2^{2r-k-l-2} M_{i,p} M_{i,p}^\dagger \left(s_{i,k} + s_{i,k}^\dagger \right) \left(s_{j,l} + s_{j,l}^\dagger \right) + \\ &- \lambda f^2(t) \sum_{i,j=1}^d \sum_{k,l=1}^q 2^{2r-k-l-2} M_{i,j}^\dagger \left(s_{i,k} + s_{i,k}^\dagger \right) \left(s_{j,l} + s_{j,l}^\dagger \right) - \lambda f^2(t) \sum_{i,j=1}^d \sum_{k,l=1}^q 2^{2r-k-l-2} M_{i,j} \left(s_{i,k} + s_{i,k}^\dagger \right) \left(s_{j,l} + s_{j,l}^\dagger \right) + \\ &+ \lambda^2 f^2(t) \sum_{i=1}^d \sum_{k,l=1}^q 2^{2r-k-l-2} \left(s_{i,k} + s_{i,k}^\dagger \right) \left(s_{i,l} + s_{i,l}^\dagger \right) \end{aligned} \quad (236)$$

It can be simplified to:

$$\langle \psi | H^{(1)} | \psi \rangle = \sum_{i,j,p=1}^d \sum_{k,l=1}^q 2^{2r-k-l-2} \left(M_{i,p} M_{i,p}^\dagger - \lambda M_{i,j} - \lambda M_{i,j}^\dagger + \lambda^2 \delta_{i,j} \right) \quad (237)$$

$$\langle \psi | H^{(2)} | \psi \rangle = 2f(t) \sum_{i,j,p=1}^d \sum_{k,l=1}^q 2^{2r-k-l-2} (s_{i,k} + s_{j,l}) \left(M_{i,p} M_{i,p}^\dagger - \lambda M_{i,j} - \lambda M_{i,j}^\dagger + \lambda^2 \delta_{i,j} \right) \quad (238)$$

$$\langle \psi | H^{(3)} | \psi \rangle = 4f^2(t) \sum_{i,j,p=1}^d \sum_{k,l=1}^q 2^{2r-k-l-2} s_{i,l} s_{j,k} \left(M_{i,p} M_{i,p}^\dagger - \lambda M_{i,j} - \lambda M_{i,j}^\dagger + \lambda^2 \delta_{i,j} \right) \quad (239)$$

Now, let $Q_{i,j,p} = M_{i,p} M_{i,p}^\dagger - \lambda M_{i,j} - \lambda M_{i,j}^\dagger + \lambda^2 \delta_{i,j}$, which allow us to express the expectation value of the perturbation as:

$$\langle H \rangle_\psi = \alpha(t) \sum_{i,j,p=1}^d \sum_{k,l=1}^q 2^{2r-k-l-2} Q_{i,j,p} + 2f(t)\beta(t) \sum_{i,j,p=1}^d \sum_{k,l=1}^q 2^{2r-k-l-2} Q_{i,j,p} (s_{i,k} + s_{j,l}) + 4f^2(t)\gamma(t) \sum_{i,j,p=1}^d \sum_{k,l=1}^q 2^{2r-k-l-2} s_{i,l} s_{j,k} Q_{i,j,p} \quad (240)$$

Conversely, the eigenvector is determined from the following equation:

$$\sum_{i,j,p=1}^d \sum_{k,l=1}^q 2^{2r-k-l-2} Q_{i,j,p} + \sum_{i,j,p=1}^d \sum_{k,l=1}^q 2^{2r-k-l-2} Q_{i,j,p} (s_{i,k} + s_{j,l}) + \sum_{i,j,p=1}^d \sum_{k,l=1}^q 2^{2r-k-l-2} s_{i,l} s_{j,k} Q_{i,j,p} \quad (241)$$

As can be observed, the result of the perturbation differs from the actual equation used to determine the eigenvector. Therefore, in order to recover 241 from 240, it is necessary to isolate the coefficients multiplying the summations. The non-interacting and interacting terms each contain two multiplicative constants and a power of the function $f(t)$, which do not appear in 241. Consequently, these factors must be canceled by $\beta(t)$ and $\gamma(t)$ to correctly extract the multiplicative factor of each summation. Thus, the requirement for $\alpha(t)$, $\beta(t)$ and $\gamma(t)$ is:

$$\alpha(t) = 2\beta(t)f(t) = 4\gamma(t)f^2(t) \text{ far from the bifurcation} \quad (242)$$

These functions will differ depending on the type of oscillator used in the computation:

- **KPO:** Since $f(t) = \sqrt{\frac{p(t)-\Delta}{K}} \approx \sqrt{\frac{p}{K}}$, the functions are chosen as:

$$\begin{aligned} \alpha(t) &= \frac{p(t)-\Delta \tanh(p(t)/\Delta)}{K} \\ \beta(t) &= \frac{1}{2} \sqrt{\frac{p(t)-\Delta \tanh(p(t)/\Delta)}{K}} \\ \gamma(t) &= \frac{1}{4} \end{aligned} \quad (243)$$

These functions are selected so that, for $p \sim \Delta$, all terms in the equation remain of comparable order. In the limit $p \gg \Delta$, the hyperbolic tangent term can be neglected, leading to:

$$\text{For } p \gg \Delta \quad \begin{cases} \alpha(t) \approx \frac{p(t)}{K} = f^2(t) \\ \beta(t) \approx \frac{1}{2} \sqrt{\frac{p(t)}{K}} = \frac{1}{2} f(t) \\ \gamma(t) \approx \frac{1}{4} \end{cases} \quad (244)$$

Accordingly, for $p \gg \Delta$, the expected value becomes:

$$\langle H \rangle_\psi = f^2(t) \left[\sum_{i,j,p=1}^d \sum_{k,l=1}^q 2^{2r-k-l-2} Q_{i,j,p} (1 + s_{i,k} + s_{j,l} + s_{i,l} s_{j,k}) \right] \quad (245)$$

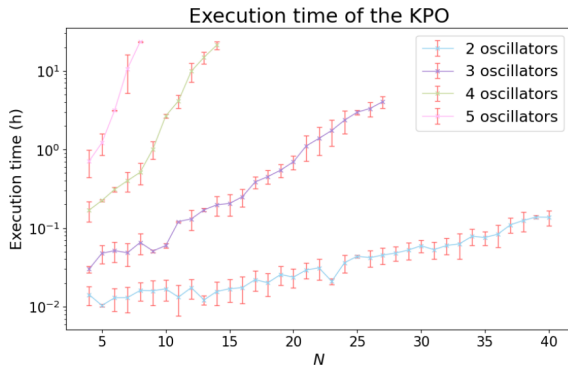
Thus, the expectation value is proportional to the eigenvalue problem.

- **Dissipative oscillators:** Following the same approach as for the KPO oscillator, the coherent amplitude is now given by $f(t) = \left(\frac{\eta(t)}{\gamma_m} \right)^{1/6}$:

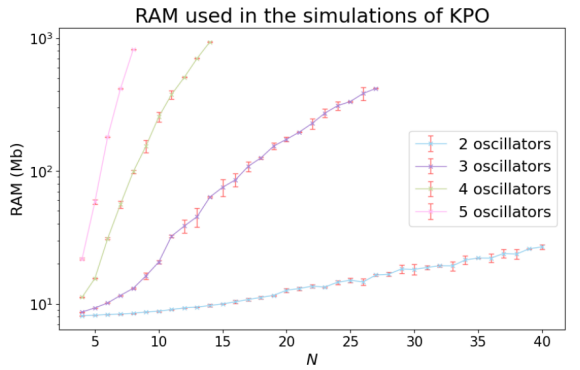
$$\text{For } \eta \gg \Delta \quad \begin{cases} \alpha(t) \approx \left(\frac{\eta(t)}{\gamma_m}\right)^{1/3} = f^2(t) \\ \beta(t) \approx \frac{1}{2} \left(\frac{\eta(t)}{\gamma_m}\right)^{1/6} = \frac{1}{2}f(t) \\ \gamma(t) \approx \frac{1}{4} \end{cases} \quad (246)$$

J Computational resources

An analysis of the computational resources required for simulating of both oscillators is performed. To this end, simulations are carried out for different numbers of coupled oscillators and various cutoff values, for which the simulation time and the memory required for the simulation in each case is computed:

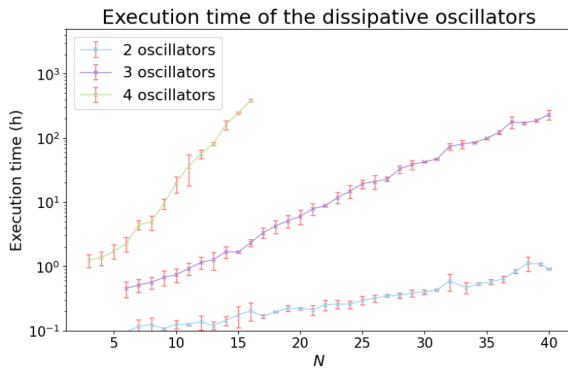


Simulation time for KPO oscillators as a function of the cutoff N for different numbers of coupled oscillators.

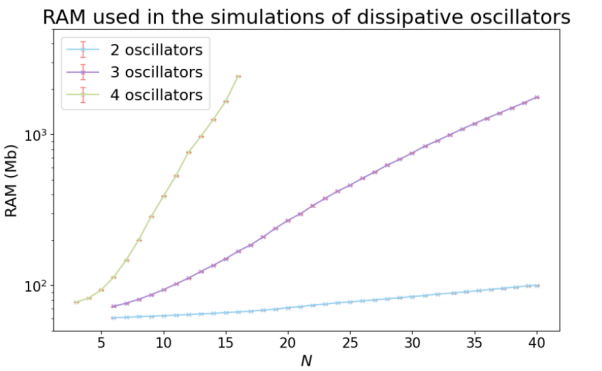


Required RAM for simulating KPO oscillators as a function of the cutoff N for different numbers of coupled oscillators.

Table 17: Time and computational resources required to simulate a coupled system of KPO oscillators using the Adams method. The simulations were performed with the following parameters, with 3 CPU cores assigned to each simulation to improve the computational speed: $p(0) = 0$, $p(700/K) = 5.0K$ and $\xi_0 = 0.5K$. The value of Δ was chosen according to the criteria introduced in 2.2.



Simulation time for dissipative oscillators as a function of the cutoff N for different numbers of coupled oscillators.



Required RAM for simulating dissipative oscillators as a function of the cutoff N for different numbers of coupled oscillators.

Table 18: Time and computational resources required to simulate a coupled system of dissipative oscillators using the quantum jump trajectory method. For each simulation, 20 CPU cores were assigned to improve the computational speed. The simulation parameters are $\tau = 300/\gamma_m$, $\eta(0) = 0$, $\eta(1000/\gamma_m) = 2000\gamma_m$ and $\xi_0 = 300\gamma_m$. The value of Δ was selected according to the criteria introduced in 2.3. The first plot shows the time required to simulate the system with 100 trajectories, while the second plot shows the RAM required for the simulation of a single trajectory.

All the simulations were executed on the Nuredduna cluster from the IFISC. This cluster uses CPU-intensive nodes equipped with AMD EPYC processors (models 7402, 7282 and 9754) and Intel Xeon E5-2630 processors. All simulations were performed for the case of solving the Ising model without an external field.

Overall, the plots show that for large values of the cutoff, both the simulation time and the memory usage increase linearly in the logarithmic space. Consequently, the computational resources required grow exponentially with the size of the Hilbert space. This behaviour is characteristic of quantum systems simulations and imposes significant limitations on their scalability.

In general, the plots show that the computational time and resources required for simulations were lower for KPO oscillators compared to dissipative oscillators. This is expected, as the KPO oscillator simulations were performed for closed systems, allowing the results to be obtained directly by solving the Schrödinger equation once. In contrast, the dissipative oscillators simulations were performed for an open quantum system by unravelling the master equation. To recover results predicted by the Lindblad equation, an average over 100 independent trajectories was required. Additionally, because the dissipative oscillators exhibit stronger non linearity, a large value for the cutoff is needed to obtain physically meaningful results. Consequently, the computational resources required for simulating KPO oscillators were lower than those needed for dissipative oscillators.

The plots shows that simulations with more than three coupled dissipative oscillators becomes computationally prohibited. To obtain physically meaningful results, the cutoff for the Hilbert space must be at least 30, which is feasible for three or fewer coupled oscillators. However, the plots indicate than the required simulation time for four coupled oscillators increases much faster than for three. Using the execution times obtained for the simulations with cutoffs in the range $N \in [4, 16]$, the required time for a cutoff of $N = 30$ with four coupled oscillators can be estimated by fitting the results to a function of the form $\ln(\text{TIME}) = aN + \ln b$:

Coefficients	
a	0.916 ± 0.063
b (h)	0.0151 ± 0.0059

Table 19: Coefficients of the fit for the execution time of the dissipative oscillators. The correlation coefficient is $r^2 = 0.992$, supporting the validity of the assumed linear dependence.

For a cutoff of $N = 30$, the estimated simulation time is 13900 ± 2700 h, or 570 ± 110 days, representing an extremely high computational cost. Therefore, in this work, simulations with dissipative oscillators are restricted to $N = 30$ and three oscillators.

In contrast, for KPO oscillators, simulations were performed up to four coupled oscillators. This is because the cutoff value at which the results becomes independent of N is $N = 14$, and simulations with five coupled oscillators at this cutoff are excessively demanding. To illustrate this, simulations with five coupled oscillators were performed up to a cutoff of $N = 8$. Given the observed linear relationship in the logarithmic scale, these results can be used to estimate the required time for higher cutoff values by fitting a function of the form $\ln(\text{TIME}/\text{MEMORY}) = aN + \ln b$ using least squares. The coefficients obtained from this fit are:

Coefficients for the execution time ($r^2 = 0.995$)		Coefficients for the memory requirements ($r^2 = 0.996$)	
a	0.916 ± 0.063	a	0.921 ± 0.049
b (h)	0.0151 ± 0.0059	b (RAM)	0.60 ± 0.18

Table 20: Coefficients of the fit for the execution time and memory requirements of the KPO oscillators.

From these results, it can be seen that for a cutoff of $N = 11$, the RAM required for the simulation is 14.72 ± 0.13 Gb and the simulation time is 350 ± 150 h, which is already demanding. For $N = 14$, the cutoff at which the results becomes physically meaningful, the estimated simulation time increases to 5613 ± 2500 h, with a RAM requirement of 233.0 ± 2.0 Gb, representing an extremely high computational cost. Consequently, the maximum number of coupled oscillators considered in this work are four.

K Wigner Picture

In quantum mechanics, the Schrodinger picture is typically used to study a quantum system. In this picture, a quantum state is represented by a vector $|\psi\rangle \in \mathcal{H}$, referred as the wave function. Observables are represented by operators $A \in B(\mathcal{H})$ acting on \mathcal{H} . This description contrasts significantly with that of classical mechanics. In classical mechanics, a state is represented by a point in phase space, and its time evolution by a function. So, the observables are functions defined on the phase space in classical mechanics.

Despite the widespread use of the Schrodinger picture in quantum mechanics, it can be very challenging. Since the observables are given in terms of operators, they may not commute $[A, B] \neq 0$, and this can complicate the calculation. In contrast, this does not happen in classical mechanics, where observables are just functions that return a number or vector. This difference makes it worthwhile to explore an alternative approach to studying quantum mechanics using functions. This is the Wigner's picture motivation.

Wigner's picture aims to introduce quantum corrections to classical statistical mechanics while respecting the limits imposed by the Heisenberg uncertainty principle. This is accomplished by the Weyl transform, which enabled the transition from the wave function picture to phase space [77, 78, 79, 80]. More specifically, the Weyl transform associates a function on phase space with each operator. In this picture, the classical probability distribution is generalized to incorporate quantum corrections, resulting in the Wigner function. Furthermore, this function can be understood as the equivalent matrix density counterpart over the phase space.

K.1 Weyl transform

As discussed in [79], given a Hilbert space \mathcal{H} with a hermitian operator A , an orthonormal basis of eigenvectors of A ($\{|\phi_n\rangle\}_{n=0}^\infty$) is chosen. If the system's state is $|\psi\rangle$, the expected value of A is given by:

$$\langle A \rangle(t) = \langle \psi(t) | A | \psi(t) \rangle = \int dx \langle \psi | x \rangle \langle x | A | \psi \rangle \quad (247)$$

Now, the state $|\psi\rangle$ can be expanded in terms of the chosen basis and utilize the fact that these are eigenvectors of A :

$$\langle x | A | \psi \rangle = \sum_{n=0}^{\infty} \langle x | A | \phi_n \rangle \langle \phi_n | \psi \rangle = \int dx' \sum_{n=0}^{\infty} a_n \langle x | \phi_n \rangle \langle \phi_n | x' \rangle \langle x' | \psi \rangle = \int dx' \alpha(x, x') \psi(x') \quad (248)$$

Here, $\alpha(x, x')$ is defined as $\alpha(x, x') = \sum_{n=0}^{\infty} a_n \phi_n(x) \phi_n^*(x')$. Consequently, the final result:

$$\langle A \rangle = \int dx \int dx' \alpha(x, x') \psi(x') \psi^*(x) = \int dx \int dx' \alpha(x, x') \rho(x, x') = \text{Tr}(A\rho) \quad (249)$$

Here $\rho(x, x') = \langle x | \psi \rangle \langle \psi | x' \rangle$ has been defined, where $\rho = |\psi\rangle \langle \psi|$. In contrast, in classical mechanic, the expected value of a function A over phase space is given by:

$$\langle A \rangle = \int dx \int dp A(x, p) f(x, p) \quad (250)$$

Here, $f(x, p)$ is the probability distribution of the trajectories, and $A(x, p)$ is a function defined over the phase space. This expression is quite similar to 249. In fact, they may coincide if one of the spatial integrals is replaced with a momentum integral, and the operators are replaced by their corresponding functions. In this case, the resulting function would represent the operator A in phase space.

Therefore, a connection between these equations will be established. According the postulates of quantum mechanic [81], each dynamical variable can be replaced by its hermitian operator representation. Taking this into account, the Weyl transform is defined as:

$$A(x, p) = \mathcal{W}[A] = \frac{1}{2\pi} \int ds dq \text{Tr} \left(A e^{i(sx+qp)} \right) e^{-i(s\hat{x}+q\hat{p})} \quad (251)$$

The proof of this expression can be found in [79]. Finally, this expression can be rewritten as follows:

$$A(x, p) = \mathcal{W}[A] = \int dy e^{-ipy/2} \langle x + y/2 | A | x - y/2 \rangle \quad (252)$$

This relationship enables the determination of the function associated with a given operator in phase space.

L Rotation Frame

A change of frame can be understood as the absorption of an unitary transformation $U(t)$ into the quantum state $|\psi(t)\rangle$ [82]. Therefore, the relation between the initial and the final vector is:

$$|\psi_R(t)\rangle = U(t) |\psi(t)\rangle \quad (253)$$

In this framework, the system's Hamiltonian must be rewritten to yield a Schrödinger equation for the evolution of the state:

$$i \frac{d}{dt} |\psi_R(t)\rangle = H_R |\psi_R(t)\rangle \quad H_R = UHU^\dagger + i\dot{U}U^\dagger \quad (254)$$

Since the unitary transformation is time-dependent, it introduces a new term in the Hamiltonian. This additional term causes that the expected value of an operator to not longer exhibit a sandwich structure:

$$\langle \psi_R | H_R | \psi_R \rangle = \langle \psi | H + iU^\dagger \dot{U} | \psi \rangle \quad (255)$$

The aim of this framework is to extract the rotating component of the system, this idea has an analogous in classical mechanics. Consider a classical system undergoing circular motion of frequency ω in the laboratory frame. The angular dependence of this system can be removed by changing to a rotation frame. This correspond to a framework that is rotating with the system, where the rotation motion effectively disappear. This transformation simplify the equations but introduces new terms such as the centrifugal force $F = mv^2/r$. These additional terms are the classical analogous to the new component of the expected value $iU^\dagger \dot{U}$, which accounts for the necessary adjustment of the Hamiltonian to maintain the same dynamics as before.

References

- [1] Hayato Goto. "Bifurcation-based adiabatic quantum computation with a nonlinear oscillator network". en. *Sci. Rep.* **6** (2016), pages 1–8.
- [2] Adrià Labay-Mora, Roberta Zambrini, and Gian Luca Giorgi. "Quantum memories for squeezed and coherent superpositions in a driven-dissipative nonlinear oscillator". *Physical Review A* **109** (2024), page 032407.
- [3] Alexander Schrijver. *Combinatorial Optimization: Polyhedra and Efficiency*. en. 2003rd edition. Berlin, Germany: Springer, 2002.
- [4] Fred Glover, Gary Kochenberger, and Yu Du. *A Tutorial on Formulating and Using QUBO Models*. 2019.
- [5] Maryam Karimi-Mamaghan, Mehrdad Mohammadi, Patrick Meyer, Amir Mohammad Karimi-Mamaghan, and El-Ghazali Talbi. "Machine learning at the service of meta-heuristics for solving combinatorial optimization problems: A state-of-the-art". *European Journal of Operational Research* **296** (2022), pages 393–422. DOI: <https://doi.org/10.1016/j.ejor.2021.04.032>.
- [6] Prasanna Date, Robert Patton, Catherine Schuman, and Thomas Potok. "Efficiently embedding QUBO problems on adiabatic quantum computers". *Quantum Information Processing* **18** (2019), page 117.
- [7] Sanjoy K Baruah, Marko Bertogna, and Giorgio C Buttazzo. *Multiprocessor scheduling for real time systems*. en. 2015th edition. Cham, Switzerland: Springer International Publishing, 2015.
- [8] Ernesto Bonomi and Jean-Luc Lutton. "The N-City Travelling Salesman Problem: Statistical Mechanics and the Metropolis Algorithm". *SIAM Review* **26** (1984), pages 551–568. DOI: <10.1137/1026105>.
- [9] Ken A. Dill and Justin L. MacCallum. "The Protein-Folding Problem, 50 Years On". *Science* **338** (2012), pages 1042–1046. DOI: <10.1126/science.1219021>.
- [10] Maximilian M Etschmaier and Dennis F X Mathaisel. "Airline scheduling: An overview". en. *Transp. Sci.* **19** (1985), pages 127–138.
- [11] Yun Li, Cristen Willer, Serena Sanna, and Gonçalo Abecasis. "Genotype imputation". en. *Annu. Rev. Genomics Hum. Genet.* **10** (2009), pages 387–406.
- [12] Abraham P Punnen. "The quadratic unconstrained binary optimization problem". *Springer International Publishing* **10** (2022), pages 978–3.
- [13] Andrew Lucas. "Ising formulations of many NP problems". *Frontiers in Physics* **2** (2014). DOI: <10.3389/fphy.2014.00005>.
- [14] Sanjoy Dasgupta. *The hardness of k-means clustering*. en. <https://escholarship.org/uc/item/2qm3k10c>. Accessed: 2025-8-29. 2008.
- [15] Nello Cristianini and Bernhard Scholkopf. "Support Vector Machines and Kernel Methods: The New Generation of Learning Machines". *AI Magazine* **23** (2002), page 31. DOI: <10.1609/aimag.v23i3.1655>.
- [16] Scott Kirkpatrick, C Daniel Gelatt Jr, and Mario P Vecchi. "Optimization by simulated annealing". *science* **220** (1983), pages 671–680.
- [17] Jon Kleinberg and Éva Tardos. *Algorithm Design*. https://cs.slu.edu/~goldwamh/class/slu/csci314/2006_Spring/handouts/course-info.pdf. Pearson Education India, 2006.
- [18] Sanjeev Arora and Boaz Barak. *Computational Complexity: A Modern Approach*. Cambridge University Press, 2009.
- [19] Satoshi Morita and Hidetoshi Nishimori. "Mathematical foundation of quantum annealing". *Journal of Mathematical Physics* **49** (2008).
- [20] Philipp Hauke, Helmut G Katzgraber, Wolfgang Lechner, Hidetoshi Nishimori, and William D Oliver. "Perspectives of quantum annealing: Methods and implementations". *Reports on Progress in Physics* **83** (2020), page 054401.
- [21] Atanu Rajak, Sei Suzuki, Amit Dutta, and Bikas K Chakrabarti. "Quantum annealing: An overview". *Philosophical Transactions of the Royal Society A* **381** (2023), page 20210417.
- [22] Sheir Yarkoni, Elena Raponi, Thomas Bäck, and Sebastian Schmitt. "Quantum annealing for industry applications: Introduction and review". *Reports on Progress in Physics* **85** (2022), page 104001.
- [23] Mark Dykman. *Fluctuating nonlinear oscillators: from nanomechanics to quantum superconducting circuits*. Oxford University Press, 2012.
- [24] Hayato Goto, Zhirong Lin, and Yasunobu Nakamura. "Dissipative quantum bifurcation machine: quantum heating of coupled nonlinear oscillators". *arXiv preprint arXiv:1707.00986* (2017).
- [25] Zaki Leghtas, Steven Touzard, Ioan M Pop, Angela Kou, Brian Vlastakis, Andrei Petrenko, Katrina M Sliwa, Anirudh Narla, Shyam Shankar, Michael J Hatridge, et al. "Confining the state of light to a quantum manifold by engineered two-photon loss". *Science* **347** (2015), pages 853–857.
- [26] Brian Vlastakis, Gerhard Kirchmair, Zaki Leghtas, Simon E Nigg, Luigi Frunzio, Steven M Girvin, Mazyar Mirrahimi, Michel H Devoret, and Robert J Schoelkopf. "Deterministically encoding quantum information using 100-photon Schrödinger cat states". *Science* **342** (2013), pages 607–610.

- [27] Gerhard Kirchmair, Brian Vlastakis, Zaki Leghtas, Simon E Nigg, Hanhee Paik, Eran Ginossar, Mazyar Mirrahimi, Luigi Frunzio, Steven M Girvin, and Robert J Schoelkopf. “Observation of quantum state collapse and revival due to the single-photon Kerr effect”. *Nature* **495** (2013), pages 205–209.
- [28] M Rehák, P Neilinger, M Grajcar, G Oelsner, U Hübner, E Il'ichev, and H-G Meyer. “Parametric amplification by coupled flux qubits”. *Applied Physics Letters* **104** (2014).
- [29] ZR Lin, Kunihiro Inomata, K Koshino, WD Oliver, Yasunobu Nakamura, Jaw-Shen Tsai, and Tsuyoshi Yamamoto. “Josephson parametric phase-locked oscillator and its application to dispersive readout of superconducting qubits”. *Nature communications* **5** (2014), page 4480.
- [30] Shruti Puri, Christian Kraglund Andersen, Arne L Grimsmo, and Alexandre Blais. “Quantum annealing with all-to-all connected nonlinear oscillators”. *Nature communications* **8** (2017), page 15785.
- [31] Hajime Okamoto, Adrien Gourgout, Chia-Yuan Chang, Koji Onomitsu, Imran Mahboob, Edward Yi Chang, and Hiroshi Yamaguchi. “Coherent phonon manipulation in coupled mechanical resonators”. *Nature Physics* **9** (2013), pages 480–484.
- [32] Thomas Faust, Johannes Rieger, Maximilian J Seitner, Jörg Peter Kotthaus, and Eva Maria Weig. “Coherent control of a classical nanomechanical two-level system”. *Nature Physics* **9** (2013), pages 485–488.
- [33] Joel Moser, Alexander Eichler, Johannes Güttinger, Mark I Dykman, and Adrian Bachtold. “Nanotube mechanical resonators with quality factors of up to 5 million”. *Nature nanotechnology* **9** (2014), pages 1007–1011.
- [34] Adrià Labay-Mora, Roberta Zambrini, and Gian Luca Giorgi. “Quantum Associative Memory with a Single Driven-Dissipative Nonlinear Oscillator”. *Phys. Rev. Lett.* **130** (19 2023), page 190602. DOI: [10.1103/PhysRevLett.130.190602](https://doi.org/10.1103/PhysRevLett.130.190602).
- [35] Heinz-Peter Breuer and Francesco Petruccione. *The theory of open quantum systems*. OUP Oxford, 2002.
- [36] Kazuyuki Fujii. *Quantum Damped Harmonic Oscillator*. 2012.
- [37] Simon Kothe and Peter Kirton. “Liouville-space neural network representation of density matrices”. *Physical Review A* **109** (2024), page 062215.
- [38] David E Evans and Harald Hanche-Olsen. “The generators of positive semigroups”. *Journal of functional analysis* **32** (1979), pages 207–212.
- [39] Marco Cattaneo, Gian Luca Giorgi, Sabrina Maniscalco, and Roberta Zambrini. “Symmetry and block structure of the Liouvillian superoperator in partial secular approximation”. *Phys. Rev. A* **101** (4 2020), page 042108. DOI: [10.1103/PhysRevA.101.042108](https://doi.org/10.1103/PhysRevA.101.042108).
- [40] Victor V. Albert and Liang Jiang. “Symmetries and conserved quantities in Lindblad master equations”. *Phys. Rev. A* **89** (2 2014), page 022118. DOI: [10.1103/PhysRevA.89.022118](https://doi.org/10.1103/PhysRevA.89.022118).
- [41] Fabrizio Minganti, Vincenzo Savona, and Alberto Biella. “Dissipative phase transitions in n -photon driven quantum nonlinear resonators”. *Quantum* **7** (2023), page 1170.
- [42] “Finite-Dimensional Vector Spaces”. In: *Introduction to Mathematical Physics*. John Wiley & Sons, Ltd, 2007. Chapter 2, pages 37–92. DOI: <https://doi.org/10.1002/9783527618859.ch2>.
- [43] C-E Bardyn, M A Baranov, C V Kraus, E Rico, A İmamoğlu, P Zoller, and S Diehl. “Topology by dissipation”. *New Journal of Physics* **15** (2013), page 085001. DOI: [10.1088/1367-2630/15/8/085001](https://doi.org/10.1088/1367-2630/15/8/085001).
- [44] Berislav Buca and Tomaz Prosen. “A note on symmetry reductions of the Lindblad equation: transport in constrained open spin chains”. *New Journal of Physics* **14** (2012), page 073007. DOI: [10.1088/1367-2630/14/7/073007](https://doi.org/10.1088/1367-2630/14/7/073007).
- [45] Bernhard Baumgartner and Heide Narnhofer. “Analysis of quantum semigroups with GKS–Lindblad generators: II. General”. *Journal of Physics A: Mathematical and Theoretical* **41** (2008), page 395303.
- [46] David J. Griffiths and Darrell F. Schroeter. *Introduction to Quantum Mechanics*. 3rd edition. Cambridge University Press, 2018.
- [47] Tameem Albash and Daniel A. Lidar. “Adiabatic quantum computation”. *Rev. Mod. Phys.* **90** (1 2018), page 015002. DOI: [10.1103/RevModPhys.90.015002](https://doi.org/10.1103/RevModPhys.90.015002).
- [48] Edward Farhi, Jeffrey Goldstone, Sam Gutmann, and Michael Sipser. *Quantum Computation by Adiabatic Evolution*. 2000.
- [49] M. H. S. Amin. “Consistency of the Adiabatic Theorem”. *Phys. Rev. Lett.* **102** (22 2009), page 220401. DOI: [10.1103/PhysRevLett.102.220401](https://doi.org/10.1103/PhysRevLett.102.220401).
- [50] Ulf Leonhardt. *Measuring the quantum state of light*. Volume 22. Cambridge university press, 1997.
- [51] Leonard Mandel and Emil Wolf. *Optical coherence and quantum optics*. Cambridge university press, 1995.
- [52] Rémi Azouit, Alain Sarlette, and Pierre Rouchon. “Well-posedness and convergence of the Lindblad master equation for a quantum harmonic oscillator with multi-photon drive and damping”. *ESAIM: Control, Optimisation and Calculus of Variations* **22** (2016), pages 1353–1369.
- [53] QuTiP: Quantum Toolbox in Python. <https://app.readthedocs.org/projects/qutip/downloads/pdf/qutip-5.1.x/>.
- [54] Pablo Gallardo Calleja. *Code for the simulations*. en. <https://github.com/qwerty-asci/Bifurcation-based-quantum-adiabatic-computation-for-resolution-of-combinatorial-problems>. 2025.

- [55] John J Hopfield. "Neural networks and physical systems with emergent collective computational abilities." *Proceedings of the national academy of sciences* **79** (1982), pages 2554–2558.
- [56] E Hairer, Syvert P Norsett, and Gerhard Wanner. *Solving ordinary differential equations I: Nonstiff problems*. en. 2nd edition. Berlin, Heidelberg: Springer Berlin Heidelberg, 1993. DOI: [10.1007/978-3-540-78862-1](https://doi.org/10.1007/978-3-540-78862-1).
- [57] M. Konyik and A. Vukics. "The Monte Carlo wave-function method: A robust adaptive algorithm and a study in convergence". *Computer Physics Communications* **238** (2019), pages 88–101. DOI: <https://doi.org/10.1016/j.cpc.2018.12.015>.
- [58] Juan P. Garrahan. "Aspects of non-equilibrium in classical and quantum systems: Slow relaxation and glasses, dynamical large deviations, quantum non-ergodicity, and open quantum dynamics". *Physica A: Statistical Mechanics and its Applications* **504** (2018). Lecture Notes of the 14th International Summer School on Fundamental Problems in Statistical Physics, pages 130–154. DOI: <https://doi.org/10.1016/j.physa.2017.12.149>.
- [59] A Yu Kitaev. "Fault-tolerant quantum computation by anyons". *Annals of physics* **303** (2003), pages 2–30.
- [60] Yanfen Luo. "Design and Improvement of Hopfield network for TSP". In: *Proceedings of the 2019 International Conference on Artificial Intelligence and Computer Science*. 2019, pages 79–83.
- [61] E Mérida-Casermeiro, G Galán-Marín, and Jose Munoz-Perez. "An efficient multivalued Hopfield network for the traveling salesman problem". *Neural Processing Letters* **14** (2001), pages 203–216.
- [62] Kuo-Sheng Cheng, Jzau-Sheng Lin, and Chi-Wu Mao. "The application of competitive Hopfield neural network to medical image segmentation". *IEEE transactions on medical imaging* **15** (1996), pages 560–567.
- [63] G Galán-Marín, E Mérida-Casermeiro, and José Muñoz-Pérez. "Modelling competitive Hopfield networks for the maximum clique problem". *Computers & Operations Research* **30** (2003), pages 603–624.
- [64] Prakash Chittora, Alka Singh, and Madhusudan Singh. "Application of Hopfield Neural Network for Harmonic Current Estimation and Shunt Compensation". *Electric Power Components and Systems* **46** (2018), pages 290–301. DOI: [10.1080/15325008.2018.1445794](https://doi.org/10.1080/15325008.2018.1445794).
- [65] Hubert Ramsauer, Bernhard Schäfl, Johannes Lehner, Philipp Seidl, Michael Widrich, Thomas Adler, Lukas Gruber, Markus Holzleitner, Milena Pavlović, Geir Kjetil Sandve, et al. "Hopfield networks is all you need". *arXiv preprint arXiv:2008.02217* (2020).
- [66] Aram W Harrow, Avinatan Hassidim, and Seth Lloyd. "Quantum algorithm for linear systems of equations". *Physical review letters* **103** (2009), page 150502.
- [67] János A Bergou and Mark Hillery. *Introduction to the theory of quantum information processing*. Springer Science & Business Media, 2013.
- [68] G. J. O. Jameson. "The incomplete gamma functions". *The Mathematical Gazette* **100** (2016), 298–306. DOI: [10.1017/mag.2016.67](https://doi.org/10.1017/mag.2016.67).
- [69] Daniel Duverney. "Polylogarithm Function". In: *An Introduction to Hypergeometric Functions*. Cham: Springer International Publishing, 2024, pages 239–279. DOI: [10.1007/978-3-031-65144-1_8](https://doi.org/10.1007/978-3-031-65144-1_8).
- [70] DC Wood. "The computation of polylogarithms. University of Kent computing laboratory". *Tech. Rep.* (1992).
- [71] Daniel B. Grünberg. *On asymptotics, Stirling numbers, Gamma function and polylogs*. 2006.
- [72] Izrail Solomonovich Gradshteyn and Iosif Moiseevich Ryzhik. *Table of integrals, series, and products*. Academic press, 2014.
- [73] Alexander Dunn and Nicolas Robles. "Polynomial partition asymptotics". *Journal of Mathematical Analysis and Applications* **459** (2018), pages 359–384. DOI: <https://doi.org/10.1016/j.jmaa.2017.10.051>.
- [74] Dan Romik. "Stirling's Approximation for n!: the Ultimate Short Proof?" *Am. Math. Mon.* **107** (2000), pages 556–557.
- [75] Catherine C McGeoch. *Adiabatic quantum computation and quantum annealing: Theory and practice*. Springer Nature, 2022.
- [76] Steffen Börm and Christian Mehl. *Numerical methods for eigenvalue problems*. Walter de Gruyter, 2012.
- [77] RF Bishop and A Vourdas. "Displaced and squeezed parity operator: Its role in classical mappings of quantum theories". *Physical Review A* **50** (1994), page 4488.
- [78] William B Case. "Wigner functions and Weyl transforms for pedestrians". en. *Am. J. Phys.* **76** (2008), pages 937–946.
- [79] Dragica Vasileska and Stephen M Goodnick, editors. *Nano-electronic devices: Semiclassical and quantum transport modeling*. en. New York, NY: Springer New York, 2011.
- [80] Jan Mostowski and Joanna Pietraszewicz. "Wigner function for harmonic oscillator and the classical limit". *arXiv preprint arXiv:2104.06638* (2021).
- [81] Leslie E Ballentine. *Quantum mechanics: a modern development*. World Scientific Publishing Company, 2014.
- [82] Gal Shavit, Baruch Horovitz, and Moshe Goldstein. "Bridging between laboratory and rotating-frame master equations for open quantum systems". *Physical Review B* **100** (2019), page 195436.